

HIGH SPEED SPINDLE HEAT SOURCES,
THERMAL ANALYSIS AND BEARING PROTECTION

By

WEIGUO ZHANG

A DISSERTATION PRESENTED TO THE GRADUATE SCHOOL
OF THE UNIVERSITY OF FLORIDA IN PARTIAL FULFILLMENT
OF THE REQUIREMENTS FOR THE DEGREE OF
DOCTOR OF PHILOSOPHY

UNIVERSITY OF FLORIDA

1993

ACKNOWLEDGEMENTS

The author wishes to express his sincere appreciation to Dr. Jiri Tlustý, chairman of the supervisory committee, for his guidance and assistance in this study and in the preparation of this dissertation. Genuine thanks are extended to Dr. Scott Smith, member of the supervisory committee, for his help and advice.

The author also wishes to acknowledge the help and assistance from C. Bales, W. Chau, C. Chen, Y. Chen, W. Cobb, D. Smith, and W. Winfough, members of the Machine Tool Research Center (MTRC); Dr. Thomas Delio and John Frost, engineers at Manufacture Laboratories, Inc.; and Dr. Carlos Zamudio and Chris Vierck, former members of MTRC.

Special thanks and appreciation are extended to his wife, Aiyu Li, for her constant support, encouragement, and understanding throughout the length of his program.

TABLE OF CONTENTS

	<u>Page</u>
ACKNOWLEDGEMENTS	ii
LIST OF TABLES	v
LIST OF FIGURES	vi
ABSTRACT	viii
 CHAPTERS	
1 INTRODUCTION	1
Scope of the Problem	1
Historical Review and Contemporary Studies	4
Tasks and Methodology of this Study	9
2 SPINDLE MODELING	14
Spindle Structure	14
High Speed Bearing Load	17
Bearing Heat Generation	19
Internal Motor Heat generation	28
Heat Transfer	31
Other Considerations	34
3 FINITE ELEMENT ANALYSIS (FEA)	37
Finite Element Analysis of Heat Transfer Problems	37
Generation and Solution of Spindle FE Thermal Model	42
Calculation of a Spindle with Bearing Heat Sources	45
Calculation of a Spindle with Bearing and Internal Motor Heat Sources	55
4 SPINDLE TEMPERATURE FIELD MEASUREMENT	63
Thermoelectricity and Thermal Radiation	63
Measurement of a Spindle with Bearing Heat Sources	66
Measurement of a Spindle with Bearing and Internal Motor Heat Sources	71
Comparison with FE Result and Discussion	75

5	HIGH SPEED SPINDLE DESIGN WITH THERMAL CONSIDERATION	80
	Spindle Static and Dynamic Properties	80
	Effect of Forced Cooling on Spindle Temperature	81
	Effect of Spindle Heat Source and Bearing Axial Load	86
	Spindle Bearing Catastrophic Failure Temperature	88
6	SPINDLE BEARING THERMAL PREDICTION MODEL AND BEARING CONDITION DIAGNOSIS	94
	Bearing Defect Frequencies and Detection	94
	Using Thermal Model for Bearing Monitoring	96
	Bearing Monitoring through Measuring Acoustic Emission and Signal Demodulation	102
7	CONCLUSION AND FURTHER WORK	109
	Conclusions	109
	Areas of Further Research	111
	APPENDIX A BEARING CALCULATION PROGRAM	113
	APPENDIX B MOTOR LOSS MEASUREMENT	120
	REFERENCES	124
	BIOGRAPHIC SKETCH	128

LIST OF TABLES

Table	<u>Page</u>
2.1 Coefficient f_v for Angular Contact Ball Bearing	25
2.2 Inductive Power Loss Distribution	29
2.3 Motor Drive DC Power Measurement @ Idling	30
2.4 Surface Characteristic Length for Free Convection	34
3.1 Spindle Surface Classification	47
3.2 Spindle A Simulation Conditions	48
3.3 Spindle A Heat Generation Rate	48
3.4 Spindle A Surface Convection Coefficients	48
3.5 Spindle A Temperature From Simulations	49
3.6 Spindle A Time Constants From Simulations	54
3.7 Spindle Bearing and Motor Heat Generation Rates	57
3.8 Spindle B Convective Coefficients	61
4.1 Spindle A Measured Time Constants	68
4.2 Spindle A Measured Temperature	71
5.1 Bearing Heat Dissipation at Seizure	91
6.1 Curve Fitting Results of Bearing Failure Cases	101
6.2 Curve Fitting of Normal Cases	101
B.1 Motor Loss from DC Power Measurement	122
B.2 Motor Loss from Motor Current and Voltage Measurement	123

LIST OF FIGURES

Figure	<u>Page</u>
1.1 Bearing Thermal Condition Diagram	3
2.1 High Speed Spindle	14
2.2 Angular Contact Ball Bearing	18
2.3 Bearing Ball Gyroscopic Moment	19
2.4 Differential Slipping	22
2.5 Heat Generation: Measurement and Calculation, Bearing 2MMV99120	27
2.6 Heat Generation: Measurement and Calculation, Bearing 2MM9117	27
2.7 Bearing Heat Generation Calculation and Result from Temperature Measurements	28
3.1 Structure of Spindle A	45
3.2 Simplified Structure of Spindle A	45
3.3 Meshes of Thermal Model of Spindle A	45
3.4 Temperature Field and Time Response at I1: a. Case 1, b. Case 2, c. Case 5, d. Case 6	51
3.5 Different Convection Situations	53
3.6 Simplified Spindle B Structure	55
3.7 Meshes of Spindle B	55
3.8 Spindle B Temperature Profiles	58
3.9 Spindle B Temperatures	59

4.1 Infrared Sensor Assembly and Arrangement	67
4.2 Sensor Arrangement for Temperature Measurement	68
4.3 Temperature Measurement for Case 1, Case 2, Case 3, Case 4: a. Case 1, b. Case 2, c. Case 5, d. Case 6	69
4.4 Sensor Arrangement for Temperature Measurement of Spindle B	73
4.5 Measured Temperature Field at 15,000 rpm and 25,000 rpm a. 15,000 rpm, b. 25,000 rpm	73
4.6 Measured vs. Calculated Temperature for Spindle B	74
4.7 Transient Temperature Response, 8000 rpm	75
5.1 Temperature Fields (for Bearings with Water Cooling) at 15,000, 25,000, 35,000 and 45,000 rpm	83
5.2 Temperature in Bearing Races	84
5.3 Temperatures in Bearing Outer Rings	85
5.4 Temperatures at Spindle Arbor Inner Surface	85
5.5 Measured Temperature with Different Bearing Preloads	87
5.6 Bearing Heat Generation Calculation with Different Axial Load	87
5.7 Measured Bearing Seizure Temperature	88
5.8 Bearing Heat Generation a. Bearing Heat Generation Change at Seizure b. Bearing Heat Generation vs. Speed without Seizure	89
5.9 Increase of Bearing Axial Load at Seizure	91
5.10 Bearing Temperature Change at Contact	92
5.11 Bearing Temperature Change of Ring and Ball	92
6.1 Spectrum of Bearing Vibration Signal @ 10,000 rpm	96

6.2 Measured Temperature (Normal & Failure Cases)	100
6.3 Curve Fitting Results for Cases in Figure 6.2	100
6.4 AE Signal and Signal Processing	
a. Pattern of AE Signal of Bearing	
b. AE Signal after Rectification	
c. Rectified AE signal after Low Pass Filter	
d. AE Signal Processing Diagram	105
6.5 Measured Bearing Vibration Signal @ 15,000 rpm	106
6.6 Demodulated Bearing Vibration Signal in Figure 6.5	106
A.1 Program Flowchart	113
A.2 Ball Contact Geometry and Deflection under Load	114
A.3 Deflection of Race-curvature Centers and Ball Center	116
A.4 Ball Force, Moment and Motion Vectors	117

Abstract of Dissertation Presented to the Graduate School
of the University of Florida in Partial Fulfillment of the
Requirements for the Degree of Doctor of Philosophy

**HIGH SPEED SPINDLE HEAT SOURCES,
THERMAL ANALYSIS AND BEARING PROTECTION**

By

Weiguo Zhang

May, 1993

Chairman: Jiri Tlustý

Major Department: Mechanical Engineering

The thermal modeling of high speed spindles and the analysis of their temperature fields, thermal characteristics, and bearing defect signals are presented. The results provide an understanding of the thermal situation of high speed spindles and introduce practical methods for assisting in the analysis and design of high speed spindles.

In this study a thermal modeling technique based on the finite element method was developed for the high speed spindles. The bearing loads, the bearing heat generation properties, the spindle structure meshing, the spindle thermal conduction and convection, and the bearing defect characteristics were investigated. An improved heat generation model of high speed angular contact ball bearings was formulated. Two high speed spindles were modeled and analyzed for illustration and verification. The models were verified against measured temperatures and good

agreement between the computational and experimental results was found. An infrared temperature measurement technique was developed for the temperature measurement inside the cavities of the rotating components. Additionally, the effect of spindle speed, bearing preload, water cooling of the spindle bearings, oil-air lubrication oil drop rate, and air supply pressure were investigated. Model evaluation based on the measurement of a real bearing seizure yielded bearing catastrophic failure load and temperature and showed the large value of the transient thermal load.

Bearing defect monitoring through measuring bearing vibration spectrum, bearing temperature variation and acoustic emission was also investigated in this work. An acoustic emission signal demodulation method was implemented. The measurement of bearing vibration signal shows that this method is effective for bearing monitoring under condition of strong background noise.

CHAPTER 1 INTRODUCTION

Scope of the Problem

High speed, high power and high accuracy spindles are important in the efficient use of machinery and labor resources and in the making of high quality parts. The design of these spindles is a difficult task in the machine tool industry. Such spindles have desirable characteristics, such as high power and high stability, but they also have some limitations. One of these limitations is that when bearings undergo very high dynamic load, they generate a large amount of heat and then are subject to sudden failure due to heavy inertia load and improper lubrication. One of the most important factors affecting high speed spindle performance and bearing life is the spindle thermal condition, which is a combined result of heat generation, heat dissipation, temperature, thermal load and stability.

In this study the spindle thermal condition and related factors were investigated. Also included are analyses of the spindle structure and material properties, the heat source properties, and finite element thermal modeling and analysis. This study provides an understanding of high speed spindle thermal situations and will be useful for the design and analysis of high speed spindles.

Tlusty et al [1] investigated the stability lobes in milling and demonstrated the effect of cutting speed on stability. Tlusty [2] successfully used the stability lobes in

high speed milling. The application greatly improved milling productivity and quality. Currently, the research conducted in the Machine Tool Research Center at the University of Florida and the Manufacturing Laboratories, Inc., has achieved significant increases in metal removal rate (MRR) with a high-speed, high-power spindle. The research revealed that high-speed high-power spindles will play an important role in improving the manufacturing processes.

Since spindles contain heat generation components (for example, bearings and the motor), the thermal condition is a major concern in designing and operating high-speed high-power spindles. Any increases in bearing speed or bearing load are always accompanied by an increase of bearing heat generation. Bearing heat generation affects the spindle thermal situation and bearing lubrication, which again affects bearing heat generation. This process, displayed through the block diagram in Figure 1.1, greatly influences the bearing life and limits spindle speed. Bearing speed and size both restrict maximum bearing speed, and a DN number (where D is the bearing bore diameter in millimeter, and N is the bearing speed in rpm) can best represent these effects. Currently, commercially available high precision bearings with steel balls can be run at speeds up to $DN = 1.5 \times 10^6$, and with ceramic balls $DN = 2.2 \times 10^6$ [3]. It has been understood for some time that the bearing heat generation, heat dissipation and bearing thermal load are important in designing high speed bearing assemblies [4, 5]. Therefore, many measures have been taken to improve the bearing thermal condition. In the design of bearing assemblies, especially with respect to machine tool spindles, many measures to improve the bearing thermal condition were based on experience, but understanding of the

spindle thermal process was limited. For example, it is well-known that the spindle arbor has a high temperature, but the true value and distribution are poorly known. Frequently, in the design, a conservative estimation is made, or experience is followed. The bearing thermal condition and thermal load are not evaluated. The significance of understanding the spindle thermal situation is obvious: knowledge of the temperature field and the thermal expansion allows measures to be taken to limit the temperature and thermal load, and to maintain bearings in a stable working condition.

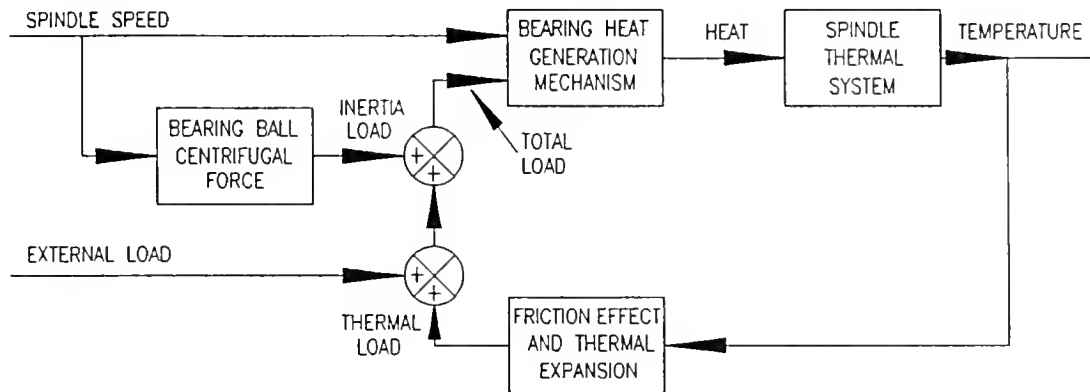


Figure 1.1 Bearing Thermal Condition Diagram

In this study a spindle thermal model was established. The spindle structure treatment, the bearing and motor heat generation, the spindle heat transfer, and the finite element method were used in the modeling process. This model was used to calculate the spindle temperature fields and to predict the temperature at different speeds. Real temperature profile measurements were made and good agreement was reached. This spindle model was then used to estimate the bearing thermal load

from measured spindle temperature field. Spindle bearing temperature and vibration were also investigated.

Historical Review and Contemporary Studies

Jones' Bearing Load Theory

In the 1940s, Jones [6] carried out a load analysis on deep groove and angular contact ball bearings and presented a method, based on bearing geometry, material strength and elasticity theory, to obtain the bearing load distribution. He also proposed the race control theory to describe the ball spinning phenomenon. His later work included the investigation of ball motion and bearing friction[7]. Some of his theory is still used in bearing applications today.

Lundberg-Palmgren's Bearing Life Theory and Palmgren's Work in Bearing Application

Lundberg and Palmgren [8] performed their bearing fatigue life study in the early 1930s. This study related bearing life to bearing load and bearing structure through the famous bearing life formula and through the bearing basic dynamic load rating. This theory, called Lundberg-Palmgren's bearing fatigue life theory, is still the major tool in estimating bearing life.

While evaluating bearing friction and temperature, Palmgren [4] analyzed bearing mechanics and pointed out that interfacial slipping friction between the rolling element and raceway was an important part in bearing mechanical friction. However, due to the complicated nature of bearing friction, when he formulated bearing mechanical friction torque, he adopted experimental data instead of a theoretical expression. He also formulated the bearing viscous friction torque due

to lubricant shearing. These friction equations made it possible to calculate average bearing temperature (bulk temperature) by balancing the heat generation and convection of the bearing assembly [4]. Because of the complexity of the rolling element bearing friction [8], Palmgren's empirical equations are still popular in estimating bearing friction, particularly at low speed.

Other Bearing Heat Generation Formulae

Astridge and Smith [9] investigated the heat generation of roller bearings and found that the viscous friction is a major source of heat generation and that Palmgren's empirical formulae over-estimated bearing heat generation. Ragulskis [10] systematically analyzed all friction torque components in a general sense. His formulae will be further analyzed later in this work.

Tallian's Generalized Bearing Life Theory

When Tallian analyzed the endurance data from a large group of bearings of different types and load conditions, lubrication, maintenance and application, he confirmed that Weibull distribution fit the test data in the most used cumulative failure probability region (failure probability from 0.1 to 0.6) [11], and presented a more general rolling contact fatigue life theory [12]. He systematized the effects of material properties, lubrication, surface roughness, load properties and other operating conditions and presented life correction factors [13, 14]. Since tests should be carried out on all types of bearings to obtain the values of those correction factors, this method has rarely been seriously applied in bearing applications.

Harris's Work on Bearing Load and Application

After Jones and Palmgren, Harris [15] further summarized and developed Jones' theory. He systemized the calculation of the bearing load, ball motion, load

distribution and high speed bearing load distribution, bearing deflection, fatigue life and friction. He used a node system method to calculate the temperatures of the bearing and bearing assembly. He also investigated the gross sliding motion, i.e., skidding between the balls and inner raceway, and developed a method to predict the skidding [15, 16], which is important in high speed bearing operation.

Dowson and Hamrock's Contribution to Bearing Lubrication Theory

For many years before 1950, the lubrication of rolling element bearings was analyzed through hydrodynamics, i.e., the bearing was considered to be lubricated by the oil film generated by the movement and the pressure of the lubricant. Accordingly, at high load, low speed, and low conformity, the hydrodynamic pressure was not high enough to maintain the film, and surface contact would occur. However, the study of hydrodynamic lubrication could not explain many of the rolling contact lubrication phenomena. In 1949 the initial elastohydrodynamic lubrication (EHL) concept was introduced by Grubin, and it was rapidly developed in the 1950s and 1960s by many researchers, particularly Dowson and Higginson [17]. A complete analysis on EHL of point contact was not made until 1976, when Hamrock and Dowson [18] presented their calculation method, results and formulae for central thickness and minimum thickness of EHL film. Since then, much research has been conducted using this theory in the friction and failure analysis of the rolling element bearings and other point contact mechanisms.

Other Studies on Bearings and High Speed Spindles

In 1979, Gupta [19] presented a rolling element bearing dynamic model giving a transient view of the bearing ball and cage motion, bearing friction and temperature. His calculation of friction and temperature was based on empirical

torque and bearing bulk temperature. The study conducted by Zaretsky et al. [20], posted some practical limitations on high speed jet-lubricated ball bearings and compared the jet-lubrication and the oil-mist lubrication. This work provided a good reference for the practical use of high speed bearings and lubrication.

Based on Lundberg-Palmgren's bearing fatigue life theory, Ioannides and Harris [21] proposed an improved bearing life model. It introduced a "fatigue limit stress" concept to describe the initiation of a fatigue crack and used the integration of the computed life of element stress volumes for the life prediction. Their application showed improvement in the life prediction of high speed bearings[22].

At high speeds, the bearing outer race will undergo a very high ball centrifugal force. There was an attempt to reduce this load by changing the single outer-race-ball contact into two contacts through the use of an arched outer race (the outer race arc consists of two pieces of curves such that the balls will have two contacts with each raceway). Coe and Hamrock [23] conducted tests on this type of bearing and no improvement of performance was concluded.

Boness [24] developed an empirical equation that determined the minimum thrust load to prevent the skidding and to improve ball bearing's high speed performance and life. Kingsbury [25] presented an experimental method of measuring the ball-race slip which was important in evaluating the bearing lubrication and friction. Jedrzejewski [26] studied a way to reduce the bearing temperature and power loss by inserting a layer of insulating material between the bearing inner ring and spindle journal, and showed some very good results on a test spindle. Carmichael and Davies [27] investigated the effect of speed, oil type and flow

rate, and housing thermal conditions, on preloaded ball bearing transient and steady state behavior. Their study was done on conventional spindles. Tlustý et al. [28] studied dynamic and thermal properties of high speed spindles with roller bearings, and concluded that the use of roller bearings at $DN = 1 \times 10^6$ and over was possible. Shin [29] investigated high speed spindle bearing stability and predicted that, at a high speed, bearings will present different dynamic characteristics, and stability lobes will be seriously affected. Stein and Tu [30] analyzed a similar spindle and obtained a model which predicted high speed bearing thermal load from temperature, speed, external load, and material properties, which could be used to prevent the bearings from being thermally overloaded. However, the above analyses on high speed bearings and spindles have concentrated on those bearing assemblies where the bearing axial load could not be constantly maintained. Most industrial high speed spindles have been designed so that their bearing loads have been pre-set at some certain high speed range which will yield good bearing performance. In contrast, a spring-preloaded constant axial bearing load mechanism has been successfully used in the research under Tlustý at the University of Florida and Manufacturing Laboratories, Inc., [31]. It was used in a spindle with a speed range of over 0 to 35,000 rpm ($DN = 2.273 \times 10^6$, ceramic ball), and in a modified spindle to increase the speed range from 0 to 6300 rpm ($DN = 6.3 \times 10^5$), to 0 to 12,000 rpm ($DN = 1.2 \times 10^6$, steel ball). It proved that, with good understanding of high speed spindle/bearing thermal behavior, high speeds above $DN = 2.25 \times 10^6$ can be safely achieved. Although there are many general rules in the spindle design temperature estimation such as those mentioned by Harris [5] and Eschmann et al. [32] for the design of high speed spindles, an accurate temperature calculation method is still needed.

Bearing Condition Monitoring and Prediction

Since the 1970s, frequency analysis techniques have been used to diagnose bearing condition in machinery. Many methods have been developed for the monitoring and diagnosing of rolling element bearings. Some examples are the fiber optic bearing monitors for displacement vibration analysis, introduced by Philips [33], the proximity monitors mentioned by Sandy [34], and the velocity transducers suggested by Berry [35]. These techniques use the noise signal produced when the defected component passes the contact as an indication of bearing defect. They are usually effective in measuring the current physical condition of the bearing without strong background noise. Using these techniques one can possibly show how long one damaged bearing can last, but one cannot identify the bearing lubrication condition and load condition. In high speed bearing applications, however, the lubricant starvation and seizure are among the major causes of bearing failure.

Tasks and Methodology of this Study

Heat Source Modeling

The equations of bearing heat generation developed by Palmgren are popular in application. However, since these equations were based on data gathered from bearings running in lower speed ranges, and with the bearing quality and lubrication methods of almost 40 years ago, the accuracy of these equations for high speed bearings has not been studied. Harris [5] presented a method that included the ball spinning torque in the mechanical friction torque equation in order to take some high speed effects into consideration. However, the ball spinning torque is a result from theoretical analysis. It is not logically correct to include this theoretical calculation

into Palmgren's empirical formula of mechanical friction torque. For this study, the bearing heat generation was based on Ragulskis' general equation with special modifications for high speed angular contact ball bearing. Friction estimation was verified against measured spindle power loss data and finite element analysis results.

Estimation of the internal motor heat generation could have been made through measurement or calculation. Based on inductance motor loss analysis [36], the motor heat generation was mainly from power loss, I^2R , and magnetic loss, which account for more than 75% of the total loss. Bearing friction loss was only a small percentage of the total loss. If the resistances of the stator winding and of the rotor conductors could be obtained, a good estimate of the motor heat generation could be calculated. The power loss measurements of the available motor were used in the spindle modeling of this study.

Spindle and Bearing Models

In this analysis, bearings were considered as part of the spindle, and the moving heat generation points were considered as a fixed heat generation circle. The balls were simplified as a fixed ring that connected the outer ring and inner ring of the bearing.

The bearings, internal motor, and arbor structure were symmetrical components, and all the heat generating sources were symmetrically distributed to the spindle center line. The thermal field was also essentially symmetrical. The spindle housing was usually a rectangular or cylindrical block with a flat mounting surface. As a whole, its structure and boundary conditions (BCs) are close to symmetrical to the spindle center line. For the entire spindle, a thermal model of

a 2-D structure was developed instead of a 3-D model in order to eliminate the complexity of modeling and computation without a great loss of accuracy.

Heat Transfer and Calculation

Heat conduction was taken as conduction in homogeneous materials. The interface (joints of the contacting parts) thermal resistances were not considered separately from the material properties. Since many spindle structures are similar, the interface locations and sizes are comparable to the spindle size. This simplification did not limit the model generality. However, because the materials were not consistent, the actual thermal conductivity was not taken from a material property table, but rather was modeled to match the measured temperature.

Another important factor was that air inside the spindle had a much higher ability to convey heat from higher temperature surfaces to lower ones. This was also considered in the model. Heat convection depends on the convective coefficients, surface area and free stream temperature. Here, the coefficients were calculated based on the heat transfer theory, and the free stream temperature was considered as the surrounding temperature. Since the spindle speed affected the convective coefficients, the coefficients actually used were corrected for spindle speed.

The calculation of both steady state and transient thermal responses were made using the Finite Element Analysis (FEA) technique. A PC-based FEM software (*COSMOS/M*) was used to realize the model meshing and to conduct all the calculations. *COSMOS/M* can be used to build the model mesh, attach boundary conditions, compute the temperatures, the temperature gradients, and the heat flux field.

Temperature Field Measurement

The temperature measurement was made on both nonrotating components and rotating components. The measurement of the nonrotating components was done by using thermocouples. The measurement of the temperatures of the rotating components could not be made by contacting methods since, in rotation, any sliding contact would produce significant heat and greatly distort the measurement. Rather, a noncontact temperature measurement was preferred. Since infrared temperature probes can measure temperatures over a wide range accurately without contact, and, since they can be made very small, the rotation component temperature measurement was made by using an infrared technique.

Modeling and Verification

The thermal model was built based on measurements of several different spindles. First, the model was built from the spindle structure and the calculated heat generation rates and convection coefficients. The convective coefficients and some material properties were varied to make the calculated temperature field match the measured result. From the result of the modeling and measurement of several spindles, the model parameters could be accurately determined and temperature field prediction become possible.

Thermal Prediction Model

The purpose of thermal prediction is to use the thermal signal to forecast the bearing working condition and issue the necessary warning to protect the bearing. The thermal prediction is based on the fact that the temperature of any part of a spindle is dependent on the heat source, which, in turn, is dependent on the bearing

performance, load and speed, and, perhaps, the motor load. In the prediction, the measured temperature signal could be compared with the temperature generated by the spindle thermal model so that any difference would suggest a change of the spindle thermal condition. Through the model simulation, the bearing heat generation, and the bearing load, could be estimated. It also could use certain criteria to check the measured temperature which would determine the bearing situation without model simulation. In this study, the proposed criterion was the first derivative of the bearing temperature signal, which was proportional to the change of the bearing heat generation rate. For example, if the bearing temperature slowly rose over a long period of time, this usually meant that the bearing lubrication was deteriorating or the bearing was gradually failing. However, if there was a significant increase of the bearing temperature in a short period of time, then the bearing was possibly under too heavy a thermal load. Another use of the model was to match the measured temperature with the thermal model simulation result, and then one could estimate the bearing load corresponding to the temperature.

Bearing Diagnosis

Spindle vibration signal and acoustic emission (AE) signal can serve as indicators of the bearing health and operation condition, in addition to temperature. Several widely used defect frequency formulae can be used to locate defects of the bearings in signal power spectrum and intensity. The intensity of these signals will show the bearing condition. Since there are strong background noises in a high speed spindle operation, the signal spectrum may not show the bearing condition with confidence. The AE signal and signal demodulation were used here in order to make the diagnosis reliable.

CHAPTER 2 SPINDLE MODELING

Spindle Structure

Spindle Housing and Shaft

Two spindles were investigated in this study (Spindle A and B). Illustrated in Figure 2.1 is Spindle B, which has four bearings and an internal motor. Spindle A has two larger bearings than Spindle B and does not have the internal motor. Spindles are 3-D objects consisting of many parts of different shapes and dimensions, and made of different materials; the detailed structures are very

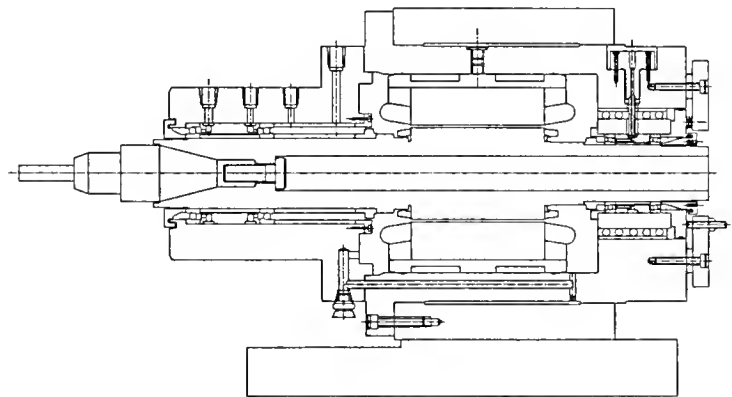


Figure 2.1 High Speed Spindle

complicated. For the purpose of modeling, the detailed structure can be greatly simplified. This process can reduce the number of the model elements and still produce acceptable accuracy. Otherwise, a large number of elements will build a cumbersome model with complicated boundary condition sets. Additionally, any benefits associate with using a large number of elements could easily be

overshadowed by the inaccuracies of the material properties and heat convective coefficients. In this process, the following aspects were considered:

- a. Since most parts in a spindle are cylindrical and symmetrical about the spindle center line, the spindles were considered as a cylindrical object and therefore modeled as 2-D structures. In each case the outer diameter of the cylinder was calculated so as to make the ratio of the housing perimeter to sectional area unchanged. In this way, the time constant is approximately unchanged. The 2-D plane stress, plane strain, body of revolution element, which represents a 3-D solid portion in a cylindrical object covering a center angle of one radian, was selected for the model.
- b. All the adjacent parts (either tight fit or loose fit) were considered as one continuous part. For example, the bearing inner rings were part of the shaft and the bearing outer rings were part of the housing, etc. Subsequently, some special thermal resistances in the interfaces were neglected in the geometry but were compensated for by adjusting the material properties.
- c. Small structures and tiny details were neglected if their dimensions were significantly smaller than the expected element size. Chamfers, tiny holes and small shoulders in the shaft were disregarded. By making the simplification, the object became a 2-D object consisting of several simple parts.

Bearing

Since the bearing rings were taken as a continuous part of the shaft or housing, only bearing balls and cages (ball retainers) were discussed here. Compared with other components, the balls and cages have very small volume (mass) and

surface area, the heat capacity is negligible, and the heat transfer ability, or heat dissipation ability, is limited. Therefore, bearing balls were simplified as a thin ring between outer and inner rings in the 3-D model, and they have a rectangular cross section in the 2-D model. The thickness of the ring was chosen so as to make the volume of the ring close to the volume of the balls.

For example, the front bearing of a spindle has 31 balls, pitch diameter $t = 125$ mm, ball diameter $d_b = 10.3124$ mm, then the total volume of balls is

$$V = 31 * \pi * d_b^3 / 6 = 17800 \text{ mm}^3$$

The total surface area

$$A = 31 * \pi * d_b^2 = 10357 \text{ mm}^2$$

For the ring with a thickness of 2 mm, the total volume is

$$V_r = 2 * \pi * [(t + d_b)^2 - (t - d_b)^2] / 2 = 16198 \text{ mm}^3$$

and the total surface area is

$$A_r = \pi * \{[(t + d_b)^2 - (t - d_b)^2] / 2 + 2 t\} = 8884 \text{ mm}^2$$

After simplification the surface area and volume will be 15% and 10% less than those of the balls respectively. The heat conduction error cannot be easily calculated since the actual contact area is small and load dependent. However, comparing the result of the FEA and that of the measurements, it was found that only a small error had resulted since the ball did little in the total conduction and convection.

In the model the cage was neglected. The error caused by neglecting the cage should be very small. This was because the cage is made of very light material (usually phenolic for high speed) with very low heat capacity and conductivity. Also, the cage has very small contact areas with the balls and rings; therefore, the heat

conduction between the cage and other parts is very small. Consequently, the cage has very small effect in the bearing-spindle thermal condition.

Material Properties

Since there exist "impurities" in the spindle parts, for example, joints, cavities, and different materials, the variance of a material's physical properties is inevitable. The parts in a spindle were classified into three basic groups according to their physical characteristics: (1) solid and uniform materials; (2) porous parts with or without interfaces and of consistent materials; and (3) the same as group 2 of inconsistent materials. For group 1, the material properties were selected directly from a standard material property table with little adjustment. The properties of group 2 were obtained by adjusting the values from the material property table. Measured temperatures were used to check the values. For group 3, material properties were obtained by trial-and-error; for example, the roller-cage of the spindle rear bearing assembly consists of a porous aluminum cage and many small steel rollers, and the rollers have limited contact area with their tracks; therefore, the heat capacity and conductivity of the roller-cage were obtained by adjusting the material property values to match some known results.

High Speed Bearing Load

Ball Motion

Figure 2.2 illustrates the cross section of an angular contact ball bearing. When the bearing inner ring rotates with the spindle shaft, the balls will roll on both inner and outer raceways. The ball's motion consists of an orbital rotation about the spindle axis and a spinning about its own axis. At low speed, bearing contact angles

at inner race and outer race are almost equal, and the ball will have only one possible spinning axis. At high speed, in rotation, the ball mass generates a significant centrifugal force, the outer race contact angle will decrease and the inner race contact angle will increase in order to maintain the equilibrium of the ball. At this moment, the ball will possibly purely roll on either the inner raceway or the outer raceway. In either case, ball-raceway sliding will occur at one contact area.

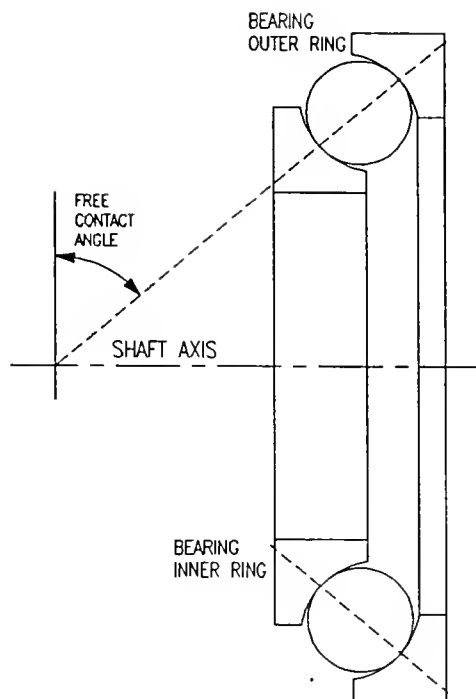


Figure 2.2 Angular Contact Ball Bearing

Since the two rotations of a bearing ball are not parallel to each other, a gyroscopic moment will be produced. This moment intends to give the ball a third rotation-gyroscopic motion (see Figure 2.3). This motion will cause sliding and possibly damage the bearing [4]. To prevent the gyroscopic motion, an angular contact bearing should always be preloaded.

High Speed Bearing Loads

External loads acting on a bearing can be combined as an axial load and a radial load. A ball inside a rotating bearing has several loads, namely, inner race and outer race contact forces, centrifugal force, gyroscopic moment, friction forces against gyroscopic moment, and sliding friction force. These loads can be calculated

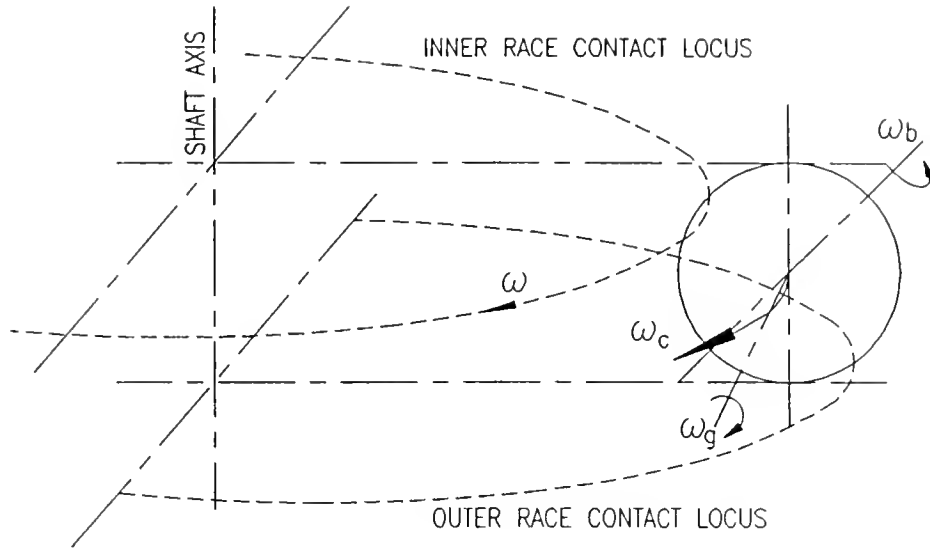


Figure 2.3 Bearing Ball Gyroscopic Moment

through the deflection and load relationship at each ball-race contact and the equilibrium of bearing. Since there are many balls in a bearing and normally every ball has different load, motion and deflection, the solution of loads is a very tedious process. A computer program for the solution of an angular contact ball bearing under general load and rotation condition was developed in this study (Appendix A).

Bearing Heat Generation

General Friction Torque Formula

Ragulskis [10] summarized many researchers' results and stated that the friction torque in bearings consists of the following components:

$$T = (T_{sl} + T_{gyr} + T_{hys} + T_{dev} + T_{ca} + T_{lub} + T_{med} + T_{tem})K \quad (2.1)$$

where

T_{sl} - friction torque from differential slippage of rolling bodies in contact area;

T_{gr} - friction torque arising from gyroscopic spin of rolling bodies;

T_{hys} - friction torque due to losses on elastic hysteresis in the material of bodies in contact;

T_{dev} - friction torque due to deviations of bearing elements from the true geometric shapes and due to micro-asperities on the contact surfaces;

T_{ca} - sliding friction torque along the guiding rims orienting the cage and torque arising from the contact of rolling bodies with the cage cavities;

T_{lub} - friction torque due to shear and shifting of the lubricant;

T_{med} - friction torque due to the working medium of the bearing (gas, air, liquid, vacuum);

T_{tem} - friction torque arising from the change of temperature;

K - correction coefficient taking into account all other unconsidered factors.

Since some factors in the above equation have not been carefully studied yet, some components are insignificant in common spindle bearings, and others are important but not stated, and we could not use this equation directly.

Empirical Formulae

In Palmgren's empirical formulae bearing friction torque T is considered as mainly consisting of two components: the bearing load related friction torque T_l and the lubricant viscous friction torque T_v :

$$T = T_l + T_v \quad (2.2)$$

and according to Palmgren [4] and Harris [5], T_l and T_v can be calculated from

$$T_l = f_l F_s t \quad (2.3)$$

and

$$T_v = f_v 10^{-7} (\nu n)^{2/3} t^3$$

$$\nu n \geq 2000 \quad (2.4)$$

where

T_l - load dependent friction torque, (N-m);

f_l - friction coefficient, which can be obtained from experimental data or the following empirical equation;

$$f_l = z \left(\frac{F_s}{C_s} \right)^y$$

F_s - bearing static equivalent load, (N);

C_s - bearing basic static capacity (static rating), (N);

z, y - bearing structure dependent values;

T_v - viscous friction torque, (N-m);

f_v - coefficient depending on lubricant and lubrication method;

ν - lubricant viscosity in centistoke (mm^2/sec);

n - bearing speed in rpm;

t - bearing pitch diameter, (m).

Because the coefficients of the above formulae are selected from many values by experience, and the natures of some important friction torques (ball sliding, gyroscopic sliding) are not represented by the formulae, these empirical formulae are not accurate. Particularly, for high speed bearing application, since the load related friction torque formula cannot reflect the effects of the preloading mechanism and the centrifugal load which is usually larger than the static load at high speed, they

cannot be simply applied to high speed bearings. The viscous friction torque can well represent the nature of the lubricant shearing friction for a wide speed range.

Improved Formulae

The bearing friction torque formulae used in this study include differential slippage friction torque, the ball sliding friction torque due to uneven contact angles (gross sliding), the ball gyroscopic spin friction torque, the lubricant shearing friction torque and the friction torque arising from ball-cage contact and cage-ring contact.

$$T = T_r + T_s + T_v + T_g + T_c \quad (2.5)$$

Each of the friction torque terms are discussed below.

Differential sliding friction torque T_r

When the ball rolls over the bearing raceway surface, the contact area is an ellipse. Since the ball and the raceway have different curvature radii and the elastic deformations of the ball and the raceway are different, pure rolling will occur only along two lines (Figure 2.4) and small local displacement will occur anywhere else.

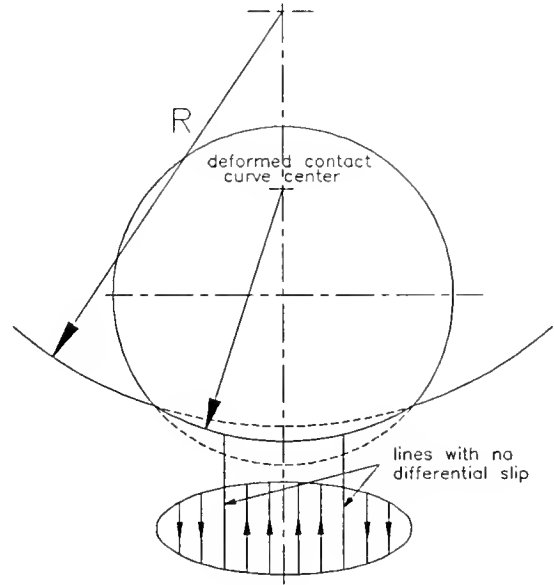


Figure 2.4 Differential Slipping

The work done for one ball by this slippage can be expressed by

$$W_j = F_{ij}l_{ij} + F_{oj}l_{oj} \quad (2.6)$$

where F is the friction force caused by differential sliding, l is the distance travelled

in a unit of time by the point of contact of the ball with race; subscript j refers to the j th ball, i and o refer to inner race and outer race respectively.

Friction force F can be expressed by the product of normal force and a friction coefficient, and the slipping distance can be expressed by

$$l = \frac{\pi}{2} t (1 - \frac{d_b^2}{t^2} \cos^2 \alpha) n \quad (2.7)$$

and then the friction torque T_r is

$$T_r = \frac{1}{2\pi n} \sum_1^{n_b} W_j \quad (2.8)$$

where α is the contact angle, a different value applies at the inner race and the outer race, d_b is ball diameter, and n_b is the number of balls in the bearing.

Ball gross sliding friction torque T_s

When an angular contact ball bearing starts to rotate, the ball will have different contact angles at the inner race and the outer race. The higher the speed, the larger the difference. Mainly because of the unequal contact angles, the balls in the bearing will slide either on the inner raceway or the outer raceway, or both. In order to distinguish this sliding from differential slipping, it is called gross sliding. If gyroscopic spinning can be prevented, the ball will slide on one race only, and the ball gross sliding friction torque can be estimated through the following equations.

At first, the sliding torque acting on the ball, T_s^b , is

$$T_s^b = \frac{3}{8} f_s F a E_2 \quad (2.9)$$

and then this torque T_s^b can be converted to T_s acting on the bearing

$$T_s = \frac{T_s^b \omega_s}{\omega_c} \quad (2.10)$$

where f_s is coefficient of sliding friction, F is contact load, a is the semi-major axis of contact ellipse, E_2 is the elliptic integral of the second kind, ω_s is the ball spinning speed on one race (2.11), and ω_c is the ball orbital rotation speed (cage speed).

$$\left[\frac{\omega_s}{\omega_{roll}} \right]_o = -(1 + \gamma \cos \alpha_o) \tan(\alpha_o - \beta) + \gamma \sin \alpha_o \quad (2.11a)$$

$$\left[\frac{\omega_s}{\omega_{roll}} \right]_i = (1 - \gamma \cos \alpha_i) \tan(\alpha_i - \beta) + \gamma \sin \alpha_i \quad (2.11b)$$

where ω_{roll} is the ball rolling speed on the race, β is the ball altitude angle, γ is the ratio of the ball diameter and the bearing pitch diameter, and the subscripts o and i refer to spinning on the inner race and the outer race.

Ball gyroscopic spinning friction torque T_g

If the ball gyroscopic moment can overcome the ball-race friction force, the ball will spin, and the friction torque generated on a ball is its gyroscopic moment:

$$T_g^b = I_p \omega_b \omega_c \sin \zeta \quad (2.12)$$

where I_p is the mass moment of inertia of the ball, ω_b is the ball spinning speed, ω_c is the bearing cage rotation speed, and ζ is the angle between vector ω_b and vector ω_c . T_g^b can also be converted to a torque acting on the bearing, T_g , as below:

$$T_g = K_g T_g^b \quad (2.13)$$

This conversion can not be expressed in a direct form since the ball spinning speed under T_g^b can not be obtained. The conversion factor K_g depends on the bearing lubrication and geometry.

Lubricant viscous friction torque T_ν

The lubricant viscous friction torque is computed according to (2.4)

$$T_\nu = \frac{1}{90} f_\nu (\nu n)^{2/3} t^3 \quad (2.14)$$

Here f_ν is a friction coefficient depending on lubrication (from Table 2.1).

Table 2.1 Coefficient f_ν for Angular Contact Ball Bearing[†]

Lubrication Type	Coefficient f_ν
Oil Mist & Air/Oil	1.0
Oil Bath and Grease	2.0
Vertical Mounting Flooded Oil and Oil Jet Lubrication	4.0

[†]: Coefficient values adopted from Harris [5].

Bearing cage-ball and cage-ring friction torque T_c

Cage related friction torque T_c consists of the friction torque between rolling elements and cage, T_{c1} , and the friction torque between cage and bearing ring guiding rim, T_{c2} . From Ragulskis [10],

$$T_{c1} = \frac{t}{4} \left(1 - \frac{d_b^2}{t^2} \cos \alpha \right) \sin \left[\alpha + \tan^{-1} \left(\frac{d_b \sin \alpha}{2R_i} \right) \right] G_c f_c n_b \quad (2.15)$$

$$T_{c2} = k G_c f_c n^2 D_r \epsilon \left(\frac{t - d_b \cos \alpha}{t} \right)^2 \quad (2.16)$$

where R_i is the radius of the race on the inner ring, G_c is the mass of the cage, f_c is the friction coefficient, k is a conversion factor depending on which ring the cage is guided, D_r is the diameter of the cage guiding rim, and ϵ is the eccentricity of the cage with respect to the axis of the bearing.

Comparison of Empirical Formulae and Improved Formulae

Spindle power consumptions were measured on Spindle A and the results are plotted in Figure 2.5 and 2.6 against the calculation results with the empirical formulae and improved formulae. In Figure 2.5 and 2.6, all cases were measured with constant axial load. Case A1S refers to newly installed bearings and short spindle running time. Case A1L refers to the same bearings and long spindle running time. Cases A2S and A2L indicate the same bearing cases A1S and A1L with more than a thirty-hour running time. Also in the figures, "Old Formula" refers to the calculation result from the empirical formulae (2.2 to 2.4) and "New Formula" refers to the improved formulae (2.5 to 2.16). It can be seen that the empirical formulae underestimated the bearing friction torque in the high speed range and the improved formulae better estimated the bearing friction torque.

Another comparison was made on Spindle B by using the calculated bearing heat generations to compare with the values obtained through matching spindle temperature profiles with temperature measurements, as shown in Figure 2.7. The smoother curve was obtained from equations (2.5) to (2.16) and represents the estimation of bearing heat generation. The second curve represents the actual bearing heat generation. On the second curve, the first part between 0 and 25,000 rpm was obtained through finite element calculation to match the measured temperature field, and the part between 30,000 and 50,000 rpm was a curve-fitting extension of the first part. It can be seen that the calculation result was close to the real bearing heat generation. Because there were flaws on the ball-race contact surfaces of the bearing, the actual bearing heat generation is not a smooth curve.

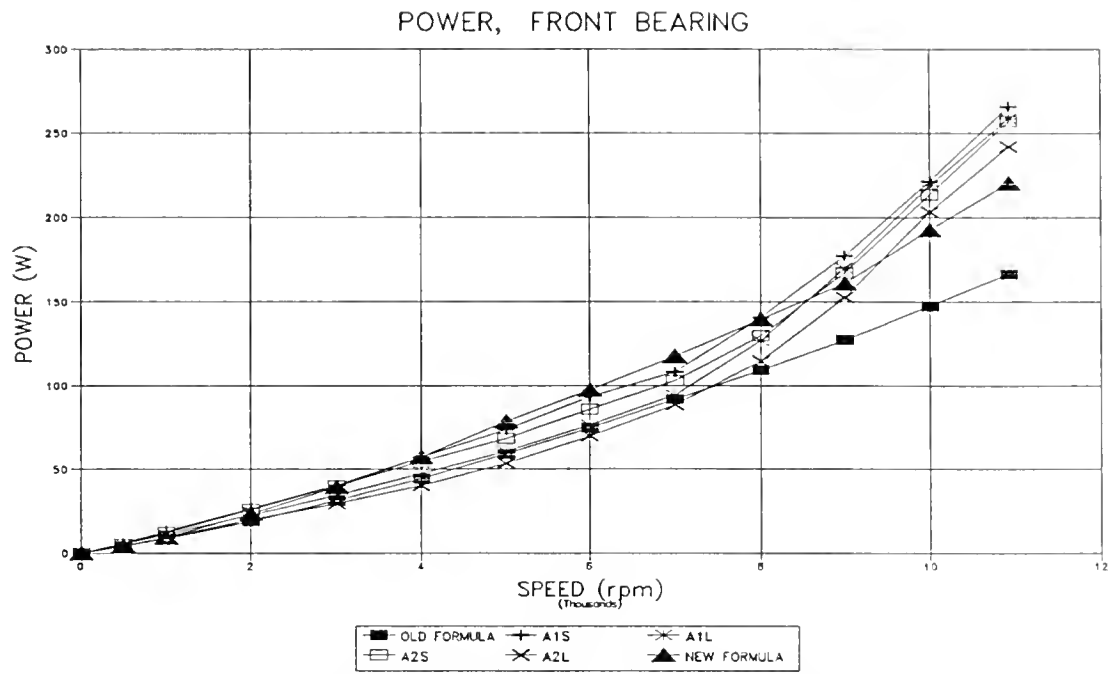


Figure 2.5 Heat Generation: Measurement and Calculation, Bearing 2MMV99120

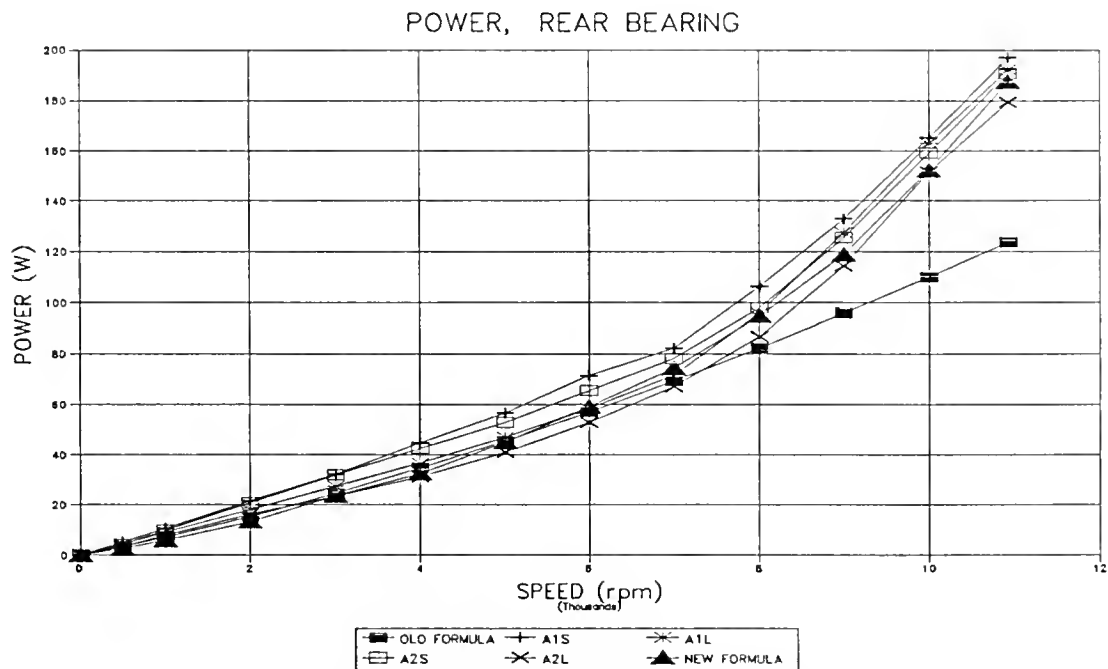


Figure 2.6 Heat Generation: Measurement and Calculation, Bearing 2MM9117

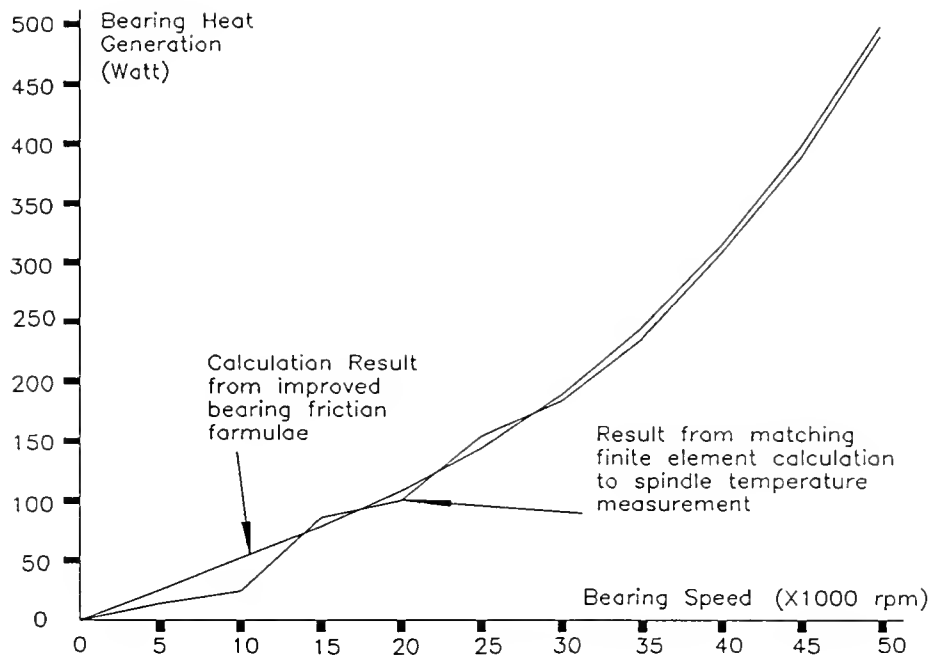


Figure 2.7 Bearing Heat Generation Calculation and Result from Temperature Measurement

Internal Motor Heat Generation

Spindle Internal Motor Structure

In order to reach very high speeds, almost all internal spindle motors on high speed spindles are variable frequency, inductance motors. This type of motor has a stator winding and a silicon steel laminate rotor with aluminum bars (cage) fitted into laminate slots. The stator winding and rotor aluminum conductors generate most of the heat.

Inductive Motor Losses

From the statistics provided by Andreas [36], the standard NEMA (National Electrical Manufacturers Association) Design B inductive motors have an average

loss distribution as shown in Table 2.2. The motor full load efficiency is 89% to 92% for this type of inductive motor with the power between 25 and 100 HP.

Since a spindle will have more and larger bearings than an inductive motor of the same power, there will be greater frictional loss. In this text, "motor loss" or "motor heat generation" does not include loss or heat generation in spindle bearings.

Table 2.2 Inductive Motor Loss Distribution[†]

Motor Component Loss	Percentage of Total Loss (%)
Stator Power Loss I_1^2R	37
Rotor Power Loss I_2^2R	18
Magnetic Core Loss	20
Friction and Windage	9
Stray Load Loss	16

[†]: Data adopted from Andreas [36].

Motor Heat Generation Estimation

If no measurements can be made on the motor and no motor design parameters are known, the motor loss can be roughly estimated through motor power, efficiency and loss distribution.

For a motor without an external load, the motor power can be found by measuring the motor voltage, current and phase angle at different speeds. From this measurement, the total power consumption can be calculated, and this total power minus the calculated bearing friction power will be roughly the motor power loss, and the distribution of the loss can be estimated based on Table 2.2.

Theoretically, when the motor design parameters (winding and rotor conductor resistance, inductance, phase angle) are provided, the motor loss can be calculated. For example, the friction torque can be expressed by $T = K_i i$, where K_i can be estimated by known motor parameters, i can be calculated from the stator winding resistance, inductance and motor speed. The motor loss is the product of the torque and the motor speed. In most situations, however, accurate motor loss data can only be obtained from measurement.

Motor Loss Measurement

The motor loss was measured for the test HS spindle through the accessible circuitry of the frequency inverter (motor drive) of the motor (Appendix B). Two methods were used and the measured results are listed in Table 2.3.

Table 2.3 Motor Drive DC Power Measurement @ Idling

RPM	I_{DC} (A)	V_{DC} (V)	P_{DC} (W)	P_{load} (W)
2500	3.0263	42.857	129.7	103.8, 100.0/119.5
5000	3.1579	85.714	270.7	216.6, 159.4/200.0
7500	3.4211	128.571	439.9	351.9, 227.7/269.7
10,000	3.6842	171.429	631.6	505.3, 321.1/359.2
12,500	4.0789	214.286	874.1	699.3, 438.7/499.0
15,000	4.3684	257.143	1123.3	898.6, 598.9/778.5
17,500	4.7895	300.000	1436.9	1149.5, 839.7/1047.4
20,000	5.0526	342.857	1732.3	1385.8, 1021.4/1276.7
22,500	5.5263	385.714	2131.6	1705.3, 1294.6/1526.5
25,000	5.8421	428.571	2503.8	2003.0, 1517.0/1897.3

Table 2.3 lists the inverter's DC power and the motor load. The DC power is a direct measurement, and the drive switching circuit loss is about 20% of this DC

power. Since there was no external load, the load is the motor loss and bearing friction loss. The values on the left were obtained by subtracting 20% loss of the drive circuit from P_{DC} . The values on the right were calculated from the measured motor "load current" (not DC current, two values here are due to two ways to read this current, see Appendix B).

Heat Transfer

Conduction

Conductive heat transfer mainly occurs inside spindle parts and other non-convection areas, such as enclosed spaces with no opening and no air movement. Outside the spindle, although significant conduction exists, as the heat is conducted between the spindle and machine mounting surface, conductive heat transfer cannot be accurately calculated, since the heat conducted between spindle and machine cannot be calculated. This amount of conductive heat transfer is then compensated through convective heat transfer. Since most spindles have a ratio of mounting area to their total surface area ranging from 0.15 to 0.3, convection is the major mode of the spindle surface heat transfer.

Convective Heat Transfer

There are many formulae for convective heat transfer coefficient calculation, but they always are subject to certain conditions (surface shape, orientation, and fluid situation). Those conditions can hardly match those of the spindle convection surfaces. Therefore in the modeling the coefficient calculation is based on the relation deduced from convection theory regarding the actual conditions (fluid flow speed, characteristic length, film temperature and fluid properties) of different

spindle parts. Consequently, the calculation will be more closely related to the individual surface, and, for each type of surface, a relationship between the flow speed, characteristic length and surface orientation can be established and used for general spindle modeling.

There are two basic types of convective heat transfer: forced and free (or natural) convection. Forced convection was produced by the rotating spindle and can be analyzed by the conductive heat transfer in the thermal boundary layer and the flow of fluid outside this layer. The analysis can be found in many heat transfer textbooks, *e. g.* Holman [37], and only the result is presented here. The resultant averaging convective heat transfer coefficient is

$$\bar{h} = 0.664 R_{el}^{1/2} P_r^{1/3} \frac{k}{L} \quad (2.17)$$

where R_{el} - Reynolds number:

$$R_{el} = \frac{\rho u_{\infty} L}{\mu} \quad (2.18)$$

P_r - Prandtl number:

$$P_r = \frac{\nu}{\alpha} = \frac{c_p \mu}{k} \quad (2.19)$$

k - fluid heat conductivity;

L - surface characteristic length;

If the fluid properties are not constant (as in most cases), they can be calculated at the film temperature T_f

$$T_f = \frac{T_w + T_{\infty}}{2} \quad (2.20)$$

where T_w and T_{∞} are wall temperature and fluid temperature respectively.

Although generally the convective heat transfer of a spindle surface is forced convection, at low spindle speed and with the surrounding air not sufficiently disturbed to produce forced convection, natural convection prevails. It is said that natural convection is of primary importance if

$$\frac{G_r}{R_e^2} \geq 10 \quad (2.21)$$

where

G_r - Grashof number, which may be interpreted physically as a non-dimensional group representing the ratio of the buoyancy forces to the viscous forces in the convection flow system.

$$G_r = \frac{g\beta(T_w - T_\infty)L^3}{\nu^2} \quad (2.22)$$

g - gravity;

β - volume coefficient of expansion of the fluid;

L - surface characteristic length.

If free-convection is dominant, a simple flat-surface formula will be used for the convection coefficient calculation

$$\bar{h}_f = C \left(\frac{\Delta T}{L} \right)^{\frac{1}{4}} \quad (2.23)$$

providing that the fluid flow is laminar and L is properly chosen. Factor C ranges from 1.32 to 1.42, and only when the plate surface is horizontal $C = 0.59$. Characteristic length L can be chosen according to Table 2.4.

Table 2.4 Surface Characteristic Length for Free Convection

Surface	Orientation	L value
Plate Surface	Vertical	Plate vertical dimension
	Horizontal	Plate horizontal dimension
Cylinder Surface	Vertical	Cylinder length
	Horizontal	Cylinder diameter

Convective Conduction

There is a special case in the spindle heat transfer which is the heat transfer via the moving air enclosed in the spindle housing. Since inside the spindle the air is moving very fast and the convection coefficient between surfaces and moving air is very high, heat can be considered to be quickly removed from high temperature surfaces and transferred to low temperature surfaces. This phenomenon is a two stage convection but cannot be easily applied in the FEA model. In this study, the fast moving air was considered as a medium with low heat capacity and high heat conductivity, and its conductivity depends on the spindle speed and the size of spindle. The experimental work of Davis et al. [38] has shown that in this situation better internal heat transfer can be expected.

Other Considerations

Internal Convection

Since the internal cavities of spindles are not totally isolated from the outside, and oil-mist or oil-air lubrication supplies air to the inside of the and causes an air flow, convection heat transfer occurs. In most instances, this stream of air is very

small and since the air has very low heat capacity, this air flow does not contribute much to spindle heat dissipation. In this study, forced convection with small coefficients was used to emulate this phenomenon in the FE analysis, and it was seen from the results that the heat transferred by this internal convection was very limited.

Nonlinear Heat Source

In the bearing seizure cases which occurred in the study, it was observed that bearing heat generation increased with time when spindle speed was constant (Chapter 5). This type of heat generation sources is called nonlinear heat sources. This increasing heat generation occurred since the bearings were fixed in the spindle and the constant axial load mechanism could not relieve the bearing load. Then when the bearings were running, bearing heat generation would cause high temperature on the shaft than on the spindle housing. The difference of the shaft and housing expansions resulted in higher bearing load. Consequently, higher load resulted in more bearing heat generation and more difference in shaft and housing expansions, and this process continued until the bearings were seized. Similarly, for spindles without constant bearing axial load mechanism, different expansions of the shaft and the housing can cause an increase of bearing load and limit maximum spindle speed.

External Heat Sources

A cutting tool under working conditions will generate substantial heat and some of this heat may be conducted into the spindle. In a high speed spindle, especially in high speed milling, in order to eliminate flexibility, tools are mounted as close to the spindle front bearing as possible, then the heat flow path from tool

to spindle will be shorter and more heat will be conducted into the spindle. Generally, this amount of heat is small compared with the heat generated from the bearings and/or motor. The external heat sources were not considered further in this study.

Bearing Condition Monitoring

Conventionally, the bearing thermal condition is monitored by measuring the maximum temperature of the bearing. If the temperature is beyond a preset limit, it is said that the bearing assembly needs to be serviced. This criterion has some problems. It cannot identify bearing condition before the bearing temperature becomes high. If the temperature is due to a failing bearing, the bearing will possibly already be damaged when the temperature reaches its limit, especially in the high speed case. If the temperature limit is set sufficiently low to avoid damaging to the bearing, the bearing capacity will be restricted. There was a bearing seizure in this study, and although the monitored temperature did not reach the limit (80 °C), the bearings were already damaged.

Bearing temperature change is another indicator of bearing health. The bearing failure cases observed in this study all were accompanied with abnormal temperature increase before the failure. It seems that temperature change monitoring may be a good method for bearing catastrophic failure (unstable thermal load, lubrication failure). Bearing vibration (noise) analysis is a method for detecting a bearing with defective components, but there is very strong noise in high speed bearing vibration signal. The use of bearing acoustic emission can eliminate the noise and identify bearing condition.

CHAPTER 3 FINITE ELEMENT ANALYSIS (FEA)

Finite Element Analysis of Heat Transfer Problem

The finite element method consists primarily of replacing a set of differential equations in terms of unknown variables with an equivalent but approximate set of algebraic equations where each of the unknown variables is evaluated at a nodal point. Normally, there are seven steps in the FEA technique:

1. formulate governing equations and boundary conditions;
2. divide the analyzed region into finite elements;
3. select the interpolation functions;
4. determine the element properties;
5. assemble the global equations;
6. solve the global equations; and
7. verify the solution.

Several different approaches may be used in the evaluation of the governing equations. Three of the most popular methods are the direct, the variational, and the residual methods. In the direct method, the unknown variables are expressed as a set of equations for each of the structural members or elements. The equations are converted into element matrices, and those matrices are assembled together to form a large (global) matrix representing the entire structure. Various methods can

be used to solve for the variables. Although it is straight-forward, this method is difficult to apply to two- and three-dimensional problems. The variational method involves a quantity called a functional, and minimizes the value of the functional with respect to each of the nodal values. The solution to the problem is approximated by the finite element function T^* such that $T^* \approx T$, where T and T^* represent temperature of an element and T is the actual value. The approximate solution is defined as the sum of a set of local functions, one for each element:

$$T^* = \sum_{e=1}^e T^{(e)} \quad (3.1)$$

An advantage of the variational method is the easy extension to two- and three-dimensional problems. The disadvantages include the lack of a functional for certain classes of problems and the difficulty of finding them for other problems even when they exist. Therefore, other methods, such as the residual method, are sometimes used. The residual method usually starts with a governing boundary value problem. The differential equation is written so that one side is zero. Then some approximation of the exact solution is employed and substituted into the equation to generate an error r , rather than zero. The error r is then multiplied by a weighting function W , and the product is integrated over the solution region. The result is called the residual R and is set equal to zero. Actually, there is a weighting function W and a residual R for each unknown nodal value, so the result is a global set of algebraic equations.

There are many FEA packages on the market, such as *NASTRAN*, *ANSYS*, *I-DEAS(CAEDS)*, *ALGOR* and *COSMOS/M*. The selection of a FEA software

depends on suitability and cost. In this study, *COSMOS/M* was used. It is capable of performing linear/nonlinear static, linear/nonlinear dynamic, buckling, heat transfer, fluid flow, and electromagnetic steady and transient state analysis on one-, two- and three-dimensional models with full double-precision accuracy, which leads to results comparable with those obtained from major FEA packages on mini-computers and mainframe systems. Although the cost of the software is an important concern, *COSMOS/M* has certain advantages. For example, it can perform transient heat transfer analysis which some other programs (such as *CAEDS*) cannot, and *COSMOS/M* has a comprehensive element library. It can handle 15,000 elements and 15,000 nodes in one model and can be used in a micro-computer.

Heat Transfer Governing Equation and FE Formulation

Heat transfer analysis is a boundary (field) problem and the governing classical equations consist of the equations governing the heat flow equilibrium in the interior and on the surface of the body:

$$\frac{\partial}{\partial x} \left(k_x \frac{\partial \theta}{\partial x} \right) + \frac{\partial}{\partial y} \left(k_y \frac{\partial \theta}{\partial y} \right) + \frac{\partial}{\partial z} \left(k_z \frac{\partial \theta}{\partial z} \right) = -q^B \quad (3.2)$$

$$\theta|_{S_I} = \theta_e \quad (3.3)$$

$$k_n \frac{\partial \theta}{\partial n} |_{S_2} = q^s \quad (3.4)$$

where k_i is the conductivity in i direction, θ is temperature, S is the surface of the object, and q is the heat quantity transferred. There are three basic assumptions for these equations:

1. the body of heat transfer is at rest;
2. heat transfer can be analyzed decoupled from the stress condition and
3. no phase change and latent heat effect.

Our case satisfies these assumptions.

A variety of boundary conditions are encountered in heat transfer analysis:

1. temperature conditions, as expressed by (3.3);
2. heat flow conditions, as expressed in (3.4);
3. convective conditions, which are generalized as (3.4) and expressed by:

$$q^s = h(\theta_e - \theta^s) \quad (3.5)$$

4. radiation boundary conditions with its general form as (3.4):

$$q^s = \kappa(\theta_r - \theta^s) \quad (3.6)$$

$$\kappa = h_r(\theta_r^2 + (\theta^s)^2)(\theta_r + \theta^s) \quad (3.7)$$

where h is convection coefficient, κ is heat quantity transferred through radiation, subscript r and e refers to heat source and element, and superscript s refers to the surrounding. For the development of a finite element solution scheme, either the direct, the variational or the residual formulation can be employed. For a general three-dimensional heat transfer problem often the variational method is used and a variational functional can be expressed as

$$\Pi = \int_v \frac{1}{2} \{ k_x \left(\frac{\partial \theta}{\partial x} \right)^2 + k_y \left(\frac{\partial \theta}{\partial y} \right)^2 + k_z \left(\frac{\partial \theta}{\partial z} \right)^2 \} dv - \int_v \theta q^B dv - \int_{s_2} \theta^s q^s dS - \sum_i \theta^i \theta^s \quad (3.8)$$

By the property of a variational functional

$$\delta \Pi = 0 \quad (3.9)$$

in matrix form

$$\int_V \delta \Theta^T k \Theta dV = \int_V \delta \Theta q^B dV + \int_{S_2} \delta \Theta^S q^S dS + \sum_i \delta \Theta^i Q^S \quad (3.10)$$

where

$$\Theta^T = \left[\frac{\partial \Theta}{\partial x} \quad \frac{\partial \Theta}{\partial y} \quad \frac{\partial \Theta}{\partial z} \right] \quad (3.11)$$

$$k = \begin{bmatrix} k_x & 0 & 0 \\ 0 & k_y & 0 \\ 0 & 0 & k_z \end{bmatrix} \quad (3.12)$$

and "δ" denotes "variation in." This equation expresses the heat flow equilibrium at all times of interest. The step-by-step incremental equations can be developed by a systematic procedure and finally discrete equations will be produced for each different heat transfer case (linear, nonlinear, steady and transient state). All the above-mentioned procedures can be found in many finite element textbooks, such as Bathe [39], and will not be discussed further.

Spindle Heat Transfer Model

A spindle is a multi-component three-dimensional object with a complicated physical profile, load and boundary conditions. There are many inter-component joints which usually have temperature-dependent properties, and the spindle's internal heat generation is also dependent upon its thermal condition and some random variables. Spindle heat transfer has many nonlinear factors. It is impossible to obtain a spindle heat transfer model in a general sense and the model size and cost of analysis will be tremendously large if many of these structural and nonlinear

properties are taken into consideration in the model. In order to overcome the difficulties mentioned above and to get a general spindle thermal model, many generalizations and simplifications were made, such as those mentioned in Chapter 2. Ignoring the existence of physical joints may introduce errors in the temperature profile (there is normally a temperature discontinuity in a joint), and assuming a two-dimensional symmetric model will generate other inaccuracies in the resultant temperature field. However, the joint temperature discontinuity can be compensated for by adjusting material properties, and the 2-D model can represent a 3-D object if the average BCs are used and the boundary dimensions are properly chosen.

Generation and Solution of Spindle FE Thermal Model

Generating Spindle FE Model

After the spindle structure has been modified for modeling purpose, meshes can be generated following the steps below:

- a. Enter coordinates (may use different methods) of important points which represent intersection points in the simplified 2-D structure.
- b. Connect corresponding points to form lines of the spindle profile. For each closed line loop a contour can be defined, and if a contour encloses none or some other contours but is not enclosed by any other contours, this contour and its enclosed contour(s) can form a region. A region is a basic unit for auto-meshing.
- c. Define element groups (type of elements) and material groups (material properties) and decide which will be active while meshing. The meshed

elements will be of the current active element type and have the current active material properties. The selected element type is *PLANE2D* in our study since it supports the axial symmetric property.

d. Meshing. Auto-meshing, manual-meshing are two meshing methods in *COSMOS/M*. Auto-meshing is faster and can be applied to a defined region to generate most of the elements, while elements from auto-meshing of a very irregular region will be distorted and further refining should be used in order to yield evenly shaped elements. The extent of element distortion is measured by the element aspect ratio. Generally, the refining process will consume more time than that spent on auto-meshing if the region is uneven, and will generate more elements. Manual-meshing can be applied to any part in the space. It is a slow process but the element shape from manual meshing can be fully controlled. Since the regions defined from a spindle usually are very uneven and complicated, and the number of elements does not have to be very large, manual meshing may be used for most of the cases. Before meshing, corresponding element group and material group should be activated. In our case, since *COSMOS/M* does not support auto-meshing of axial symmetric 2-D elements, auto-meshing could not be used.

e. Merging nodes which are located too close to each other and elements which are overlapping, and compressing nodes and elements so all the nodes and elements will be numbered in a continuous order. All elements should be connected through nodes. The element shape should be as close to square as possible and, generally, the difference of sides, in term of aspect ratio, should

be less than five times. The connectivity and element shape can be checked automatically by executing the *CHECK* command in *COSMOS/M*.

Applying Load and Boundary Conditions

In *COSMOS/M* the thermal load can include a nodal heat source, node and element heat flux, and an element heat source. Since bearing heat generation is located at the ball-race contact and the contact area is very small, it was considered as a nodal heat source. Internal motor heat is generated from the stator winding and rotor conductors and was represented by element heat sources. In the analysis of an individual component or assembly, heat flux was used to describe heat flow between the contact surfaces of components. Only convective boundary conditions are applied to boundary elements. The values of node heat, element heat and convection coefficients were calculated through the formulae in Chapter 2, and were modified by matching the FEA result to measured temperature fields.

Analysis

Steady state analysis was made after the BCs were added to the model and the maximum number of iterations and convergence tolerance were specified. For the transient state analysis, a time step and a time range were given before starting the analysis. Since many machine tool spindles have similar operation conditions, convective coefficients have a relatively general meaning. The verified coefficients in this model can be applied to corresponding elements of another spindle model if there are no measurements available. Many pilot cases were analyzed in this study and the convective coefficients and material properties were tuned to make the FEA result fit the measured data.

Calculation of a Spindle with Bearing Heat sources

Modeling Spindle A

Figure 3.1 illustrates the original physical structure of Spindle A. After simplifying the complicated details and neglecting the small structures, such as lubrication orifices and screw holes, a 2-D object was developed, as shown in Figure 3.2. Then manual-meshing was used to create nodes and elements. The nominal element size was chosen as 10 mm comparing the overall length 960 mm of the spindle. Figure 3.3 illustrates the final mesh for Spindle A.

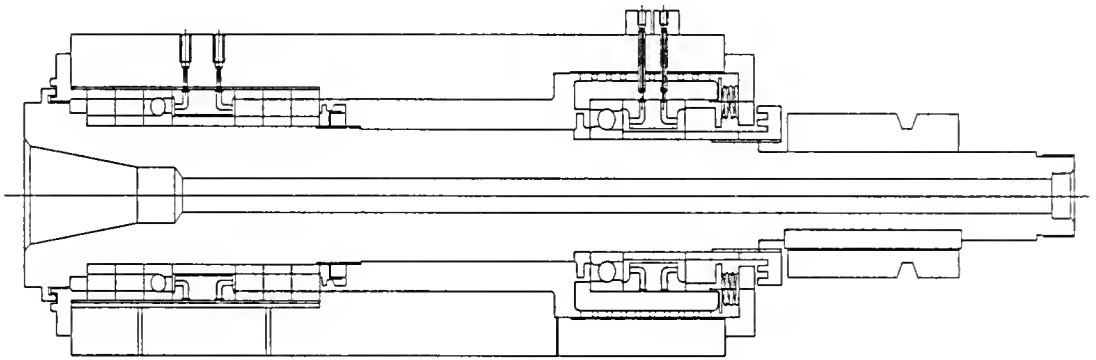


Fig. 3.1 Structure of Spindle A

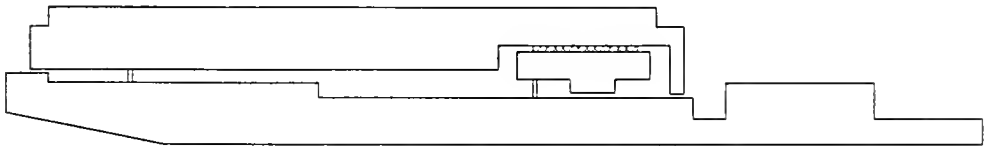


Fig. 3.2 Simplified Structure of Spindle A

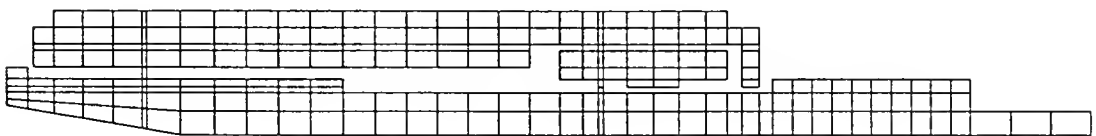


Fig. 3.3 Meshes of Thermal Model of Spindle A

The thermal load condition for Spindle A was frictional heat at bearing contacts. There are two bearings in the spindle, and correspondingly in the 2-D model, there are 4 contact points, or 4 node heat sources. All the surfaces are convection surfaces except the interface surfaces. The meshing is valid for all of the simulation cases (different speed, lubrication). For different cases, the heat generation rate and surface convection coefficients were different and were evaluated accordingly. In order to investigate the convection property of different surfaces, the spindle surfaces were classified into seven categories, as shown in Table 3.1. The classification is based on the surface air flow velocity.

Calculation Cases

Spindle speed, cooling and lubrication, were considered to be the most important factors in spindle model for designated spindle structure and bearings. Hence, spindle thermal analyses were conducted under the conditions as listed in Table 3.2. The speeds were 4000 and 8000 rpm, air-oil producer inlet pressures were 35 and 75 psi, and two cooling conditions were the shaft center hole with both ends open and with only one end open.

In Table 3.3, bearing heat generation rates are listed for the different cases. These values were obtained from the improved bearing heat generation formulae (equation 2.5 to 2.16). Since there were two contacts per bearing and the model was built for one radian center angle, these values were divided by 4π before being applied to the model. Table 3.4 lists surface convective coefficients obtained from calculation.

Table 3.1 Spindle Surface Classification

Surface Location	Symbol	Surface Characteristics(V_s, L) [†]	
Shaft Center Hole	S1 & S1a	Both Ends Open	$V_s = 0.025 V_t$ $L = \text{Hole Length}$
		One End Open	$V_s = 0.01 V_t$ $L = \text{Hole Length}$
		Both Blocked	No Convection
Housing Outer Wall	S2	$V_s = 0.167 V_t$ $L = (\text{Length} + \text{Width})/2$	
Housing Outer Surface, Top and Bottom	S3	Same as S2, if with mounting conduction, use same value as that of S2	
Shaft Outer Surface, Outside Housing, Small Diameter	S4	$V_s = 0.0667 V_t$ $L = \text{Average Diameter.}$	
Shaft Outer Surface, Outside Housing, Large Diameter	S5	$V_s = 0.1 V_t$ $L = \text{Average Diameter.}$	
Housing End Walls	S6	$V_s = 0.2 V_t$ $L = (\text{Length} + \text{Width})/2.$	
Convective Surface Inside Housing	S7 [‡]	$V_s = 0.025 V_t$ $L = \text{Average Diameter.}$	

[†]: In the calculation, the surface wall temperature T_w and the fluid stream temperature T_f were needed. T_w was taken as estimated wall temperature, and T_f was the incoming air stream temperature under normal condition;

[‡]: Considering lubrication effect on convection, the following suggested coefficients should multiply the convection coefficient obtained:

Lubrication Coefficient

Lubrication Type		Coefficient
Oil-Air	Air: <30 psi	1.0
	Air: 30-60	1.2
	Air: 60-120	1.4
Oil-mist		1.0
Grease		0.75

Table 3.2 Spindle A Simulation Conditions

Cooling Condition (Shaft Center Hole)	Speed (rpm)	Lubricant [†] : 10 DPM Air Pressure [‡] : 35 psi	Lubricant [†] : 10 DPM Air Pressure [‡] : 75 psi
Both Ends Open	4000	1 (SA4B)	5 (SA4D)
	8000	2 (SA8B)	6 (SA8D)
One End Open	4000	3 (SA4BN)	7 (SA4DN)
	8000	4 (SA8BN)	8 (SA8DN)

- [†]: Air-oil lubrication was used in the study. The lubricant was VISTAC oil ISO 68 for all cases. 10 DPM is 10 drops per minute, equivalent to 1.0 cm³/hr;
- [‡]: Air pressure was measured pressure at air-oil producer inlet.

Table 3.3 Spindle A Heat Generation Rate[†]

Case	Front Bearing (Watt)	Rear Bearing (watt)
1, 3, 5, 7	50	43.75
2, 4, 6, 8	113.5	82.38

- [†]: Front bearing was 2MMV99120, 31 balls, 15° contact angle and steel ball, rear bearing was 2MM9117, 21 balls, 15° contact angle.

Table 3.4 Spindle A Surface Convective Coefficients (W/m²/°C)

S	case 1	2	3	4	5	6	7	8
1	55.2	65.2	10.2	18.2	55.2	65.2	10.2	18.2
1a	35.3	40.3	1.28	1.30	35.3	40.3	1.28	1.30
	43.3	40.3	0.31	0.22	43.3	40.3	0.31	0.22
	54.2	55.2	0.20	0.03	54.2	55.2	0.20	0.03
2	8.01	10.5	8.01	10.5	8.01	10.5	8.01	10.5
3	8.01	10.5	8.01	10.5	8.01	10.5	8.01	10.5
4	7.32	10.2	7.32	10.2	7.32	10.2	7.32	10.2
5	8.22	11.3	8.22	11.3	8.22	11.3	8.22	11.3
6	8.47	11.5	8.47	11.5	8.47	11.5	8.47	11.5
7	10.5	12.5	10.5	12.5	18.5	18.8	18.5	18.8

Table 3.5 Spindle A Temperature From Simulations

Location	Temperature (°C)							
	1	2	3	4	5	6	7	8
I1	33.6	44.5	38.5	50.5	31.8	42.2	34.5	45.95
I2	32.7	42.2	37.9	49.6	30.8	39.3	33.2	44.86
I3	30.9	39.0	35.6	44.0	28.8	35.1	31.2	38.97
I4	30.6	36.8	35.3	43.1	28.5	34.8	30.9	38.05
I5	33.3	41.6	37.5	46.5	31.1	38.2	33.4	41.83
I6	35.1	43.9	39.1	49.2	33.9	42.7	35.2	44.83
I7	33.9	39.1	37.9	44.5	31.9	36.2	33.5	42.84
I8	30.7	35.1	34.8	41.1	29.1	32.7	31.5	37.41
I9	33.0	41.2	37.9	49.4	31.2	40.0	34.0	44.87
K1	32.5	39.3	33.7	41.0	30.6	36.7	31.1	38.01
K2	32.8	39.9	33.9	41.6	30.9	37.0	31.4	38.65
K3	33.2	41.1	34.5	42.9	31.3	37.1	31.9	39.84
K4	32.4	39.1	33.6	40.7	30.4	35.5	31.0	37.74
K5	31.0	36.0	32.0	37.2	29.1	33.6	29.5	34.43
K6	30.9	35.8	31.9	37.1	29.1	35.1	29.5	34.37
K7	30.5	34.9	31.4	36.1	28.7	30.8	29.0	33.33
K8	29.9	33.5	30.8	34.5	28.1	32.8	28.5	31.96
K9	30.3	33.5	31.1	34.5	28.3	33.5	28.6	32.20
K10	35.2	42.6	36.8	44.9	31.4	39.9	33.7	41.49
K11	31.1	34.7	32.5	36.0	29.2	32.7	29.6	33.53

Figure 3.4 illustrates the spindle temperature profiles and the temperature transient responses at a node on the shaft's inner surface at the front bearing location (corresponding to the thermal sensor measuring point I1 as shown later in Figure 4.2) for case 1 and case 2 as defined in Table 3.3. The measurements for all 8 cases were

made with the spindle speed quickly increased from zero to the calculation speed in order to simulate the step input used in FEA calculation. The results for case 1 and 2 are illustrated in Chapter 4. All calculations and measurements show very good agreement. Most of the differences between the measured and calculated temperatures are within 1 to 2 °C.

Calculation Analysis

In Table 3.5, the locations correspond to the temperature measurement locations in Figure 4.2 (shown later). Table 3.5 lists the steady state temperatures at those locations. It can be seen that the spindle speed is a major factor influencing bearing/spindle steady state temperatures, and that lubrication air pressure has a significant effect on reducing the temperatures. This can be understood since higher air pressure forced more compressed air into the contact neighborhood. Therefore, the heat convection was improved, the contact temperature was reduced, and the oil-film thickness and strength were increased. More air inside the spindle means higher air density and larger heat capacity. More air also causes a more violent turbulent air flow, results in better convective heat transfer.

The size of the opening of the spindle shaft center hole had a very important influence in local (shaft inner surface) temperature. This is because the two ends of the shaft have different diameters, and since the centrifugal force causes air flow radially at the shaft ends, the end with the bigger diameter can throw more air into the surroundings, generating an air flow from the small diameter end to big end, as shown in Figure 3.5a. If one end is blocked, the situation is shown in Figure 3.5b, where almost no air flows through the shaft. If the shaft has the same end diameters,

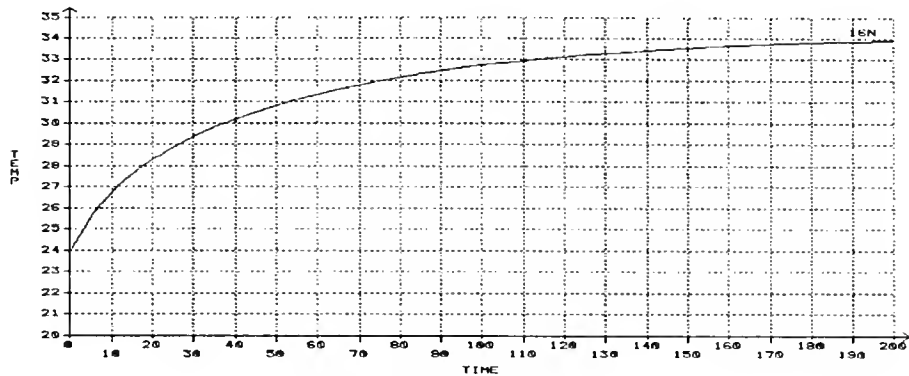
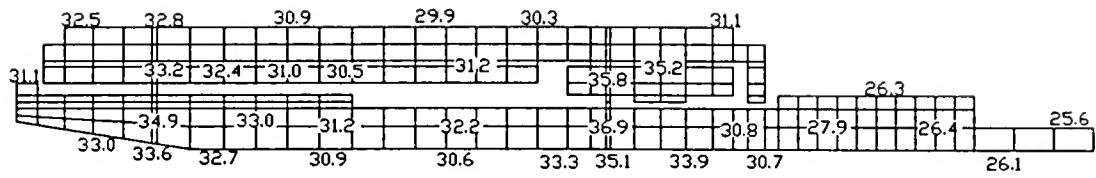


Figure 3.4a Case 1

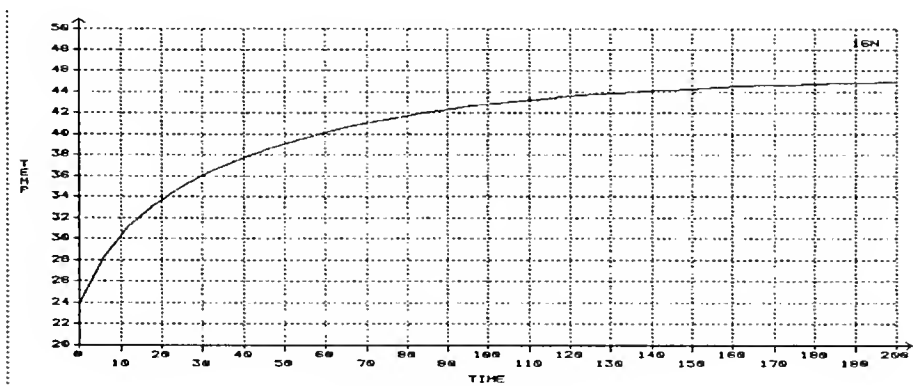
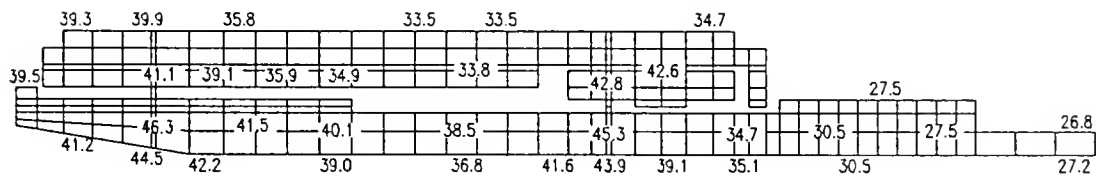


Figure 3.4b Case 2

Figure 3.4 Temperature Field and Time Response at I1:
Case 1, Case 2, Case 5, Case 6

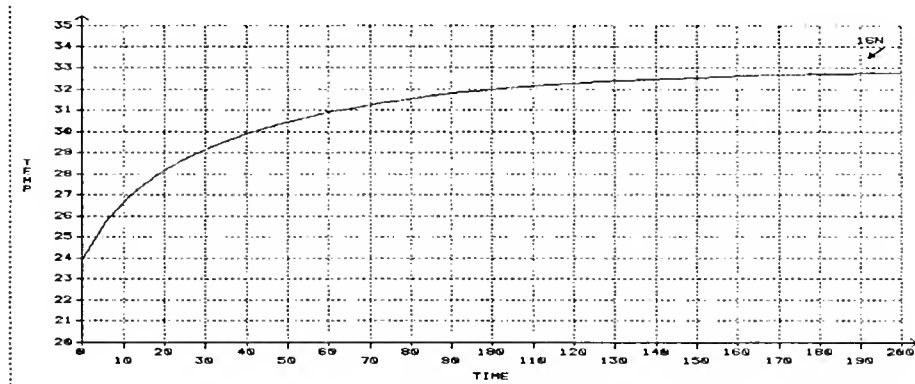
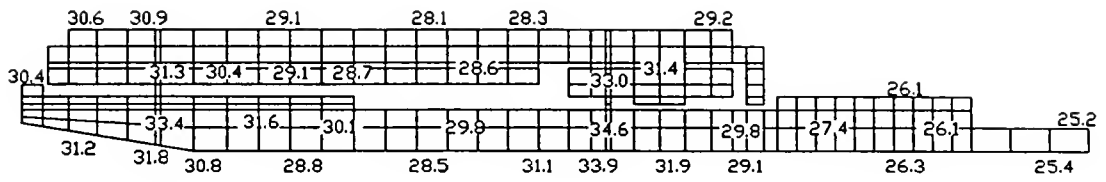


Figure 3.4c Case 5

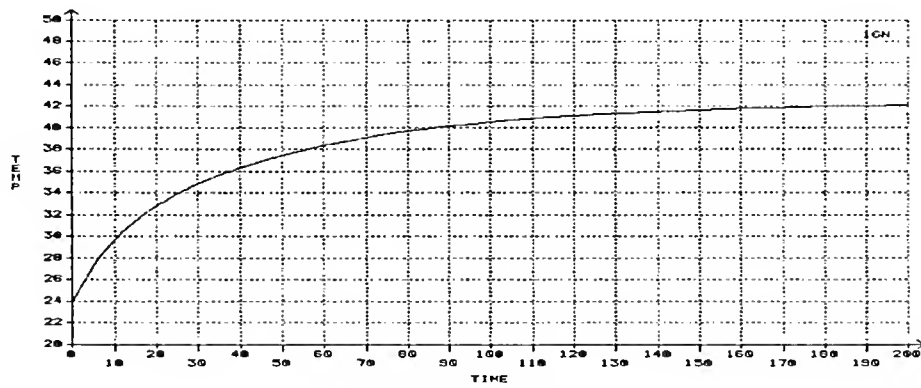
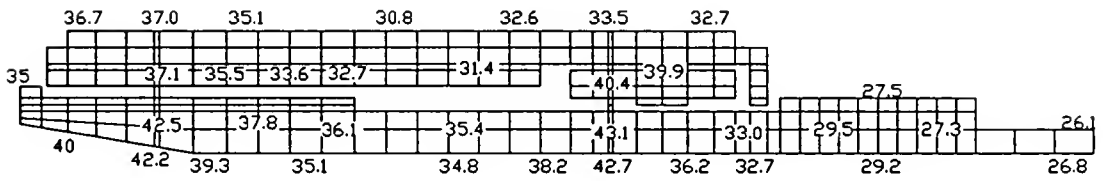


Figure 3.4d Case 6

Figure 3.4 (Continued)

the centrifugal effect will cause a surface air flow (or boundary layer flow) from inside toward the ends. In order to compensate for the air loss there, the air flows in from the hole center to supply this flow (Figure 3.5c). It can be seen from Figure 3.5c and *d* that a shaft with both ends open will have double the amount of air passing its center hole, and the air will travel only half the distance as that in a shaft with one end blocked, so a shaft with both ends open will have better hole convective heat transfer than the shaft with one end open. In addition to the increased air flow, the spindle speed also causes better convection inside the shaft hole.

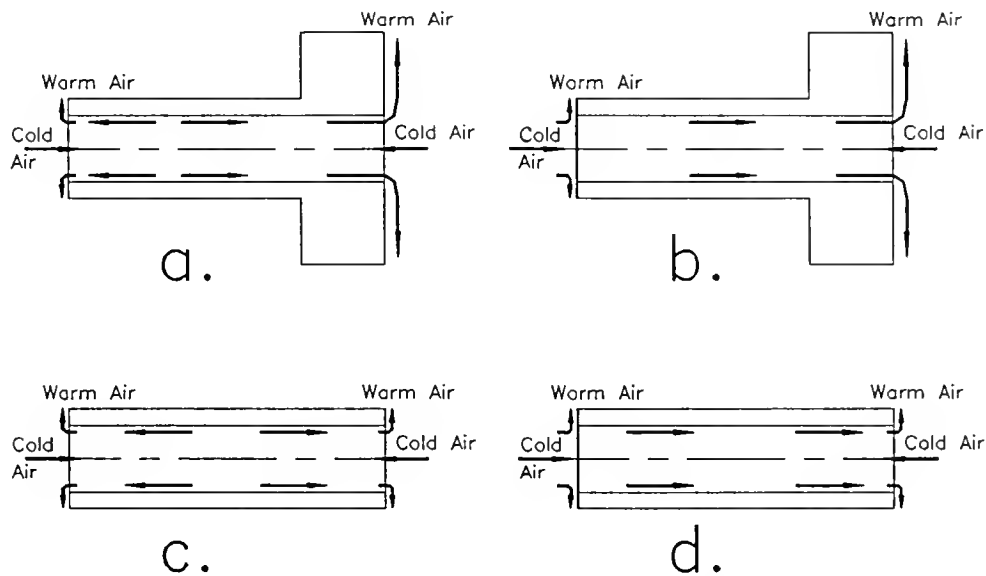


Fig. 3.5 Different Convection Situations

Table 3.6 lists the time constants for different cases at the front bearing shaft inner surface. The time constants were obtained from the local transient temperature responses of different cases. From the time constants the following conclusions may be made, 1) The spindle shaft center hole has a very significant influence on spindle temperature response, especially spindle shaft temperature

response. 2) An increase of air-oil lubrication air supply pressure from 35 psi to 75 psi results in a 15% to 50% reduction in time constant. 3) High spindle speed causes high bearing heat generation as well as large convection heat transfer. As a result, although the spindle will have a higher steady state temperature, the transient occurs over a shorter time. This is because the time constant is dictated by the heat capacity and convection ability. 4) The calculation results show that the spindle internal contact surfaces (between the bearing ring and the housing hole and the shaft surface) have a large heat conduction resistance, which is an important factor affecting the spindle temperature and temperature distribution. 5) The spindle material incongruity and physical cavities reduce heat capacity and reduce transient response time. The material properties also influence the transient temperature response.

Steady state temperature fields show that this spindle can be thermally stable at speeds over 8000 rpm, and that the spindle is naturally convected.

Table 3.6 Spindle A Time Constants From Simulations

Case	Time Constant (Min)	Comment
1	49.40	
2	27.90	High speed, fast response
3	56.47	Shaft hole partially open
4	38.85	
5	24.71	High air pressure
6	24.64	
7	31.78	
8	31.77	

Calculation of a Spindle with Bearing and Internal Motor Heat Sources

Modeling Spindle B

The structure of Spindle B is illustrated in Chapter 2, Figure 2.1. It can be seen that there is an integral AC motor and there are four angular contact ball bearings. The spindle is more complicated, smaller and faster in rotational speed than Spindle A. The simplification process was more difficult because the analysis result was more sensitive to the simplification. Figure 3.6 illustrates the simplified spindle structure and Figure 3.7 illustrates the meshes of this spindle model. The spindle was about 510 mm long and 280 mm tall. Manual meshing and *PLANE2D* element were used and the nominal element size was 6 mm.

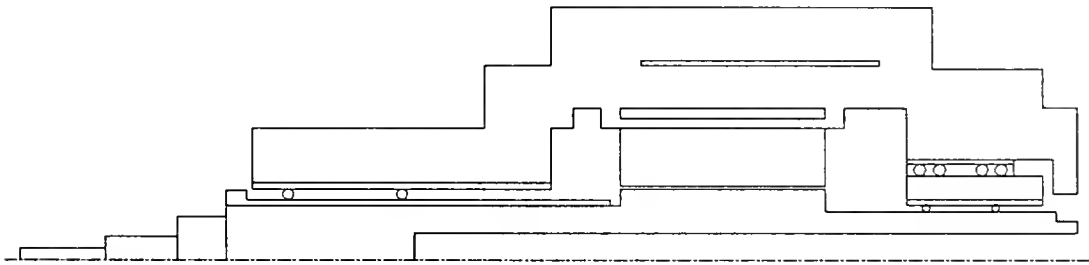


Figure 3.6 Simplified Spindle B Structure

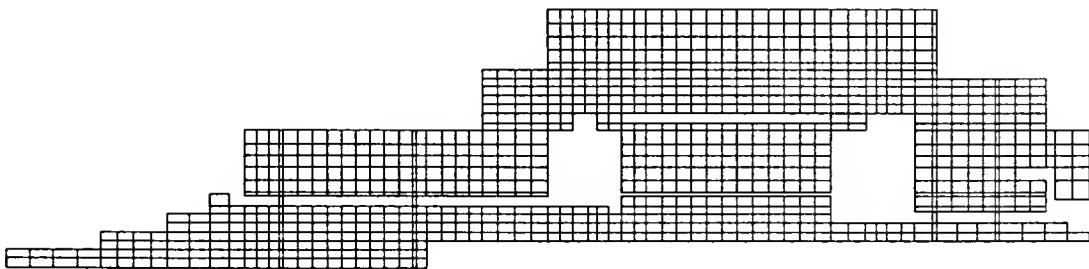


Figure 3.7 Meshes of Spindle B

Spindle B has both bearing heat sources and a motor heat source. Thus, the thermal load includes both nodal heat and element heat. The spindle speed range of interest is well over 5000 rpm, and both computational and experimental results indicate that spindle speed influence on the convective coefficients of Spindle B is not as important as that in Spindle A.

Calculation Cases

In the calculation of spindle B, the variables studied were spindle speed, cooling effect and spindle axial preload. The calculation was done for spindle axial preload of 100 lbs, 150 lbs, 170 lbs, and 220 lbs, spindle speed every 5000 rpm from 5000 rpm to 50,000 rpm, and with and without water cooling of the bearing outer ring. The results discussed in this text are from the calculation with 150 lbs preload unless otherwise specified. In Table 3.7 the bearing heat generation rates for the calculation cases and the estimated motor heat generation rates are listed. The motor heat generation rates were obtained from the AC motor power measurement for the speed from 5000 rpm through 25,000 rpm (Appendix B). For speed from 30,000 rpm to 50,000 rpm, the motor heat generation rates used were from extrapolation (polynomial curve-fitting) of the measured result. In Table 3.8 convective coefficients are listed. For air-cooling surface convection, smaller coefficients correspond to lower spindle speeds and large coefficients correspond to higher spindle speeds. For water-cooling surface convection, larger coefficients were selected for low water temperatures and high flow rates. Figure 3.8 shows the spindle steady-state temperature profiles for the following speeds: 15,000, 25,000, 35,000 and 45,000 rpm. Some of the steady-state temperature-speed relation curves

(the temperature at the bearing race contacts, outer ring surface, spindle arbor and rear bearing roller-cage) are illustrated in Figure 3.9. In that figure, "F#1" and "F#2" are front first and second bearings, and "R#1" and "R#2" are rear first and second bearings, "inner" and "outer" designate the inner-race and outer-race of the bearings. The corresponding measurements will be shown in Chapter 4.

Table 3.7 Spindle Bearing and Motor Heat Generation Rates[†]

Speed (×1000) (rpm)	Bearing Heat Generation Rates (Watts/bearing) (front/rear)				Motor Heat Rate (rotor/stator) (Watts)
	100 lb	150 lb	170 lb	220 lb	
5	13.87/5.03	13.94/5.53	14.36/5.91	14.73/6.66	82.4/142.1
10	23.79/7.92	29.81/12.9	30.10/13.6	33.26/16.7	173.5/299.2
15	85.7/25.26	76.43/26.0	77.2/27.27	70.0/29.41	274.9/474.2
20	99.7/29.91	89.57/37.2	90.73/39.0	95.5/40.21	386.6/666.9
25	152.6/56.8	135.3/56.7	137.2/59.6	141.1/66.1	508.7/877.4
30	183.1/71.3	188.4/78.9	191.0/82.7	196.2/91.2	641.0/1106
35	235.4/100	242.8/110	246.2/115	252.8/126	783.7/1352
40	307.6/133	317.7/147	322.2/153	330.9/167	937.0/1616
45	388.6/184	402.0/201	407.8/210	418.7/226	1100/1898
50	490.5/258	508.1/279	515.5/289	529/309.1	1273/2197

[†]: Front bearing RHP B7012, 18 balls, rear bearing RHP B7909, 20 balls, all bearings had silicon nitride balls and 20° contact angle.

Figure 3.8 Spindle B Temperature Profiles

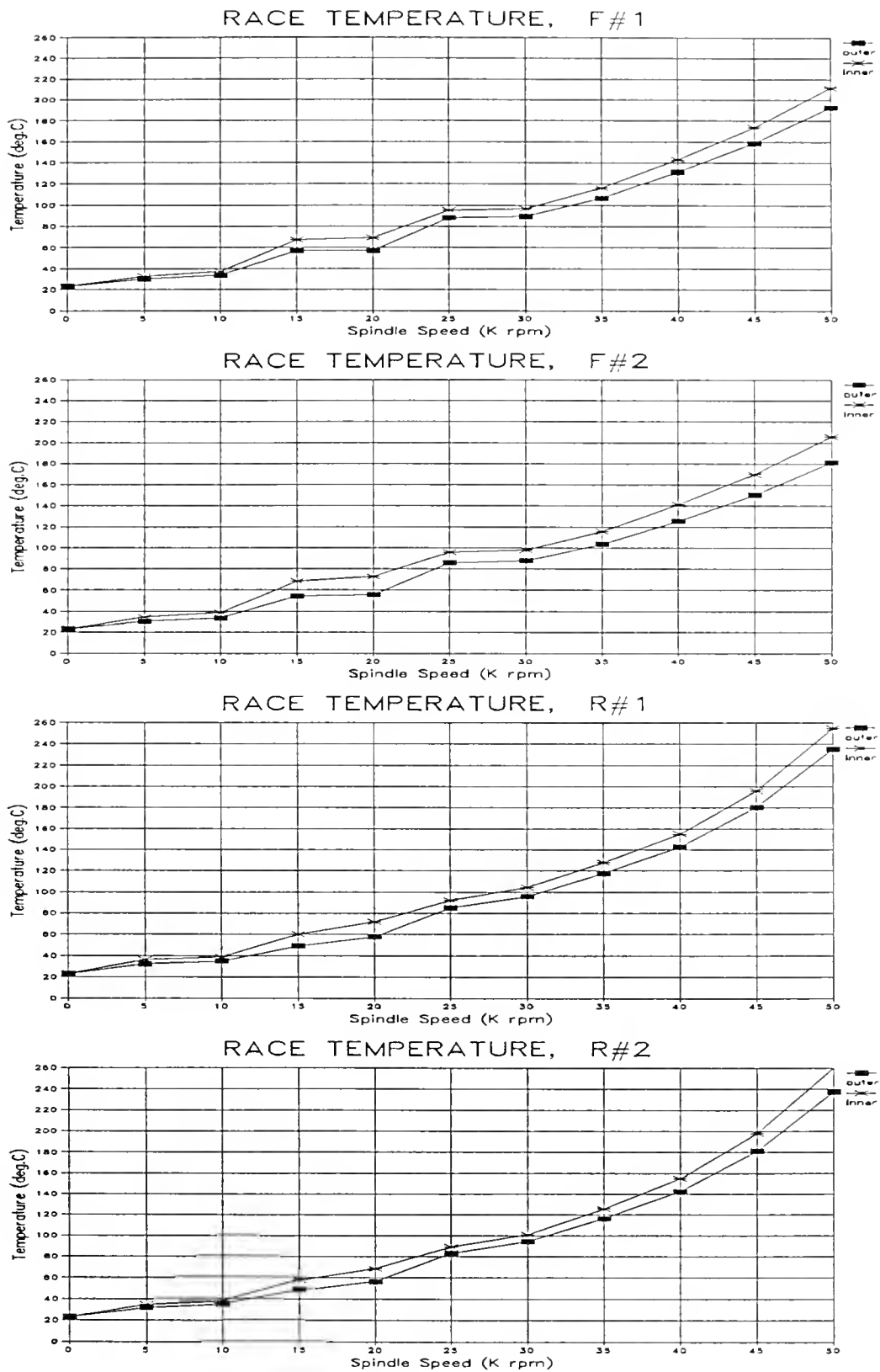


Figure 3.9 Spindle B Temperatures

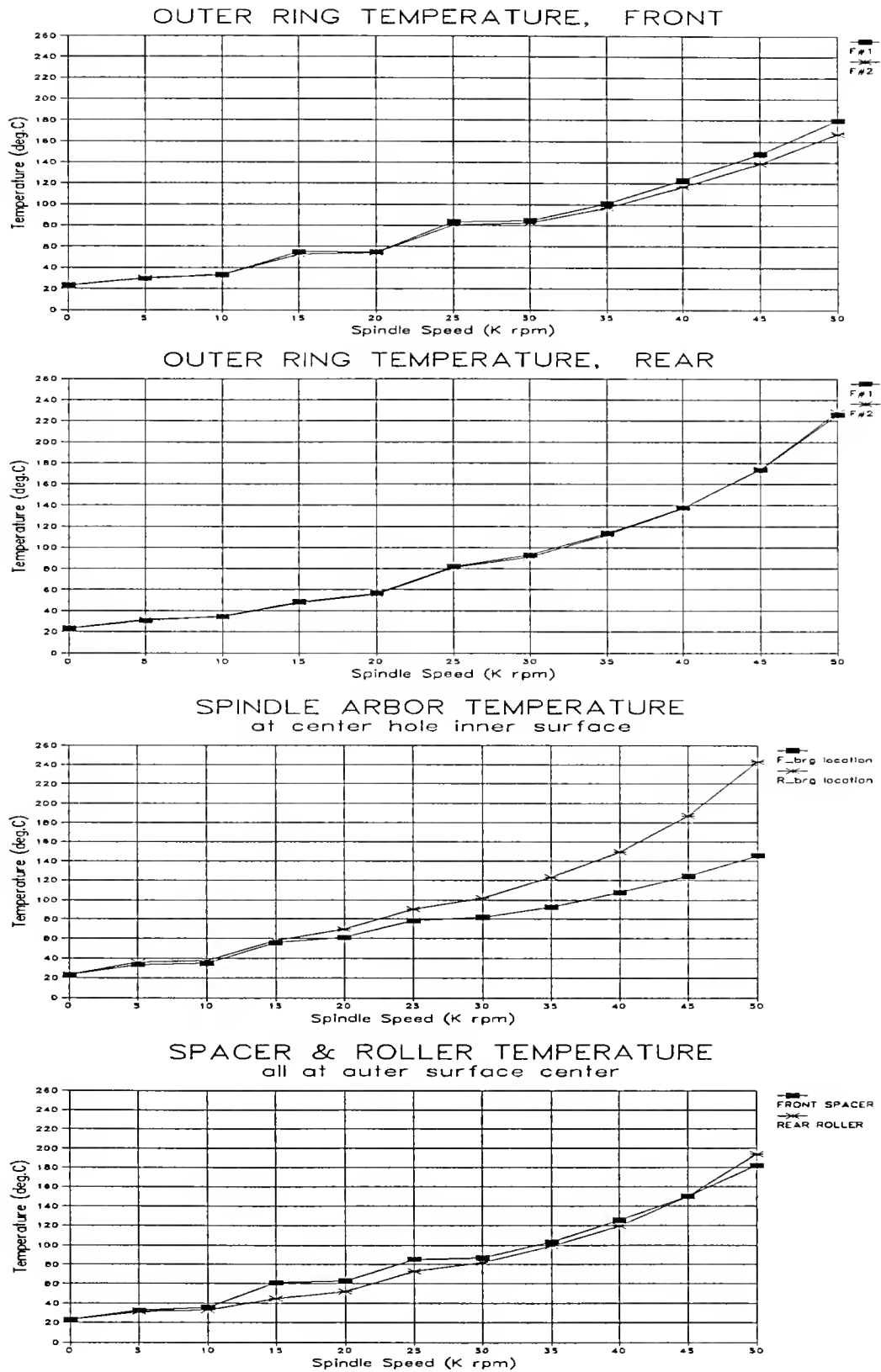


Figure 3.9 (continued) Spindle B Temperatures

Table 3.8 Spindle B Convective Coefficients

Convection Surface Location	Value (W/m ² °C)
Spindle arbor center hole, near opening	20 - 30
Spindle arbor center hole, away from opening	8 - 15
Spindle rotating shaft, outside housing	35 - 60
Housing wall, near rotating part(s)	30 - 60
Housing side wall, away from rotating part(s)	20 - 40
Surface inside housing	0.5 - 2.0
Motor water cooling surface	450 - 550
Bearing water cooling, equivalent surface	150 - 200

Calculation Analysis

From Figure 3.8 it can be seen that the bearings and motor rotor conductors have higher temperatures than the other spindle parts, indicating that the motor and bearing heat generations play an important role in limiting the maximum speed. The motor rotor conductors have the highest temperature, however the motor rotor material can withstand higher temperatures than bearing components. At high speeds, the bearing temperature increases very rapidly with the speed and finally limits the spindle speed. This is because, as the spindle speed increases, the bearing heat generation increases exponentially, as shown in Figure 2.7. Since the rear bearings were inside the roller cage, which has low heat conductivity, and the rear bearings were close to the motor rotor, the rear bearings had higher temperatures than the front bearings.

Figure 3.9 illustrates the relationship between the steady-state temperatures and the spindle speed. It is shown that the temperatures increase exponentially with

spindle speed and the race temperature is 100°C at about 30,000 rpm. This temperature (100°C) was considered as maximum bearing temperature, since higher temperatures would deteriorate the lubricant, or reduce the strength of the bearing cage. The remains of the decomposed oil would stay on the race, further deteriorate the lubrication and cause the bearing to generate more heat. Such temperature-related lubrication deterioration was not modeled in this work.

Since the rear bearings had very high race temperatures, if higher spindle speed is desired, the rear bearing assembly should be modified. To lower the bearing temperature, the motor can be relocated in a position farther from the bearings, or special cooling method can be used to remove more heat from the bearings. To achieve higher spindle speed, the high motor rotor temperature also needs to be reduced. This can be done by using a higher efficiency motor or by increasing the heat transferred from the motor. Since this structure (internal motor is between the bearings) allowed motor heat generation to dissipate through bearing locations, motor power loss directly resulted in the high bearing temperatures.

CHAPTER 4 SPINDLE TEMPERATURE FIELD MEASUREMENT

Thermoelectricity and Thermal Radiation

Thermoelectric theory states that if a conductor is heated at one end, there will be an electric potential gradient along the conductor. This thermoelectric potential varies for different metals and alloys. A thermocouple is a pair of different metal or alloy wires which are joined together at one end to form a junction. When the temperature at the junction is higher (or lower) than that at the other end of these wires, the difference of the potentials at the other ends indicates the temperature of the junction relative to the other ends. With a temperature reference, the thermocouple can be used for temperature measurement. Since the measurement junction should be at the same temperature as the measured object, there should be good contact between the hot junction and the target.

The temperature measurement of a moving surface is usually done by radiation thermometry. The thermal radiation from a blackbody can be expressed in terms of spectral radiance L_λ as used in reference [40]. The spectral radiance is defined as the radiant flux (i.e. rate of energy flow) propagated in a given direction per unit solid angle about that direction and per unit area projected normal to that direction. The spectral radiance also depends on temperature and wavelength, as suggested in the Plack distribution law[40]:

$$L_{\lambda} = C_1 \pi^{-1} \lambda^{-5} [e^{\frac{C_2}{\lambda T}} - 1]^{-1} \quad (4.1)$$

The maximum is at

$$(\lambda T)_{\max} = 2898 \text{ } \mu m K \quad (4.2)$$

where L_{λ} : Spectral radiance, $W \cdot cm^{-2} \cdot \mu m$;

λ : Radiation wavelength, μm ;

T : Absolute temperature (K);

C_1, C_2 : Coefficients.

Practical materials follow the same law but on a different scale. In the application of the radiation theory to temperature measurement, emissivity (ϵ) is used, which is defined as the ratio of energy emitted by an object to the energy emitted by a blackbody at the same temperature. Emissivity depends upon the material and surface texture. Since, with the same emissivity, the energy emitted from an object depends on the temperature, the temperature can be obtained by measuring this energy. Because the wavelength of thermal radiation covers a wide range, from $0.760 \text{ } \mu m$ to $1000 \text{ } \mu m$ in the electromagnetic spectrum, radiation thermometry can use energy over different frequency ranges to measure temperature. However, the most commonly used wavelength is usually from 5 to $20 \text{ } \mu m$ due to the high spectral energy in this range.

The spindle temperature is usually in the range from approximately 300 K to 450 K . Equation (4.2) shows that the radiation peak is between 9.66 to $6.44 \text{ } \mu m$ for this temperature. Since a hot object radiates more energy than a cold object, it is

easier to measure higher temperatures. Radiation attenuation through a media is determined by the wavelength, and long wavelength radiation has a high attenuation. For high temperature measurements, since the radiation is strong, the measurement can be done at high frequency, and the radiation loss is small. Then many materials can be used to make the sensor head small and to transmit radiation over a long distance before the radiation is converted into an electrical signal. For low temperature measurements on the other hand, the strong radiation peak is in the low frequency range. To avoid losses, the radiation is directly converted into an electrical signal without any media other than air. In the sense of thermal radiation, the spindle temperature is in the low temperature range.

Type K (Ni-Cr/Ni-Al alloys) thermocouples were used for measuring the temperature of non-moving surfaces, and an infrared temperature sensor was used to measure the spindle arbor center hole surface temperature. The infrared sensor used was a 3000AH Microducer manufactured by Everest Interscience, Inc.. This sensor has a scale range of -30°C to 1100°C , with a resolution of 0.1°C , and a spectral pass band (wavelength range) from 7.0 to $15.0\ \mu\text{m}$. The diameter of the spindle arbor center hole is 1.05 inches, and the sensor, claimed as the world smallest infrared sensor in their literature, still has dimensions of $\phi 0.625 \times 2.25$ square inches. Because of the limited room, the measurement cannot be accomplished by directly aiming the sensor at the surface. Also since noncontact infrared sensors always use an optical window that has a field of view, the measurement should be made at a distance as close to the target as possible so the local temperature will be obtained, otherwise, the measured temperature will be an average over a larger area. To

overcome these difficulties the sensor was assembled as shown in Figure 4.1, where the sensor was in an axial orientation with a front surface gold-plated mirror placed in front of the sensor at 45° angle to reflect infrared radiation from the measured surface into the sensor window. This mirror has a reflection efficiency of 95% - 98% for infrared radiation. The total distance from target to the sensor window was about 1.5 inches.

Measurement of a Spindle with Bearing Heat Sources

Figure 4.2 illustrates the locations of the temperature measurement for Spindle A with thermocouples and the infrared sensor. Since there was only one infrared sensor, in the measurement, the sensor was moved between I1 through I9 locations. Steady-state temperatures were measured for each of these points and the transient temperatures were measured at most of the locations. The temperature fields of the cases in Chapter 3 (Table 3.2) were measured. The temperature profiles and transient responses, corresponding to the results in Figure 3.5, are illustrated in Figure 4.3. In Figure 4.3 cases 1 and 2 were measured for lubricator air pressure 35 psi, at 4000 rpm and 8000 rpm respectively. Cases 5 and 6 were for air pressure 75 psi, at 4000 rpm and 8000 rpm respectively. Table 4.1 lists the time constants from the measured transient response and Table 4.2 lists the temperatures measured at specific points for each case. The data in Tables 4.1 and 4.2 correspond to those listed in Tables 3.6 and 3.7.

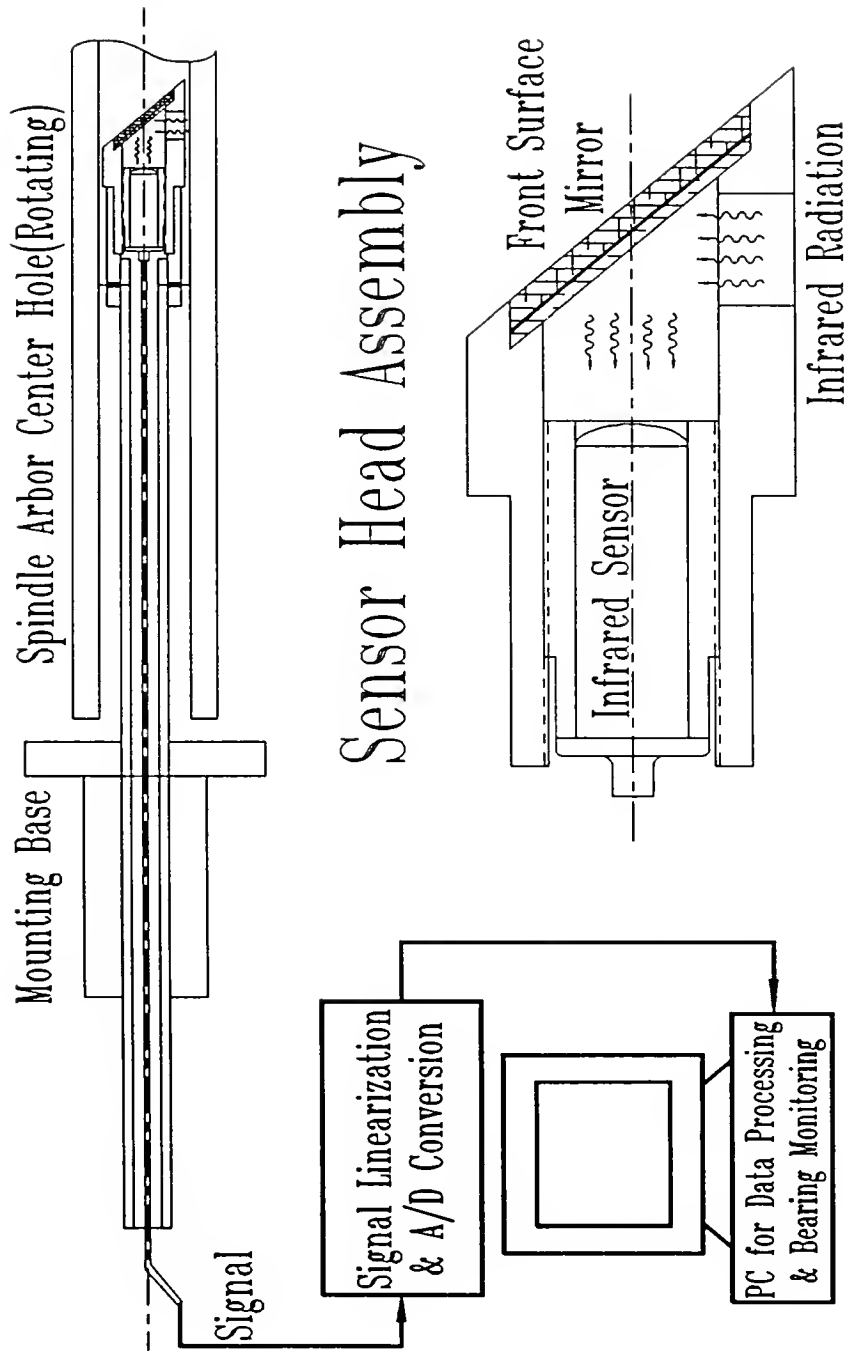


Figure 4.1 Infrared Sensor Assembly and Arrangement

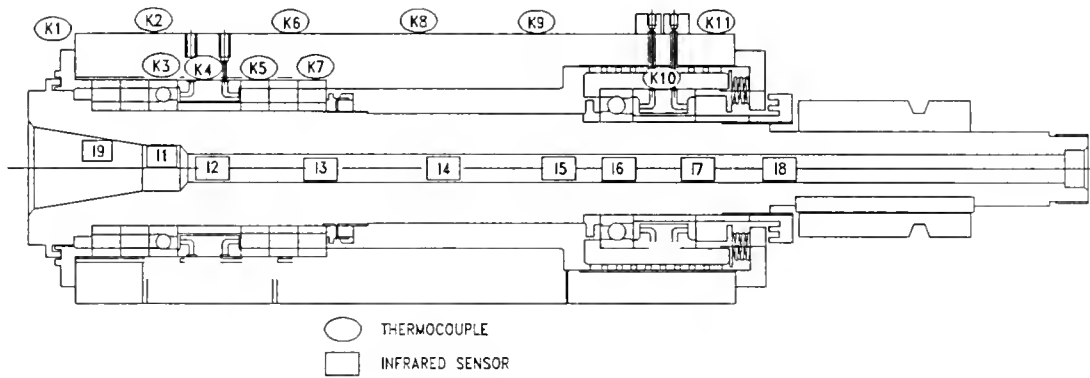


Figure 4.2 Sensor Arrangement for Temperature Measurement

Table 4.1 Spindle A Measured Time Constants

Case	Time Constant at I1 (Min)	Curve Shape
1	52	
2	41	
3	52	
4	25, 40	Clear overshoot peak
5	33	
6	15	Fast response, Overshoot peak not clear
7	35	
8	22, 35	Clear overshoot peak

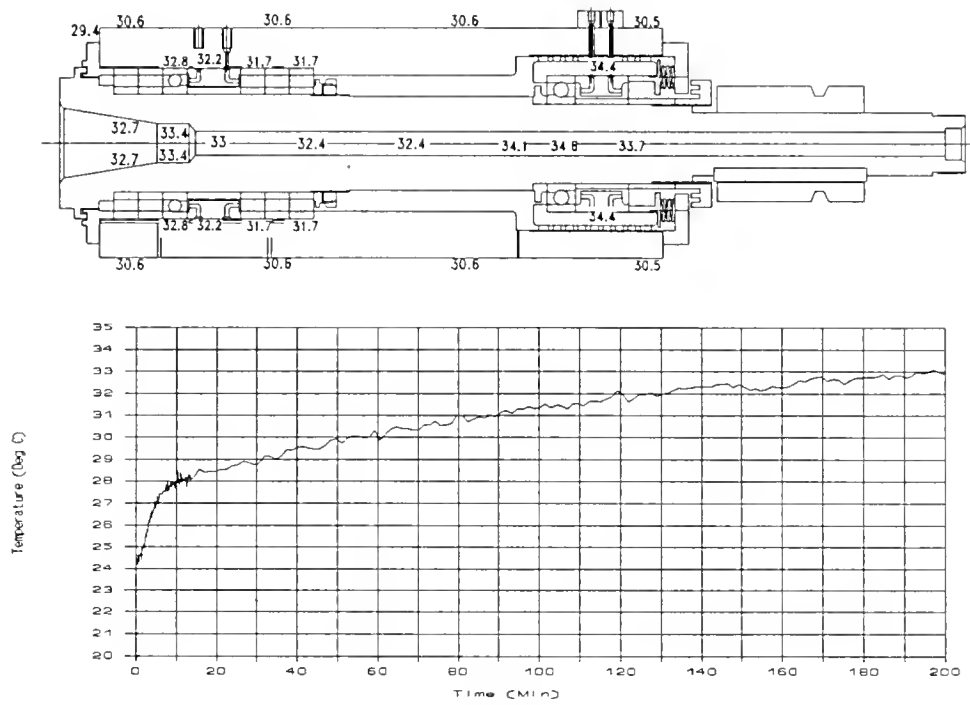


Figure 4.3a Case 1

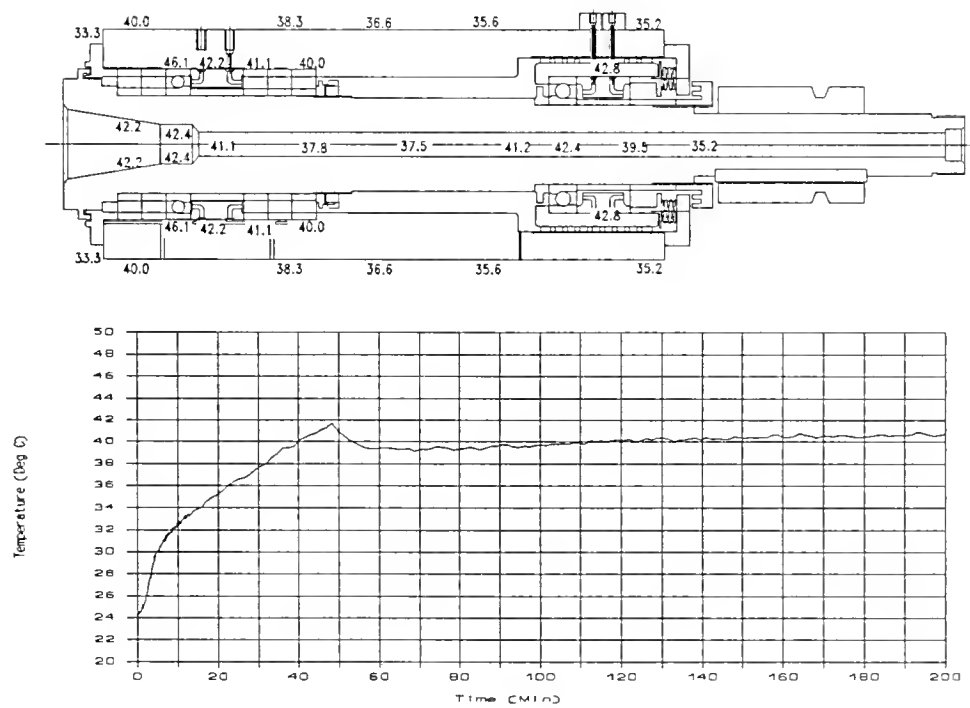


Figure 4.3b Case 2

Figure 4.3 Temperature Measurement for Case 1, Case 2, Case 5, Case 6

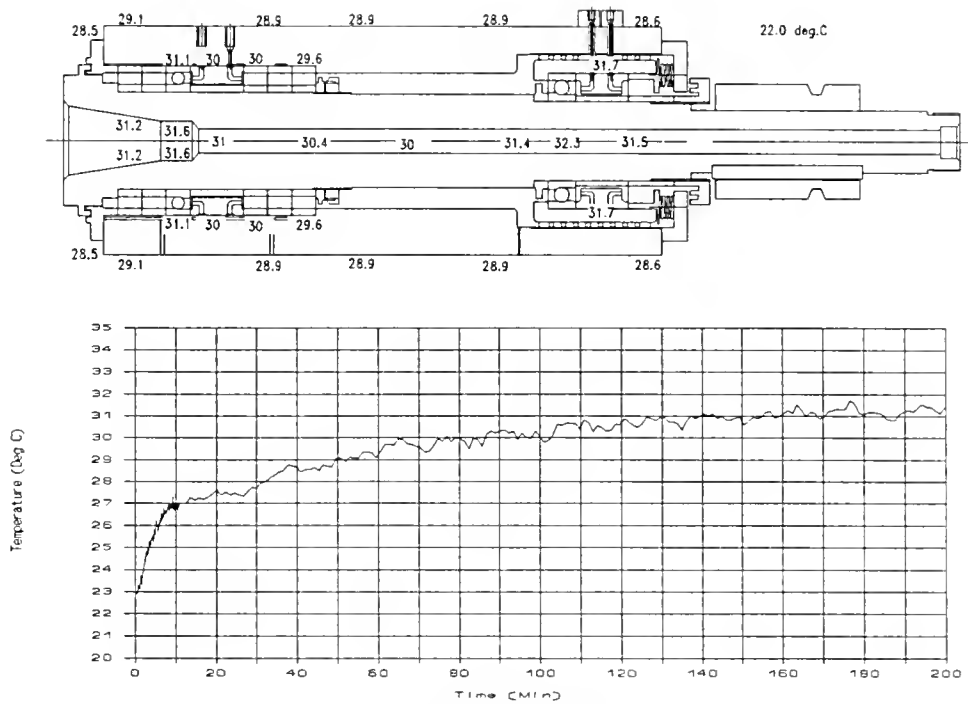


Figure 4.3c Case 5

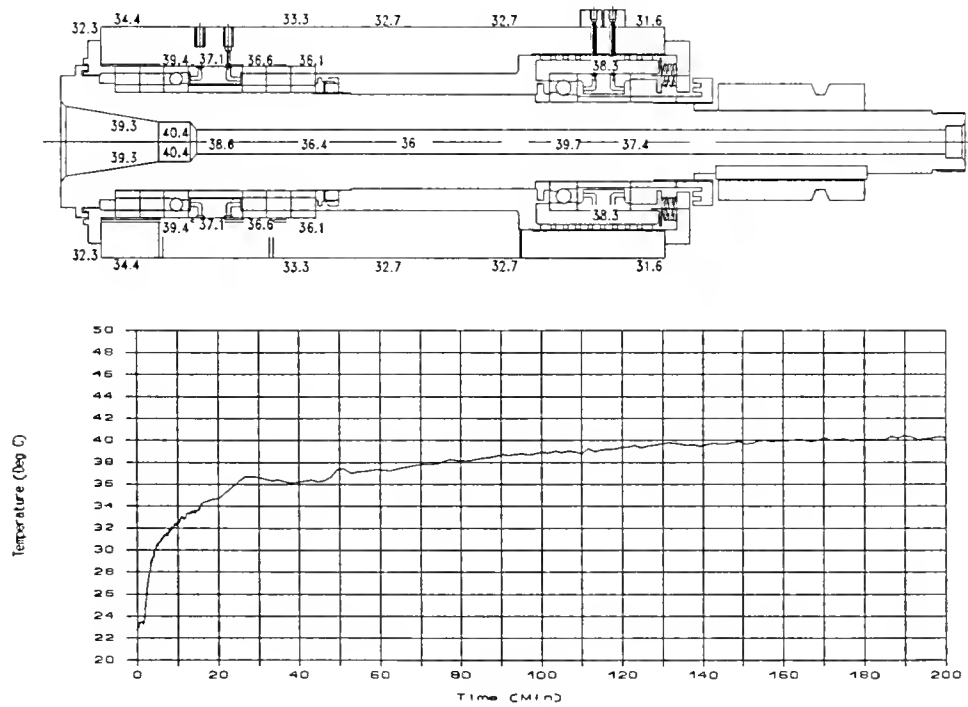


Figure 4.3d Case 6

Figure 4.3 (Continued)

Table 4.2 Spindle A Measured Temperature

Location	Temperature (°C)							
	1	2	3	4	5	6	7	8
I1	33.4	42.4	38.8	48.9	31.6	40.4	34.3	45.8
I2	33.0	41.1	39.8	50.3	31.0	38.6	34.9	47.6
I3	32.4	37.8	38.7	47.6	30.4	36.4	34.0	44.9
I4	32.4	37.5	37.8	46.6	30.0	36.0	33.6	44.0
I5	34.1	41.2	40.4	49.4	31.4	N/A	35.5	46.6
I6	34.6	42.4	40.8	50.6	32.3	39.7	36.4	47.6
I7	33.7	39.5	39.3	47.8	31.5	37.4	35.5	44.9
I8	N/A	35.2	N/A	41.2	N/A	N/A	N/A	N/A
I9	32.7	42.2	36.4	45.3	31.2	39.3	32.2	41.6
K1	29.4	33.3	32.2	35.0	28.5	32.3	29.4	32.9
K2	30.6	40.0	33.3	41.1	29.1	34.4	30.0	35.6
K3	32.8	46.1	36.1	47.2	31.1	39.4	32.2	40.6
K4	32.2	42.2	35.0	42.7	30.0	37.1	30.7	38.3
K5	31.7	41.1	34.6	41.1	30.0	36.6	30.1	37.9
K6	30.6	38.3	32.2	39.4	28.9	33.3	29.4	35.6
K7	31.7	40.0	33.8	41.1	29.6	36.1	30.0	37.4
K8	30.6	36.6	31.6	37.9	28.9	32.7	29.2	34.4
K9	30.6	35.6	31.6	36.6	28.9	32.7	29.2	33.9
K10	34.4	42.8	35.5	43.8	31.7	38.3	32.2	39.4
K11	30.5	35.2	31.2	36.2	28.6	31.6	28.9	33.1

N/A: not available.

Measurement of a Spindle with Bearing and Internal Motor Heat Sources

The locations of the thermocouples and the infrared sensor in spindle B are illustrated in Figure 4.4. The measurements were made for the speeds from 5000 to

25,000 rpm and the axial preload 100, 150, 170 and 220 lbs. Since this spindle has a much larger speed range than Spindle A, the transient responses were measured by increasing spindle speed in multiple steps. Every time the speed was increased by 5000 rpm and the transient temperatures were measured. When a steady temperature field was achieved, the speed was increased by another 5000 rpm. Figure 4.5 illustrates two measured temperature fields at 15,000 rpm and 25,000 rpm which correspond to the calculation cases at the same speeds in Figure 3.9. Figure 4.6 illustrates the temperature-speed relationships at different locations, which also correspond to the calculation results in Chapter 3. The computed temperatures at the same points are also plotted in Figure 4.6. In the plots "f#1" indicates the calculation result of the first front bearing, "r" indicates the calculation result of the rear bearing. The curves symbolized with "f#1_M", "f#2_M" and "test" are from the measurement results. The rest of the curves are the calculation results, which are plotted here to compare with the measured temperatures.

Figure 4.7 illustrates a typical transient temperature response for the axial preload of 170 lbs and at 8000 rpm. The temperature was measured at location T9 and the spindle was started from 0 rpm to 8000 rpm. The noise in the temperature signal was due to the interference of the spindle's internal motor. Unlike Spindle A, Spindle B temperatures did not have an overshoot. The curve shows that the response has three stages, i.e., rapid increasing, slow increasing, and slow decreasing to approach a steady value. Since the curve is not smooth, and the discontinuity could only result from the change of heat sources, it can be concluded that the constant bearing load mechanism of Spindle B still has some nonlinearity.

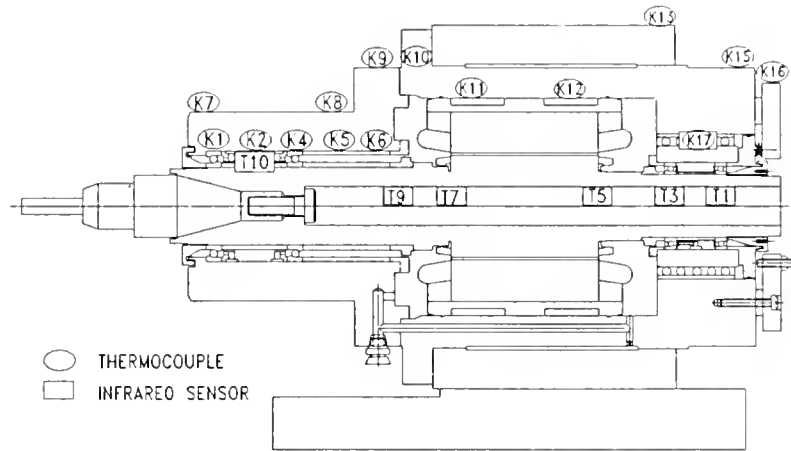


Figure 4.4 Sensor Locations for Temperature Measurement of Spindle B

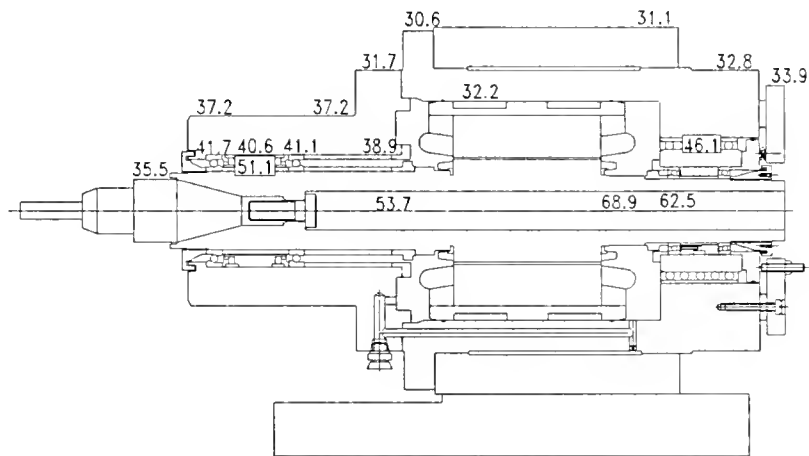


Figure 4.5a 15,000 rpm

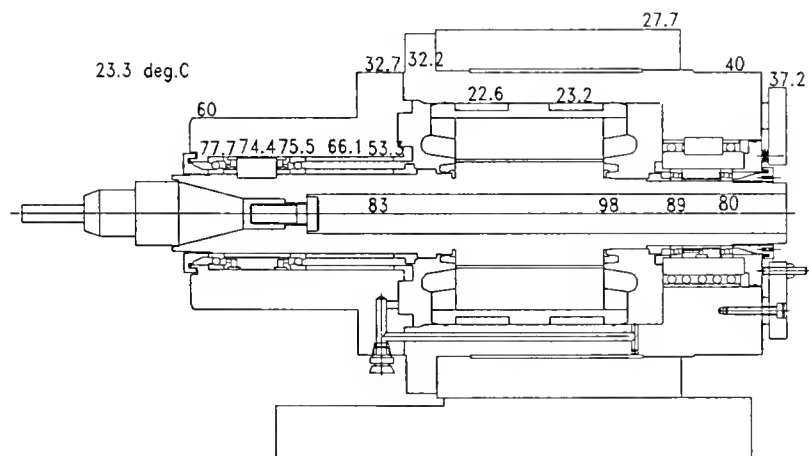


Figure 4.5b 25,000 rpm

Figure 4.5 Measured Temperature Field at 15,000 rpm and 25,000 rpm

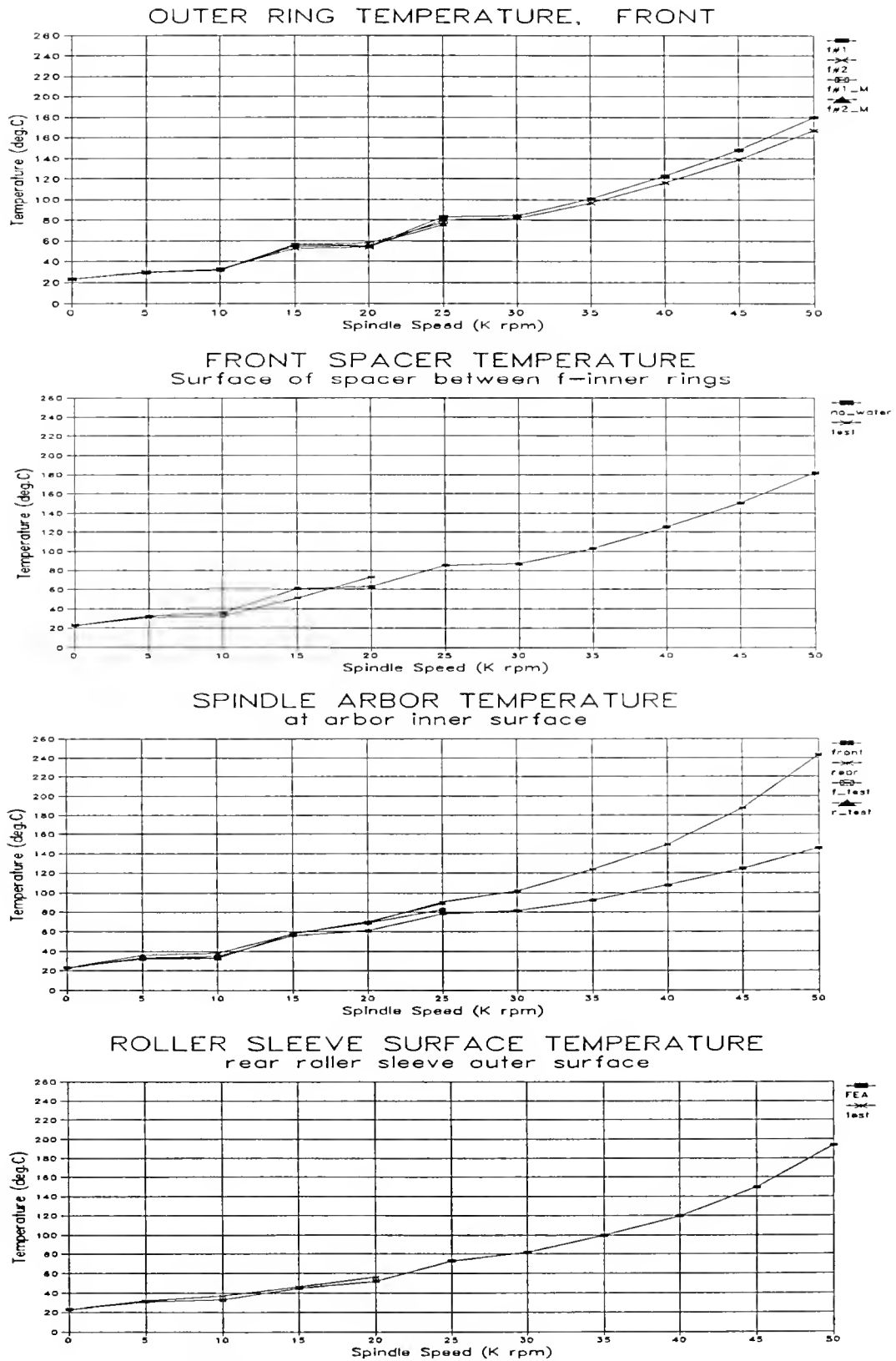


Figure 4.6 Measured vs. Calculated Temperatures for Spindle B

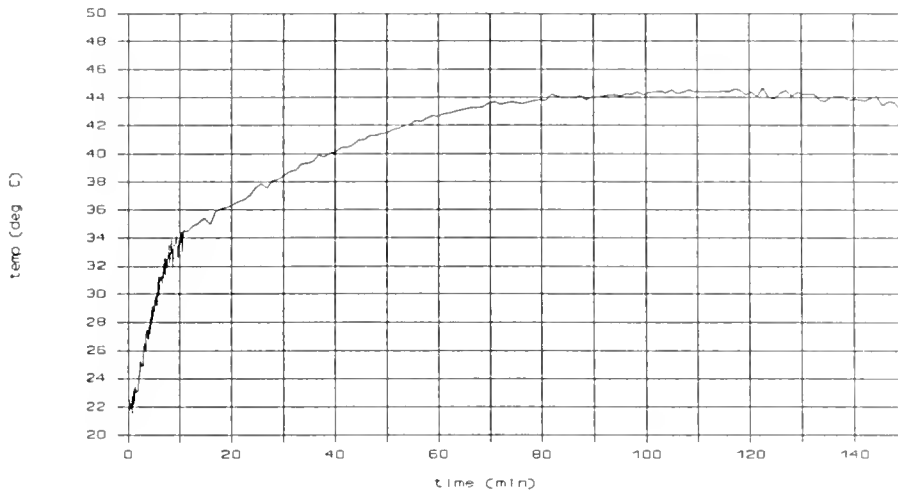


Figure 4.7 Transient Temperature Response, 8000 rpm

Comparison with FEA Results and Discussion

Spindle A. Comparing Tables 4.1 and 4.2 with Tables 3.6 and 3.7 it is shown that the FEA results are fairly close to the measured results. It should be noted that the material properties of the roller-cage and most of the convection coefficients were adjusted to make the simulation results match the experimental results. The convection coefficient adjustments were integrated into convective coefficient formulae, and the obtained roller-cage properties can be directly used for other similar structures without substantial error, for example, for Spindle B. The effects of spindle speeds and air supply pressures on spindle temperatures and time constants behaved like those predicted by FE model (Chapter 3). Since different spindle speeds caused different air flow speeds along spindle housing surface, the convective coefficients at different speeds were different. Higher lubricator inlet air pressure could force more air to pass the housing internal cavities, and better

convection resulted. If we compare the temperatures of case 2 and case 6 (or case 4 and case 8), we can see the change of air pressure from 35 psi to 75 psi caused 2 to 6 °C decrease in temperature, which is equivalent to a result from a speed change of about 1000 rpm.

The difference between the measured temperatures and time constants and the calculated temperatures and time constants seem to be the result of following three effects. First, the surfaces at different locations had different local convection coefficients that greatly depended upon the local air flow and temperature conditions. The local air flow cannot be accurately calculated. The coefficients used in the calculation were estimated average coefficients. Second, the spindle material local heat conduction resistance could not be expressed and included in the finite element model at this time. Third, the material properties (heat conductivity and capacity) could only be obtained as approximate values. The major difference between the calculated and the measured transient temperature responses exists in the appearances of the transient response curves. The calculated transient responses are all smooth curves, but the measured responses have apparent overshoots, which can be interpreted as the result of nonlinear heat sources. At high heat generation rates and in low convection in the shaft center hole there is an overshoot peak occurring shortly after the spindle is started, occurring at a time very close to the calculated time constant. The peak not only occurred in the infrared sensor measurements inside the center hole of the spindle shaft, but also appeared in the thermocouple measurements in the spindle housing. These temperature overshoots are apparently the result of the bearing heat generation rate not being constant. As the spindle

warmed, the spindle shaft expanded more than the housing, because the friction between the spindle housing and rear bearing roller-cage slowed the constant axial load mechanism's reaction to compensate for the heat induced axial load, the bearing axial load increased. The heat generation continued to increase with the temperature until the heat induced axial load was large enough to overcome the friction. In the meantime, because the shaft slowed down its expansion while the housing continued to expand, there was a small release of bearing axial load. Then the actual axial load and heat generation became smaller and the area around the bearing contacts had a temperature reduction such that the temperature gradient was changed. In some parts of the spindle the temperatures appeared to stop increasing or to start decreasing until a new thermal equilibrium was achieved. This also showed that the existence and effectiveness of the bearing constant axial load mechanism are very important.

Spindle B. Comparison of the measurements with the FEA results in Chapter 3 shows good agreement. The computed temperature fields are close to the measured temperature profiles as compared in Figures 3.10 and 4.5, and the calculated temperatures at some important points are fairly close to the measurements as shown in Figures 3.11 and 4.6, the temperatures at bearing outer rings and arbor outer surface). The sources for the remaining differences are the same as those for Spindle A.

In Figure 4.6 the first graph displays the computed temperatures for the outer rings. The graph for the front bearings also includes the measured values at K1 and

K4, marked "_M". The outer rings of the rear bearings are not accessible for measurement. The second graph plots the temperatures of the spacer between the front bearings (T10), the third graph plots the temperatures of the surface of the roller-cage (K17), and the fourth plots the temperatures in the hole of the spindle arbor (T9, T3), all of them as computed and as measured. However the measured data apply only to speeds up to 25,000 rpm, whereas computations were made up to 50,000 rpm. The measurements and computations both show that the bearing outer rings and inner rings have different temperatures and that the differences increase with the speed.

The transient temperature shows some characteristics similar to those of Spindle A. The transient curve is smooth, this suggests that the rear roller-cage moves freely. The fast rising portion of the curve is due to the change of the bearing heat generation. In the next portion, the shaft's thermal expansion applied substantial load on the bearings and the heat generation rate was slowly increasing. At this time, the shaft expanded more than the housing. After a certain time the housing expanded more than the shaft, the bearings were released and heat generation rate decreased. In the transient curve, it is shown as a slow decrease in the temperature. Since the housing expansion was limited, this decrease of temperature was small and the temperature finally reached a steady value. Since the constant bearing load mechanism was very effective, the above bearing load change was very small.

The transient temperature also shows that the spring constant load mechanism still could not provide constant bearing axial load when the temperature difference

between the shaft and the housing was large. If the housing has good cooling, such as water cooling, the bearings will have a significant thermal load, and in the design this thermal load should be considered. The bearings were arranged as DF (face-to-face) tandem, and a shaft expansion larger than the housing expansion would cause significant bearing load increase if the constant axial load mechanism was not effective.

Another phenomenon observed in the measurement is the slow temperature increase when spindle speed changed from 15,000 rpm to 20,000 rpm. In contrast to this slow temperature rise, the temperature increase for spindle speed change from 10,000 rpm to 15,000 rpm was quite large. An explanation is that the bearings were previously slightly damaged at 16,000 rpm by bearing seizure. The seizure caused surface flaws in the races of the bearings at the contact angle corresponding to this speed. When the spindle was not running at the speeds around 16,000 rpm, the bearing balls contacted the races in the good tracks, and the friction was moderate. Then when the speed was around 16,000 rpm, the balls contacted the races in the neighborhood of the damaged tracks, the friction became large. This caused the significant high temperature at 15,000 rpm. If there were good bearings, the temperature change from 10,000 rpm to 20,000 rpm would be smooth. It can be estimated from the plots that the temperature at front bearing was about 8 °C higher than the temperature with good bearings. Since this temperature increase was not large, the damage to the bearing race was not severe.

CHAPTER 5

HIGH SPEED SPINDLE DESIGN WITH THERMAL CONSIDERATION

Currently in the design of spindles, the stiffness and power are major concerns and can be under the control of design engineers. However, the design of spindle thermal characteristics, which greatly affects the spindle properties at high speed, is largely based on experience. At high speed, the bearing generates more heat, and the spindle has higher temperature and larger thermal expansion. Special thermal design becomes necessary to remove the spindle internal heat from the bearings, and prevent the bearings from being thermally overloaded.

Spindle Static and Dynamic Properties

The spindle stiffness determines its static and dynamic properties. The stiffness can be increased by using larger bearings and larger arbor diameter, and by applying a larger preload to the bearings. The location of the bearings and the structure of the arbor can significantly influence the spindle static and dynamic properties. Most currently available spindles used in various machines and machine centers are designed to operate at speeds below or around 5000 rpm. When the spindle has to be used at higher speed, it will have a higher temperature, both its dynamic properties and structure will be influenced by the high temperature condition. Therefore, for high speed spindles thermal design becomes very important.

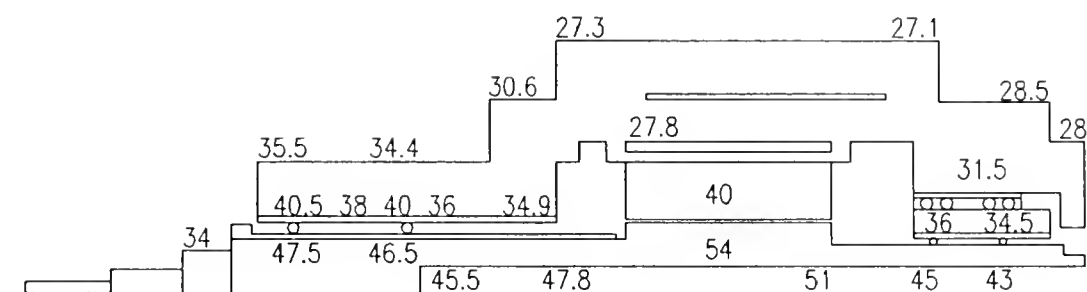
The purpose of the thermal design is to eliminate bearing thermal load, lubricant deterioration and unacceptable structural distortion, and also to maintain the dynamic properties. After a valid spindle thermal model is established, the thermal design can be processed through estimating and eliminating the bearing thermal load, reducing the high local temperatures, adjusting the bearing preload and modifying the lubrication system.

Effect of Forced Cooling on Spindle Temperature

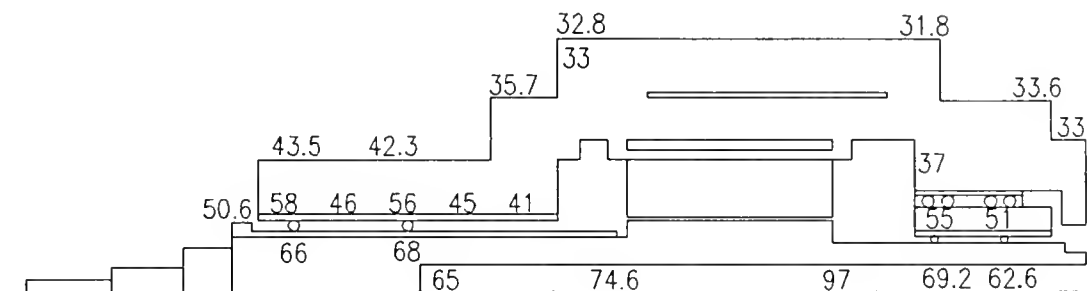
Spindle cooling is important, but the commonly used method of spindle cooling is the natural convection of the spindle surface. When the internal motor is used in a spindle, a water cooling jacket needs to be used to remove the heat generated from the motor stator. Forced cooling for a spindle will add structure complexity and service difficulty, and is used when natural cooling cannot satisfy the cooling need. For high speed, high power spindles, natural cooling usually cannot provide adequate cooling to maintain stable thermal condition and lubrication condition. Since it is essential for spindle bearings to operate below a maximum temperature, effective cooling of bearings becomes necessary. The water cooling of the bearing outer rings is considered as a good method.

The effect of the water cooling of the spindle bearings was analyzed based on the thermal model established in Chapters 2 and 3 for Spindle B. Calculations for the model with water cooling in the bearing outer rings were done in contrast to the cases studied in Chapter 3. Figure 5.1 illustrates the temperature profiles after the water cooling was used in the bearings. These profiles can be compared with those

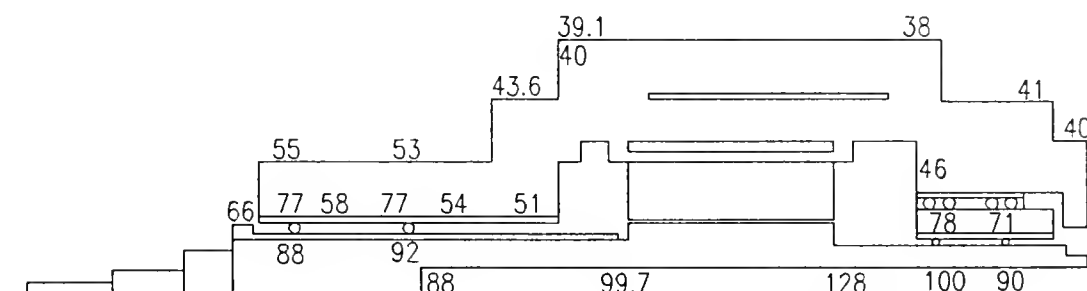
in Figure 3.10. The reduction of temperatures around bearings is obvious, particularly at high spindle speed. The water was introduced into the cavities near the bearing outer rings. Figure 5.2 shows the computed temperatures on the races of the bearings with and without the water cooling. Figure 5.3 shows the temperatures in the bearing outer rings. Figure 5.4 illustrates the temperatures at the spacer between the front bearings, the outer surface of the rear roller sleeve and the surface of the arbor center hole. Both the computational and measured results are displayed in Figures 5.3 and 5.4 (water cooling of the bearings and no water cooling of the bearings). The effect of cooling the bearing outer rings is a computational result only since the cooling was not introduced in the housing experimentally. The computations show that, for the same temperatures, with water cooling it may be possible to increase speed by about 10,000 rpm. The water cooling of the bearings was done by placing 8 quarter-inch diameter holes around the outer rings of the bearings. The convective coefficients for the water cooling of the bearings were $150 - 200 \text{ W}/^\circ\text{K}/\text{m}^2$ as listed in Table 3.9. These values are average values considering the total cooling area, water hole area and the convective coefficients at the surfaces of water holes. The water convection coefficients were obtained under the pressure of regular chilled water supply. Although the highest temperatures in Figure 5.1 are not much less than those in Figure 3.10, the high temperatures in the bearing rings and races are greatly reduced. This can also be observed from the temperature curves in Figures 5.2 through 5.4.



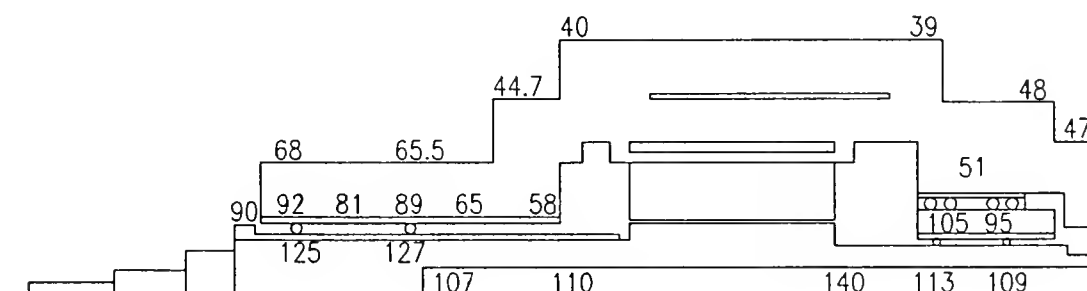
a. 15,000 rpm



b. 25,000 rpm



c. 35,000 rpm



d. 45,000 rpm

Figure 5.1 Temperature Fields (for Bearings with Water Cooling)
at 15,000, 25,000, 35,000 and 45,000 rpm

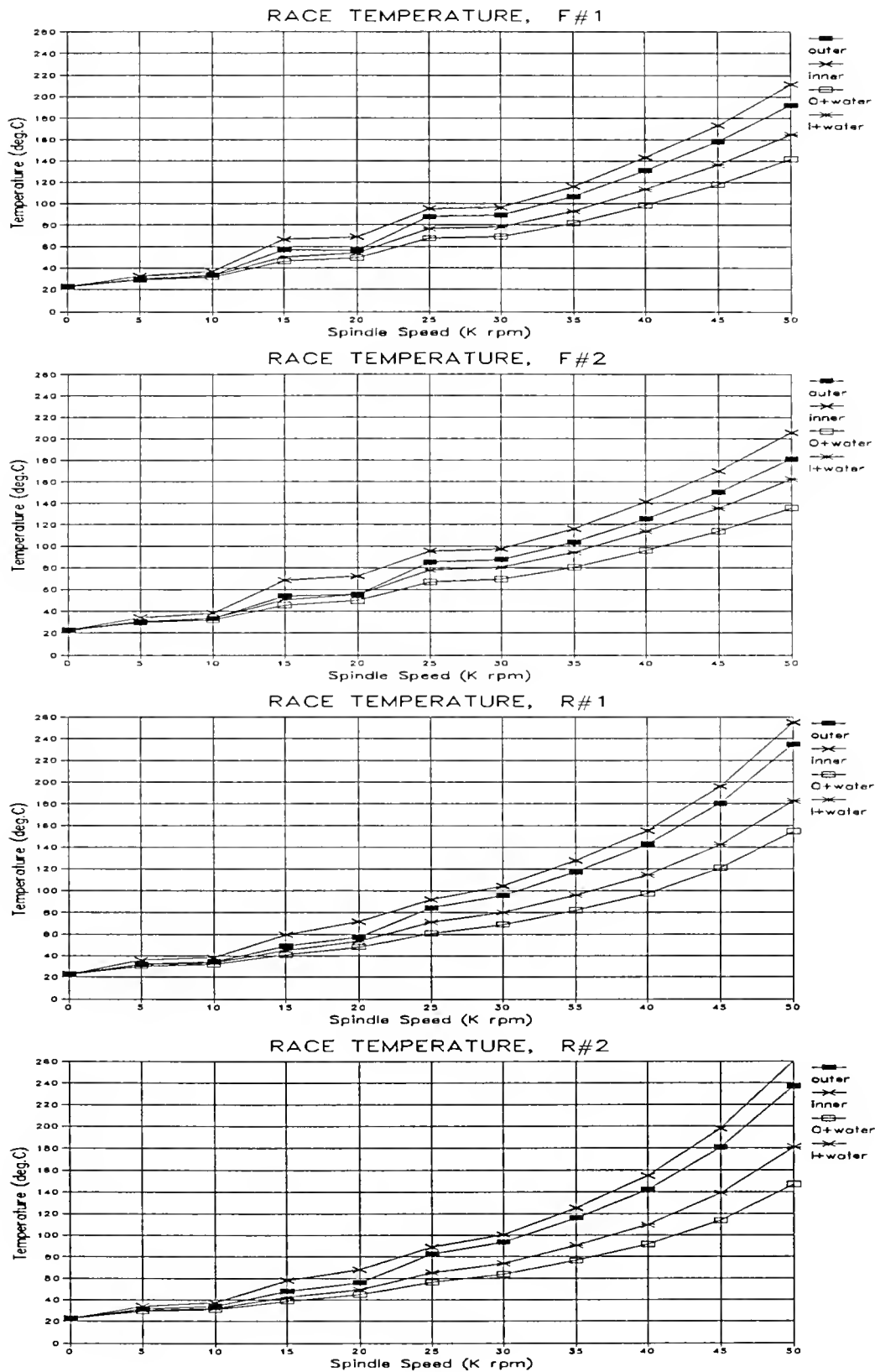


Figure 5.2 Temperatures in Bearing Races

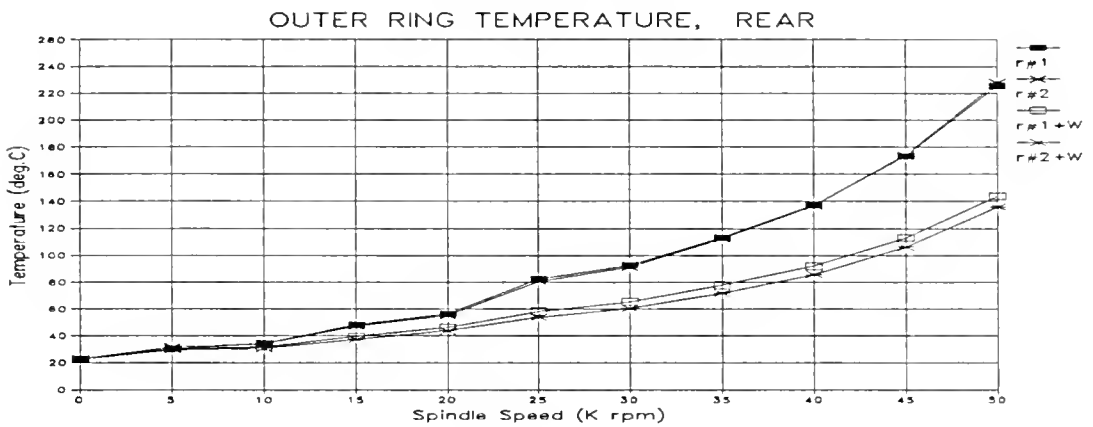
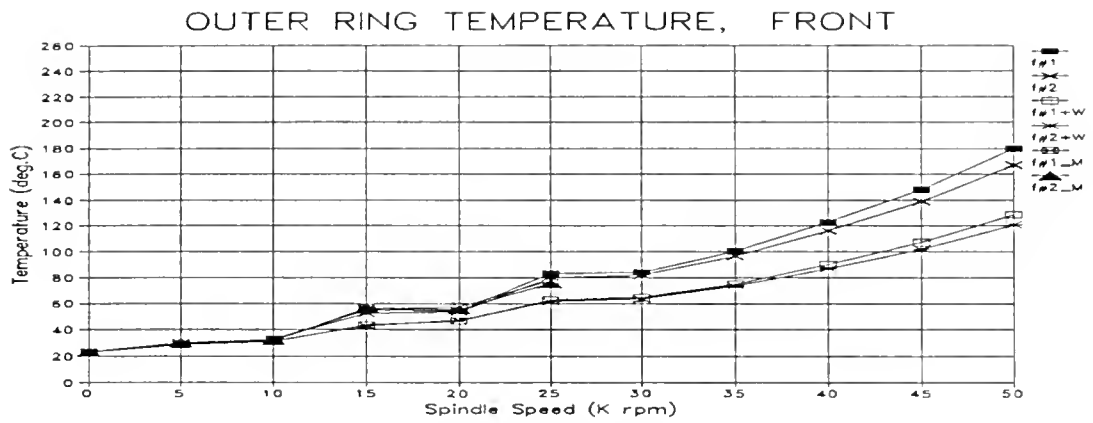


Figure 5.3 Temperatures in Bearing Outer Rings

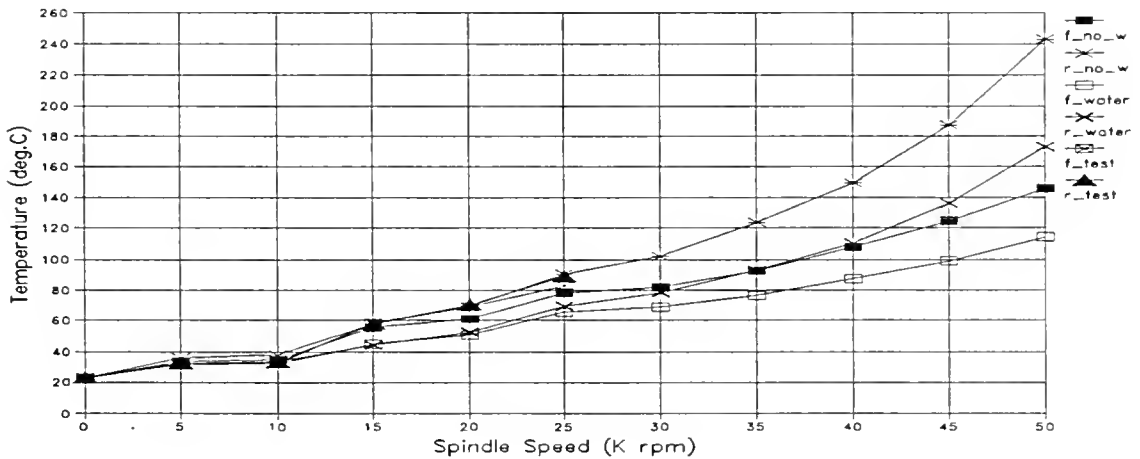


Figure 5.4 Temperatures at Spindle Arbor Inner Surface

Effect of Spindle Heat Source and Bearing Axial Load

Another method to reduce the spindle temperature is to reduce the bearing heat generation and to design the spindle structure such that the generated heat can be quickly conducted out of the heat sources and thus an even temperature distribution could be achieved. A uniform temperature field is always good for both eliminating thermal load and dissipating heat. But it usually cannot be easily achieved since the location of bearings will affect the spindle dynamic and static properties more than the spindle temperature distribution. As shown in the Figures 3.10, 4.5 and 5.1, the motor heat generation contributes much to the spindle temperature, especially to the temperature of the rear bearings. Therefore, it is reasonable to relocate the motor to a location away from the bearings such that the bearing temperatures can be reduced.

Figure 5.5 shows the measured effects of preload on the temperatures of the outer rings of the front bearings, and of the surface of the hole in the spindle. The preload was applied through a spring system that provides constant axial load to the bearings. The adjustment of the preload was made by compressing the springs a certain amount. The results are not very systematic, but they show that an increase of the preload from 100 lbs to 220 lbs (per two bearings) caused a temperature increase by about 10-15 °C. Figure 5.6 illustrates the calculated bearing heat generations when the bearing axial load varied from 110 lbs to 220 lbs. In this case, bearing heat generation was increased by 25% to 40%. This also indicates that an increase of bearing thermal load can strongly affect bearing friction.

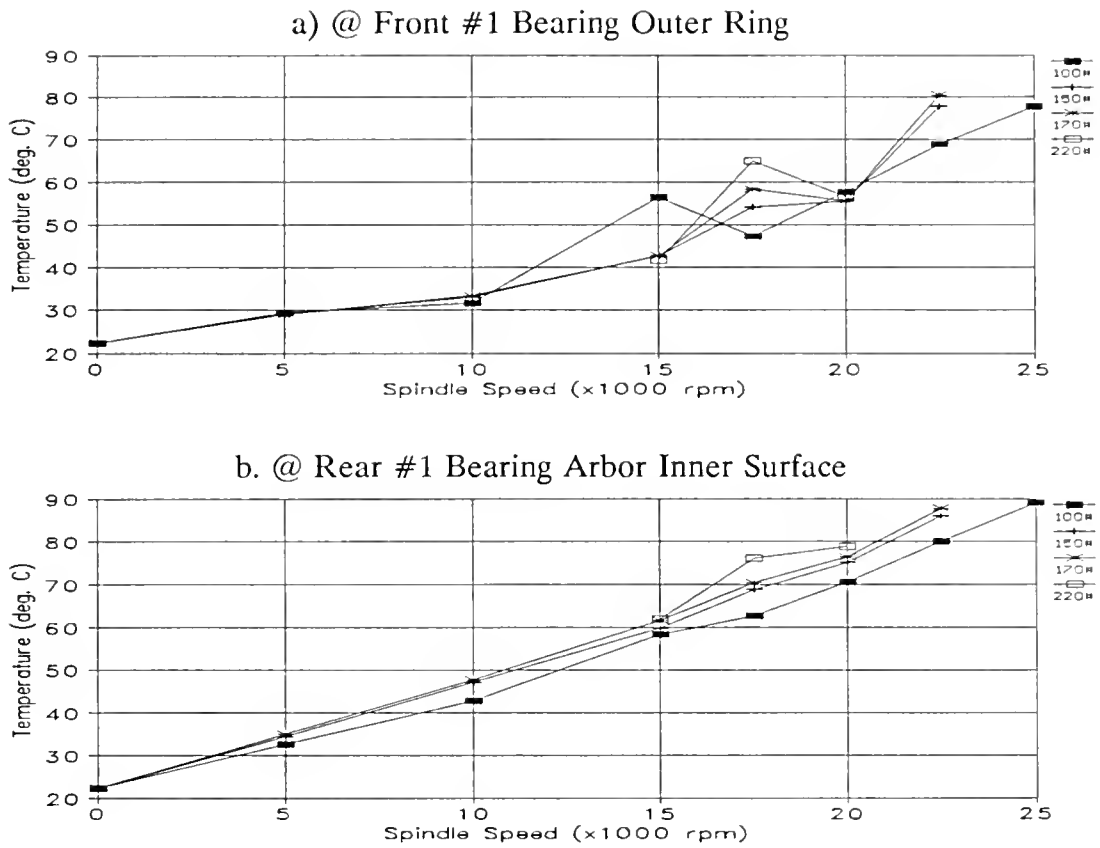


Figure 5.5 Measured Temperatures with Different Bearing Preloads

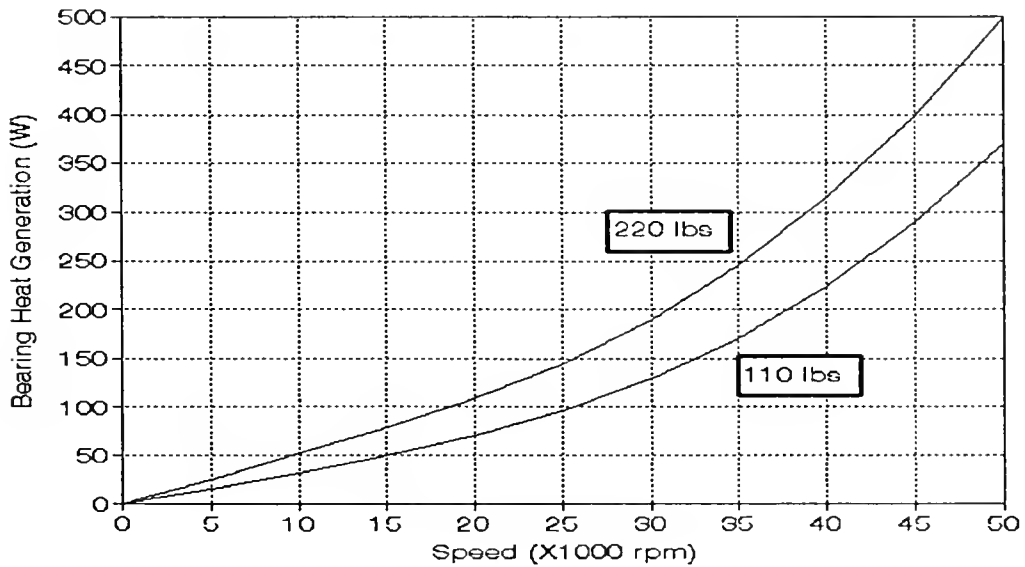


Figure 5.6 Bearing Heat Generation Calculation with Different Axial Load

Spindle Bearing Catastrophic Failure and Temperature

Usually it is relatively easier to detect bearing fatigue failure than to prevent bearing rapid catastrophic failure. It is especially true for high speed bearings. Two cases of bearing sudden seizure failure were experienced in this study, both at 16,000 rpm. Both failures happened when spindle was restricted axially and the bearing thermal load became large. Below is the investigation of one of the cases.

Bearing Failure Temperature (Measurement)

The bearing rapid failure happened 10 minutes after the spindle speed was changed from 8000 rpm to 16,000 rpm. The bearings measured a continuously increasing temperature, however, the bearing outer ring temperatures were below the assumed alarm level (80 °C). Figure 5.7 illustrates the transient temperature responses of bearing failure at the outer rings of the front bearings ("F_1" and "F_2" indicate the first and second front bearings). A spindle temperature profile was recorded once each minute for this case.

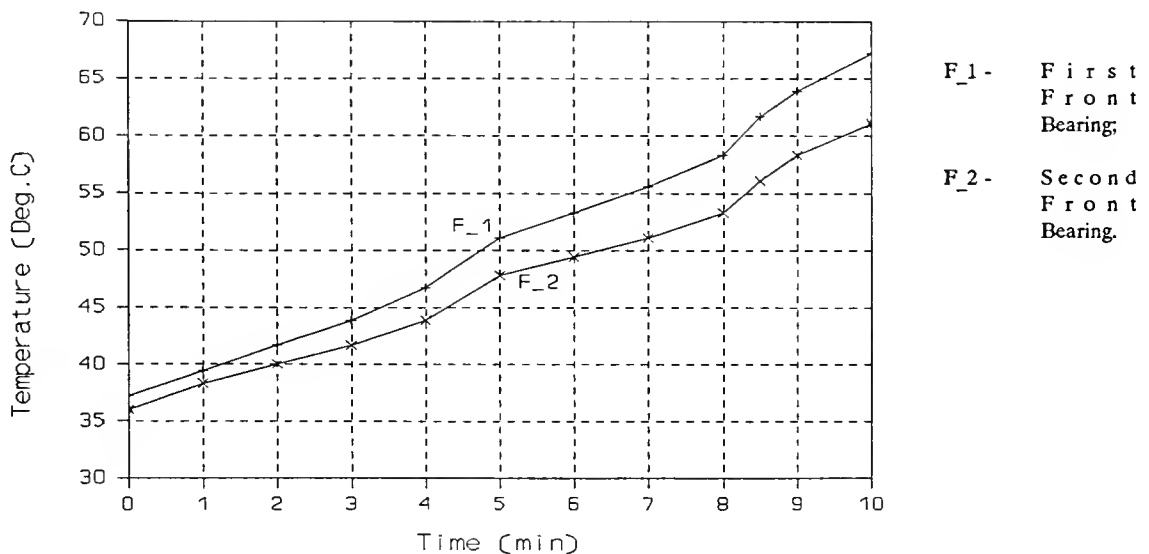


Figure 5.7 Measured Bearing Seizure Temperature

Thermal Induced Bearing Heat Generation

The above bearing failure was simulated through FEA. Since the spindle thermal model was well established, then in the simulation the variables were bearing heat generation and spindle running time. For this nonlinear case, a pseudo-nonlinear method was used. For each time period (1 minute) the bearing heat generation was held constant so as to use the available FEA software for the transient heat transfer calculation. The bearing heat generation was adjusted to make spindle temperature profile match measured profile at each period. Table 5.1 lists the increase of heat generation during the bearing seizure. The figure indicates that at the time of the seizure, the bearing heat generation was equivalent to that at 42,000 rpm, far beyond the maximum spindle speed. The estimated bearing heat generation is also plotted in Figure 5.8.

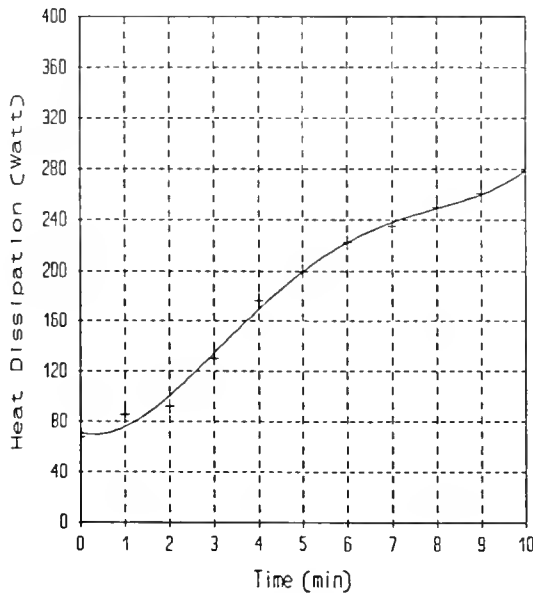


Figure 5.8a Bearing Heat Dissipation Change at Seizure

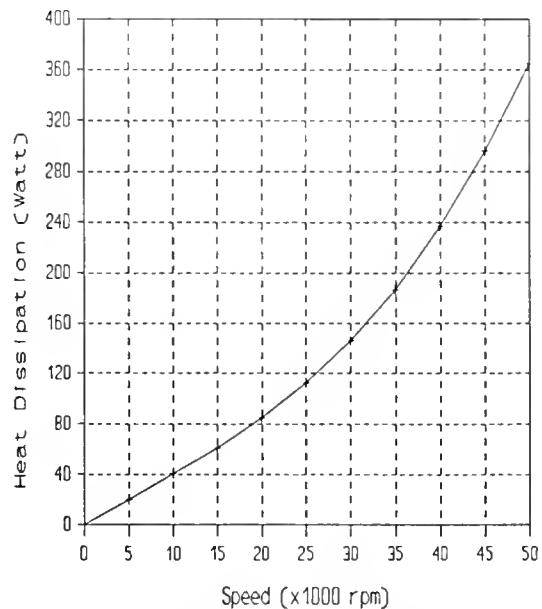


Figure 5.8b Bearing Heat Dissipation vs. Speed without Seizure

Figure 5.8 Bearing Heat Generation

Bearing Thermal Load at Failure

The axial loads were calculated through the relation between bearing heat generation and bearing axial load. The spindle has a constant axial load mechanism, thermal expansion can be compensated through a set of springs, and so the bearing thermal load can be eliminated. The spindle was set with an axial preload of 220 lbs (1040 N) per two bearings. The bearing seizure was because the movement of the bearings was constrained. It was assumed that at time 0 min., the spindle speed was changed from 8000 rpm to 16,000 rpm and the bearing axial load was 1040 N per pair, and then bearing axial load was calculated (Table 5.1 and Figure 5.9). The result shows that the axial load at bearing failure could have been four times as much as the preload.

Spindle and Bearing Failure Temperature

Since this bearing failure occurred in a short time, the spindle housing temperature increase was small, however, the bearing components had great temperature increases, and Figure 5.10 and 5.11 illustrate these changes. From the figures it can be seen that the highest temperature at the failure was about 105°C on the bearing inner race.

Bearing Rapid Failure Cause Analysis

The above investigated case is a typical bearing rapid failure. The steps for the failure were as follows: the bearing friction generated heat and caused the bearing components to expand. Since the bearing was axially constrained, the bearing was compressed by the thermal load. Under this thermal load, the bearing produced more heat, and so the bearing had larger thermal load. When the bearing

Table 5.1 Bearing Heat Dissipation at Seizure

Time	Front Bearing (Watt)		Rear Bearing (Watt)		Axial Load
(min)	per contact	per bearing	per contact	per bearing	(N)
< 0	3.5636	44.78	1.333	16.75	1040
0	5.4226	68.14	2.149	22.01	1040
1	6.8170	85.66	2.426	30.49	1325
2	7.3414	92.25	3.418	42.95	1440
3	10.374	130.4	3.958	49.74	2000
4	14.035	176.4	4.700	59.06	2500
5	15.906	199.9	5.014	63.01	2760
6	17.674	222.1	5.571	70.01	3020
7	18.713	235.2	5.898	74.12	3160
8	19.883	249.9	6.267	78.75	3620
9	20.747	260.7	6.540	82.18	3750
10	22.195	278.9	6.996	87.91	3950

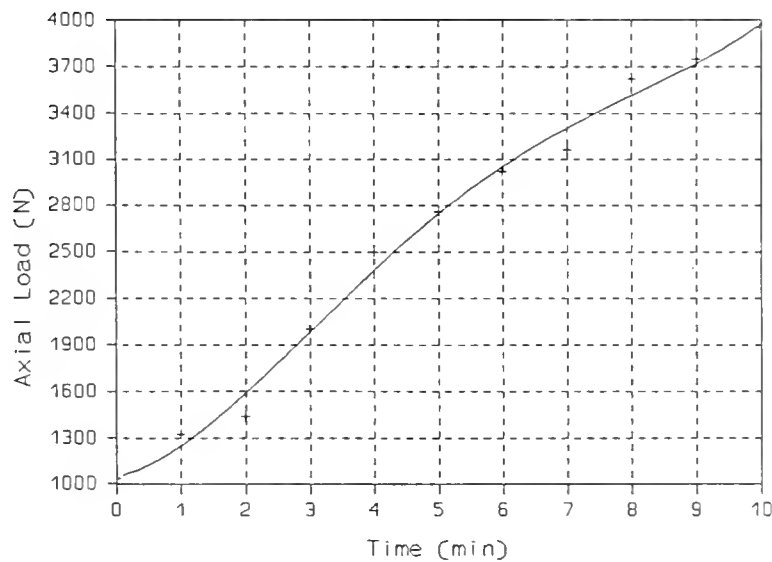


Figure 5.9 Increase of Bearing Axial Load at Seizure

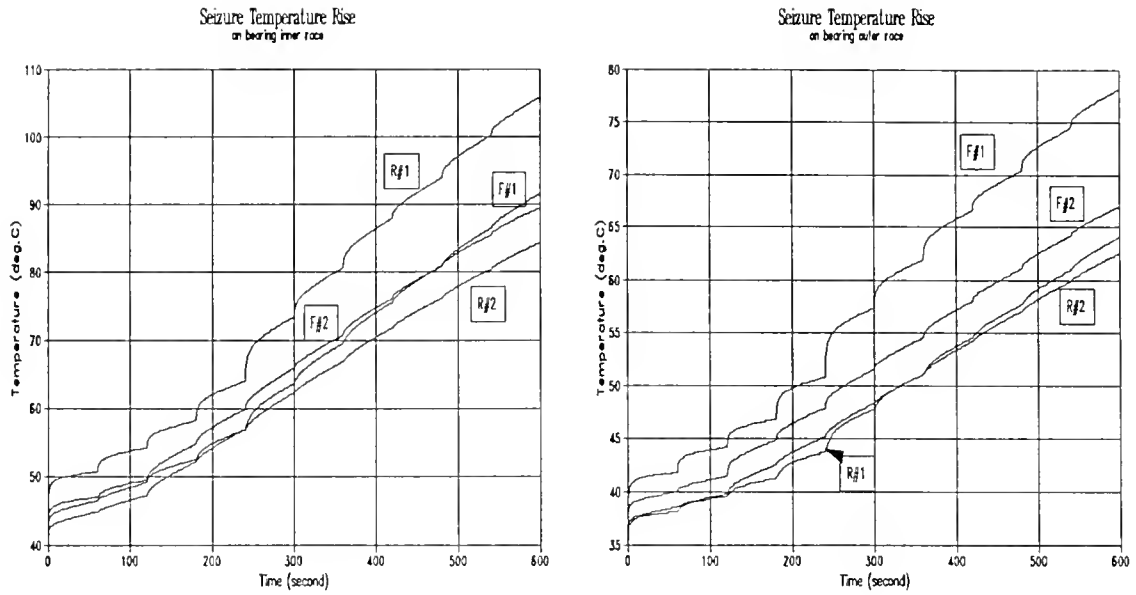


Figure 5.10 Bearing Temperature Change at Contact

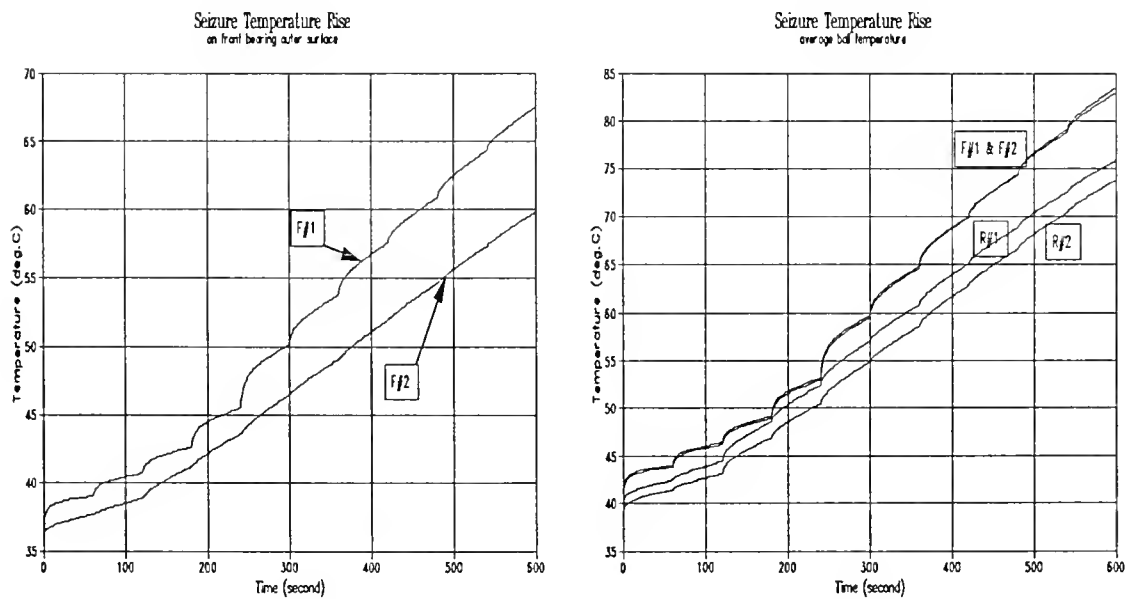


Figure 5.11 Bearing Temperature Change of Ring and Ball

load was too large, bearing ball-race lubrication film broke down, direct ball-race contact was resulted, and the friction force increased very rapidly. The large amount of heat deteriorated the lubricant around ball-race contact, and the remains of the

deteriorated lubricant caused more friction. The friction damaged the ball and race surfaces, and the increased friction finally stopped the bearing (spindle).

To prevent the seizure of bearings, it is very important to implement the bearing assembly with constant load system and to assure that it works all the time, so that the thermal load can be properly compensated. It is especially true for high speed bearings. It should be noted that after the bearing has seized, it is not always necessary to replace the bearing. The bearing may have only little damage, and be seized by the large bearing load and deteriorated lubricant. If the bearing thermal load can be carefully controlled and the bearing is run with the speed increased slowly, the remainder of the deteriorated lubricant can be removed by new lubricant and the bearing can recover. When the bearing ball is large, the maximum Hertz stress at the ball-race contact is small, and bearing damage will be light. In the above analyzed seizure case, the front bearing ball diameter was 10.31875 mm, and the bearing recovered without open-spindle service. The spindle has operated for 7 additional months so far. If the bearing ball is small, the local contact stress is large, and the bearing damage may be substantial. In another seizure case with the same spindle but a different bearing (front bearing ball diameter 7.14375 mm), the bearings were significantly damaged and had to be replaced.

The simulation of seizure shows that 100 °C is the limit of this bearing running temperature. If bearing temperature can be reduced somehow, the bearing's thermal load can be reduced, and the bearing service life can be improved.

CHAPTER 6

SPINDLE BEARING THERMAL PREDICTION MODEL AND BEARING CONDITION DIAGNOSIS

Bearing Defect Frequencies and Detection

The conventional diagnosing methods of bearing defects involve analyzing bearing noise and temperature. Since the 1970s, spectral analysis of bearing vibration has become a major tool to diagnose bearing conditions. Some description of this technique is provided by Philips [33], Sandy [34], and Berry [35]. This technique is based on the analysis of the bearing noise frequencies. If bearing's components have defects, there will be an impact when a defect passes a ball-race contact. When bearing inner ring is rotating and outer ring is fixed, the frequencies of the impacts will be

$$BPFI = \frac{n_b}{2} \left[1 + \frac{d_b}{t} \cos(\alpha) \right] \times \frac{n}{60} \quad (\text{Hz}) \quad (6.1)$$

$$BPFO = \frac{n_b}{2} \left[1 - \frac{d_b}{t} \cos(\alpha) \right] \times \frac{n}{60} \quad (\text{Hz}) \quad (6.2)$$

$$BSF = \frac{t}{2 d_b} \left[1 - \left(\frac{d_b}{t} \cos(\alpha) \right)^2 \right] \times \frac{n}{60} \quad (\text{Hz}) \quad (6.3)$$

$$FTF = \frac{1}{2} \left[1 - \frac{d_b}{t} \cos(\alpha) \right] \times \frac{n}{60} \quad (\text{Hz}) \quad (6.4)$$

where d_b , t , α , n and n_b are as defined in Chapter 2. $BPFI$ is the frequency at which

ball (or roller) passes any contact point on bearing inner raceway, *BPFO* is the ball (or roller) passing outer race frequency, *BSF* is ball (or roller) spinning frequency, that is the frequency at which ball (or roller) makes a full rotation about its axis, *FTF* is bearing cage rotation frequency (or fundamental train frequency). If strong signals at any of above frequencies (or their harmonics) are present, the bearing is suspected to have flaws on the corresponding components. Progressive increase of the signal's spectral power at any of the above frequencies will further confirm the existence of the defect. Philips [33], Sandy [34], and Berry [35] discussed many characteristics of bearing defects signal spectrum and methods to determine the location of bearing defect and to estimate the remaining bearing life.

The bearing signature analysis technique also has some shortcomings. First, since the measured spectrum includes signals from all vibration sources, and the signal frequencies may be close to each other, the bearing vibration signal may not be as significant as noises. It can be difficult to distinguish the bearing vibration from other noises. Secondly, though this technique can indicate the bearing defect situation and even predict the remaining life, it usually cannot identify the existence of severe bearing load or failure lubrication before the bearing is damaged. When a bearing is under extraordinarily high load, or lacks lubrication, it is difficult to recognize the impending catastrophe in the spectrum. In high speed bearing applications the above mentioned situations are usually the major causes of bearing failures. Sound and vibration signals from high speed spindles were measured in this study, but the results showed that the direct use of the signal spectrum is difficult due to the very strong background noise. Figure 6.1 illustrates a spectrum of bearing

vibration (acceleration). There should be frequency peaks at about 593, 1186, 1335 or 1745 Hz if there are defects on cage, ball, outer race and inner race of this bearing, respectively. But the spectrum shows that with the background noise only characteristic frequencies of badly damaged bearing could be seen in the spectrum. Clearly by the time the characteristic frequencies would be apparent, it would be too late for defect detecting and failure prevention.

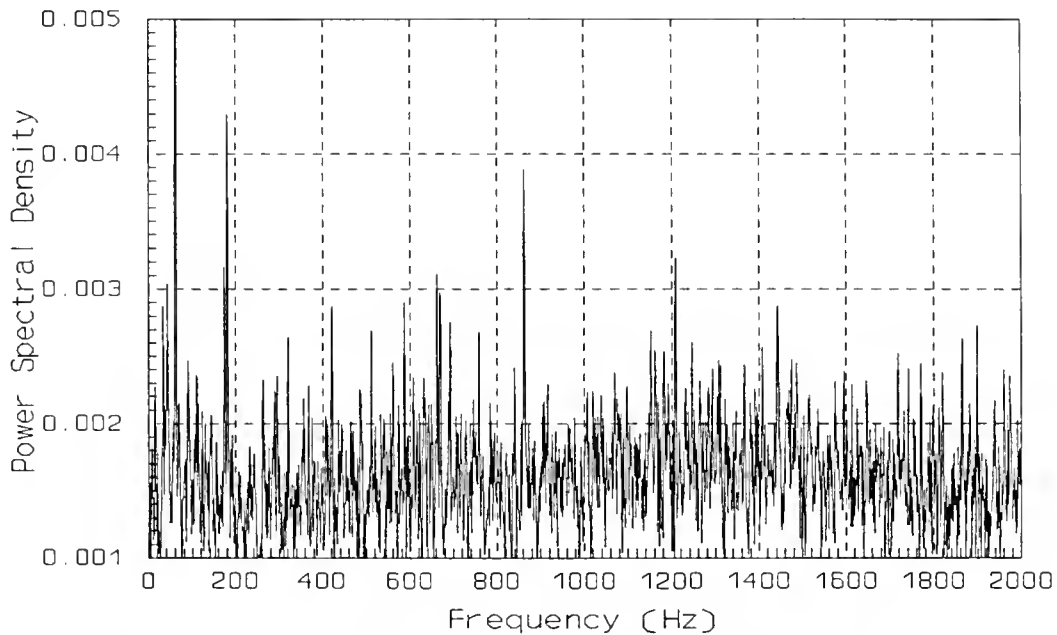


Figure 6.1 Spectrum of Bearing Vibration Signal @ 10,000 rpm

Using Thermal Model for Bearing Monitoring

Bearing monitoring is the continuous diagnosis of the bearing condition. Spindle thermal models can serve as a useful tool for off-line bearing condition monitoring. The thermal model can be a spindle FE thermal model or state-space model as discussed by Stein and Tu [30]. In monitoring, the model load parameters will be varied to make calculated temperatures match measured temperatures. The obtained load parameters (bearing heat generation and bearing load) will indicate

bearing conditions. For steady state bearing condition monitoring, an established FE thermal model can be used to obtain the bearing heat generations corresponding to measured temperatures. For transient analysis, such as bearing rapid failure mode, load parameters become nonlinear and the calculation of the thermal model should use small time steps. The seizure analysis in the last chapter is an example of this technique.

Outer Ring Temperature Variation Technique

A one dimensional lumped-heat-capacity system can be used to illustrate the bearing temperature response, since bearing heat generation can be considered as uniform in the race contact circle, and heat conduction is basically radial in direction. Then bearing temperature differential equation can be written as

$$P - Ah(T - T_r) = Mc \frac{\partial T}{\partial t} \quad (6.5)$$

where P is the change in bearing heat generation rate, h is a properly chosen convection coefficient which represents heat dissipation from the bearing, M is bearing mass, including mass of bearing rings and balls, A is the total convective area, c is bearing specific heat capacity, T_r is the bearing temperature before P is applied, and τ is so defined as $\tau = Mc/Ah$ and is the time constant. The bearing retainer is not considered here because it has a very small mass and heat capacity. The solution of equation 6.5 is

$$T = \frac{P}{Ah} (1 - e^{-\frac{t}{\tau}}) + T_r \quad (6.6)$$

and the first derivative of T with respect to time t is

$$\frac{dT}{dt} = \frac{P}{Mc} e^{-\frac{t}{\tau}} \quad (6.7)$$

For any bearing heat generation change, the bearing temperature change and the change rate can be determined if the bearing geometrical and environmental conditions remain unchanged. This provides a way to monitor the bearing condition. If the bearing temperature change rate is greater than a certain value, P/Mc , the bearing can be said to be under a poor operational or physical condition, and maintenance should be undertaken in order to avoid a sudden bearing failure. For the bearing investigated here, $P/Mc = 0.7 \text{ } ^\circ\text{C}/\text{min}$, bearing mass $M = 0.45 \text{ kg}$, bearing heat capacity $c = 0.48 \text{ KJ}/\text{kg}^\circ\text{C}$, and at 25,000 rpm, the bearing heat generation P was about 150 W . Also the time constant of this bearing was about five minutes (for $h = 50 \text{ W}/\text{m}^2^\circ\text{C}$).

Monitoring the bearing through the bearing temperature has been available in industry for many years, however, the monitoring parameter is always the bearing temperature since temperature change rate is difficult to obtain and the boundary to distinguish normal and bad condition varies from machine to machine. In low speed bearing applications, the bearing failure is usually a long process and abnormal bearing temperature can be measured to decide the bearing condition. At high speed, bearing rapid failure becomes very important and the measured failure temperature may not be very high. A strategy to prevent this bearing rapid failure is to set the bearing maximum temperature sufficiently low. However, a low limit temperature also limits the bearing and machine abilities. Bearing ball and ring material properties are almost constant for temperatures below 300°C . A phenolic

ball retainer has a maximum operating temperature of about 135°C [41, p. 67], and the limit of the thermal stability is 150°C for commercial mineral oil and 200°C for synthetic oil [32, p.223]. In other words, regular high speed spindle bearings (light duty, angular contact ball bearings) have the potential to operate at temperatures up to 100°C . If a maximum temperature is set at 60°C as is commonly done, the high speed capacity of a bearing will not be fully utilized.

If temperature change rate is used to monitor bearing condition, the bearing working temperature can be higher, that is, the bearing can be used at higher speed. If a severe bearing load is present, it can be detected through a temperature change before the bearing temperature reaches a high level. Since the measured temperature response on a bearing outer ring is rapid, the machine can be stopped before the bearing can be damaged.

Measured Temperature Response and Analysis:

In the process of spindle temperature field measurement, transient responses of bearing outer ring temperature have been measured for different spindle speeds, bearing preloads and bearing location. Some typical bearing outer ring temperature responses are illustrated in Figure 6.2. In order to get the nature of the temperature response, each response has been normalized and curve-fitted exponentially and linearly. Curve fitted transient responses in Figure 6.2 are displayed in Figure 6.3. In this investigation, exponential and linear curve fittings were conducted to 60 transient temperature responses of different speeds, bearing locations and bearing axial loads. The linear fitting results showed that a temperature increase rate higher than $1.3^{\circ}\text{C}/\text{min}$ results in seizure. A similar conclusion could not be drawn from

exponential fitting results. Table 6.1 (bearing failure cases) and 6.2 (bearing normal condition cases) list some results.

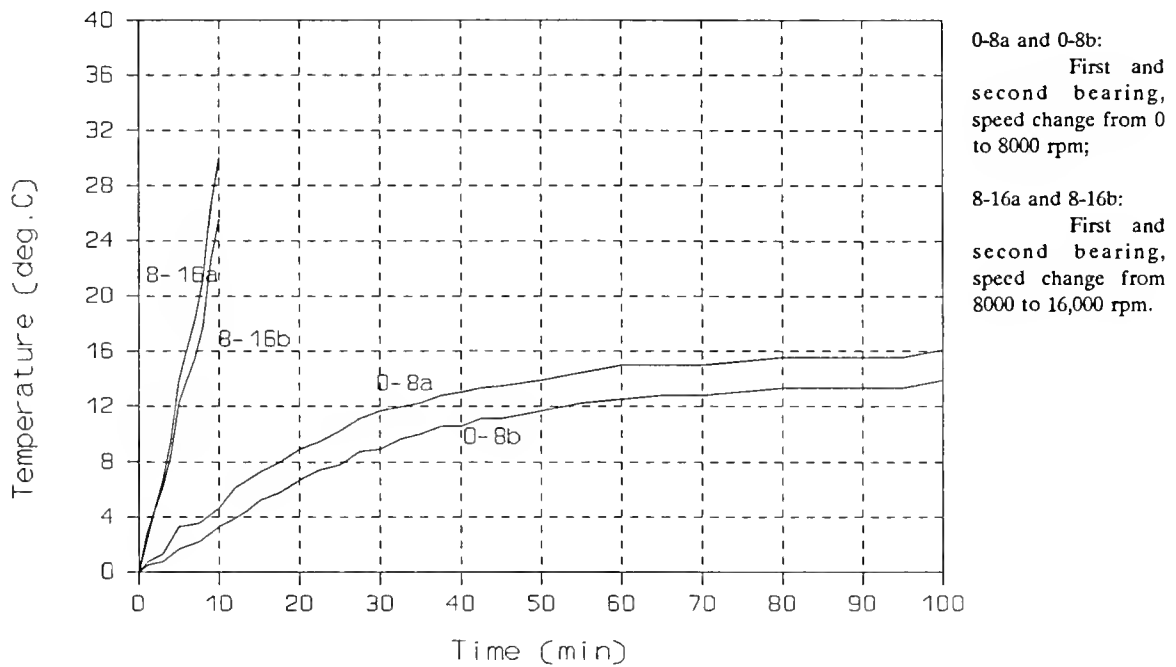


Figure 6.2 Measured Temperature (Normal & Failure Cases)

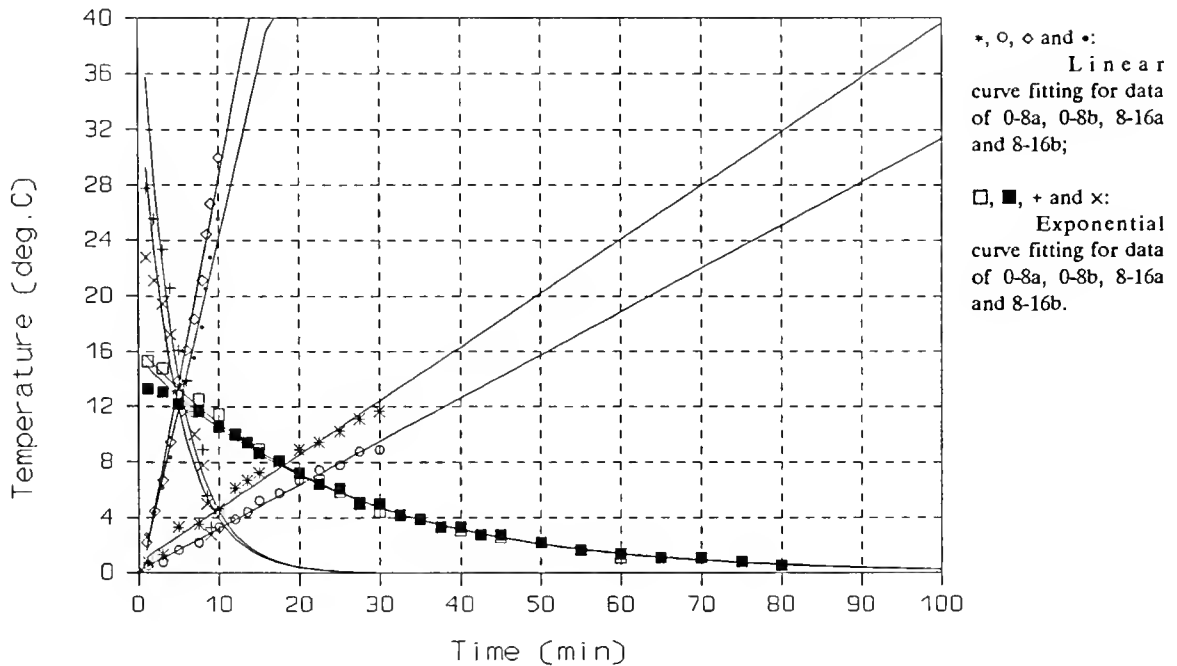


Figure 6.3 Curve Fitting Results for Cases in Figure 6.2

Table 6.1 Curve Fitting Results of Bearing Failure Cases

CASE	linear, $T=a+bt$		exponential, $T=ce^{dt}$	
	a	b	c	d
0-16a ¹	0.465	1.5700	38.090	-0.1274
0-16b ¹	-0.828	1.3300	32.820	-0.1071
8-16a ²	-1.390	2.9925	45.070	-0.2239
8-16b ²	-0.613	2.4781	36.600	-0.2313

- ¹: 0-16a & 0-16b: axial load 200 lbs, speed increase from 0 to 16,000 rpm, bearing 3MMV9912CR with 25° nominal contact angle, 9/32" ball diameter, 26 balls, two different bearings;
- ²: 8-16a & 8-16b: axial load 170 lbs, speed increase from 8000 to 16,000 rpm, bearing RHP B7012 with 20° nominal contact angle, 13/32" ball diameter and 18 balls, two different bearings;

Table 6.2 Curve Fitting of Normal Cases

CASE	linear, $T=a+bt$		exponential, $T=ce^{dt}$	
	a	b	c	d
15-17a ¹	1.2626	0.7071	27.680	-0.0707
15-17b ¹	3.6864	0.8333	32.530	-0.0754
0-5a ²	-0.0161	0.2170	10.140	-0.0397
0-5b ³	-0.1210	0.3048	10.340	-0.0407
10-15a	0.2420	0.5980	33.540	-0.0503
10-15b	-0.3580	0.4918	35.250	-0.0490
20-25a	1.8400	0.6376	7.260	-0.1470
20-25b	0.7170	0.8192	9.897	-0.1670

- ¹: speed change from 15,000 to 17,000 rpm, bearing axial load 220 lbs, all rest bearing axial load 100 lbs;
- ²: speed change from 0 to 5000 rpm. Speeds for other cases can be similarly found from case names;
- ³: all bearings are RHP B7012 with 20° nominal contact angle, 13/32" ball diameter and 18 balls;

It seems that the linear temperature increase rate is a good measure of bearing heat generation. A threshold (maximum rate) can be determined from bearing parameters, that is, P/Mc . It has been shown that the measured failure rate (1.3 °C/min) is about twice of the calculated value (0.7 °C/min), so 1.0 °C/min could be taken as a threshold. Monitoring of bearings can be made by comparing the measured temperature rates with the threshold. Since high speed bearing failure is a rapid process, bearings should be continuously monitored during their running.

Bearing Monitoring through Measuring Acoustic Emission and Signal Demodulation

Bearing Acoustic Emission

Acoustic emission, or AE, as defined in ANSI/ASTM E610-77 [42, p. iii], "is the class of phenomena whereby transient elastic waves are generated by the rapid release of energy from a localized source or sources within a material, or the transient elastic wave(s) so generated." These elastic waves are considered as generated from material's microstructure under stress. The intensity of the waves is related to the magnitude of stress.

Ball-race contacts of a bearing have substantial stresses, then they also generate AE signals. When the bearing components have flaws or other defects, the ball will impact on race when it passes the defect zones. The impact represents a high local stress and, subsequently, high AE. So it is possible to monitor the bearing working conditions through its AE signals. Since AEs are very high frequency signals

(20 - 1000 kHz), where other vibration signals are weak, it becomes easier to analyze the bearing defect.

AE Measurement and Signal Processing

Piezoelectric element sensors are often used to measure the AE signal due to their high sensitivity and low cost. Because of the wide frequency range of the AE signal, AE sensors are naturally resonant but the various modes of vibration of the element are extensively cross-coupled, thus they do not have a simple frequency response curve but one which consists of a dominant and many other peaks [42]. During selection of AE sensors, sensitivity, frequency response and size are important parameters.

Since AE signal lies in the high frequency, analysis of this signal in frequency domain is difficult, and is also not necessary. What is interested in the bearing defect monitoring is the signal intensity at defect frequencies. When the bearing is rotating, AE impulses are generated in groups at certain frequency. For example, every time a ball rolls over a defect spot on the bearing outer raceway, a group of AE impulses are generated and propagated. The characteristics of the AE impulses are not important in the bearing monitoring, since the envelope of the AE impulses can reflect the intensity of the bearing defect signals. In order to extract the signals with the bearing defect frequencies (the "envelope"), a simple technique to demodulate the AE signal was developed. Figure 6.4a displays the possible ball-race contact AE signal with little background noises. The envelope of the AE signal is the defect signal at one of the bearing characteristic frequencies. The demodulation technique

is to rectify the signal first to generate a corresponding low frequency, and then use a low pass (LP) filter to obtain the signal at the defect frequency (Figure 6.4b and c). A wide-band, high precision rectifier and wide-band HP and LP filters were implemented and used. The above process will be still valid if there are several defect frequencies. This signal processing is illustrated in Figure 6.4d, where the high pass (HP) filter is used to get rid of the background noises but keep high frequency AE signal.

Figure 6.5 shows the spectrum of a measured bearing vibration signal, Figure 6.6 shows the spectrum of the signal after the processing. It can be seen that several bearing "defect frequencies" become visible in the second spectrum. Since the ball-race rolling contact generates AE signal as well, the existence of bearing defect frequencies does not mean the occurrence of the bearing defects. The existence of the defects of bearing components can be determined if the magnitudes of the peaks at bearing defect frequencies grows progressively. A threshold should be determined based on the same bearing assembly and new bearing under proper operation conditions. Berry [35] and Berggren [43] discussed the determination of bearing defect in the spectrum of bearing vibration, and their conclusions can also be used in AE spectrum.

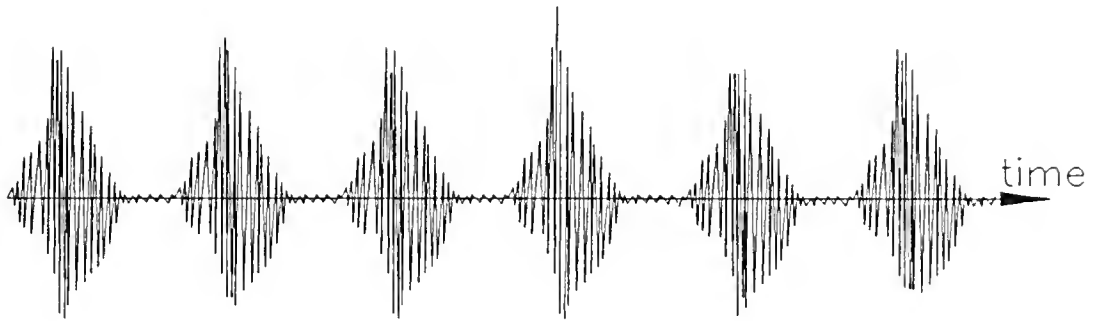


Figure 6.4a Pattern of AE Signal from Bearing

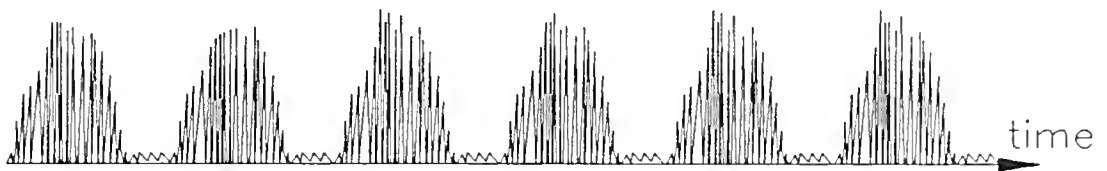


Figure 6.4b AE Signal after Rectification

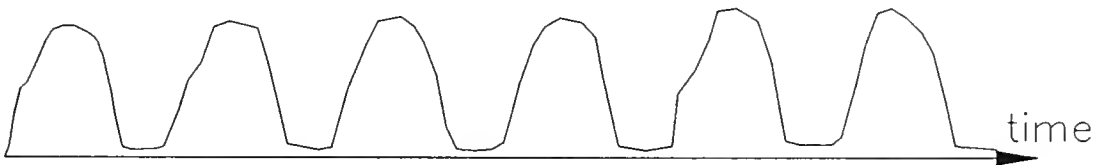


Figure 6.4c Rectified AE Signal after Low Pass Filter

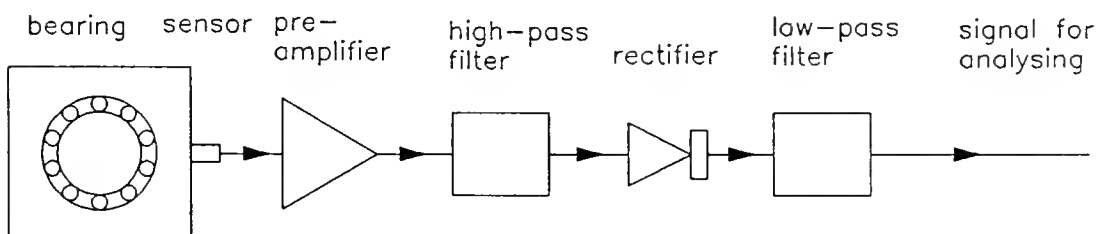


Figure 6.4d AE Signal Processing Diagram

Figure 6.4 AE Signal and Signal Processing

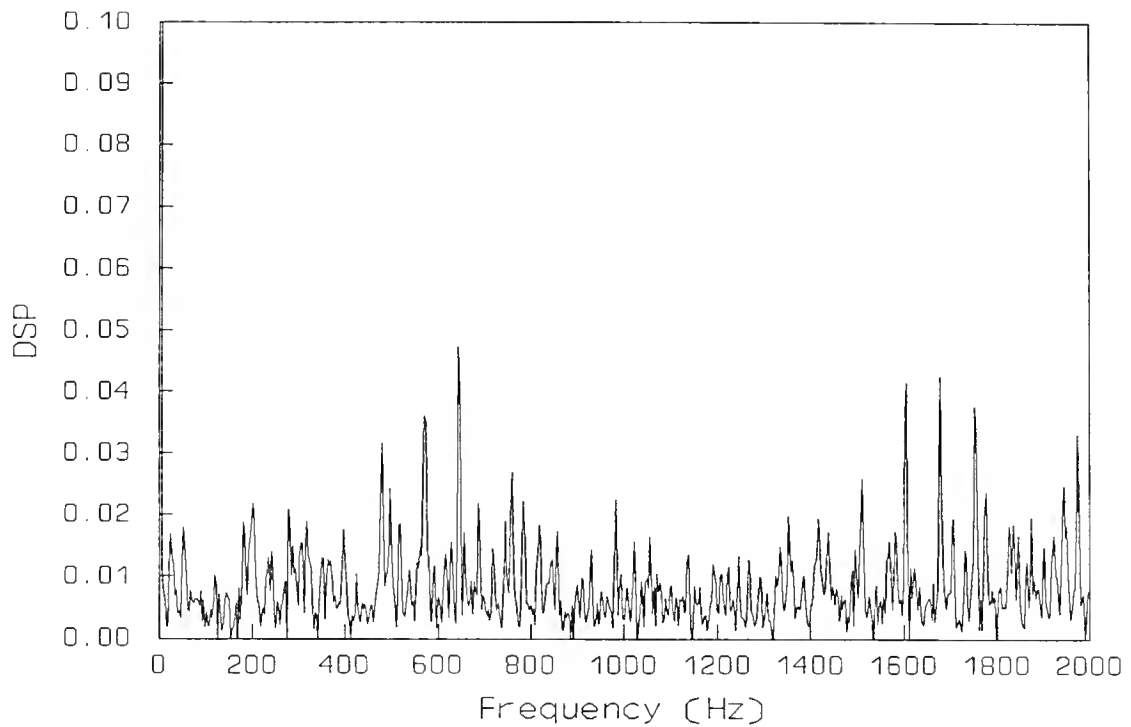


Figure 6.5 Bearing Vibration Signal @ 10,000 rpm

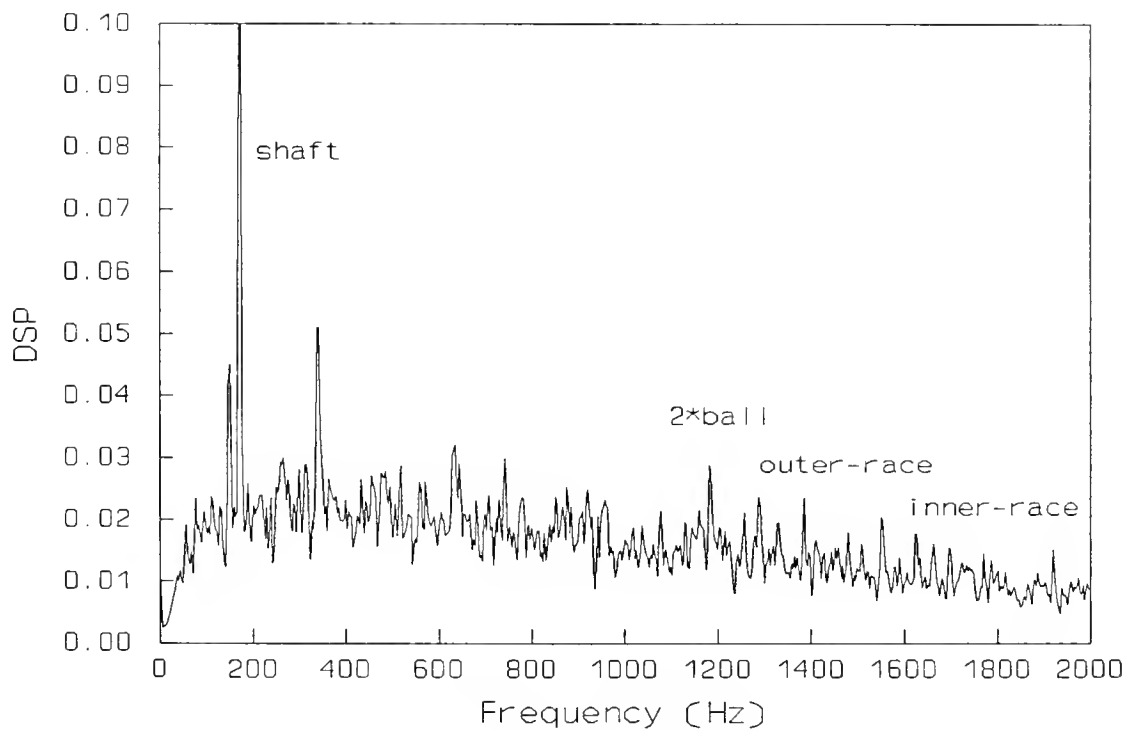


Figure 6.6 Signal of Figure 6.5 after Processing

Remarks

Since AE signals have high frequencies, they have very short wavelengths, and it is important to provide a good passage for AE signals to propagate from their source to the sensor. The interfacing surface between the sensor and the object should be smooth, the sensor should be mounted to the object firmly. Any gap between the AE source and sensor should be filled by good AE conductive cement. AE signals are also very weak. In order to avoid attenuation and interference, cabling should be as short as possible, a pre-amplifier should be placed as close to the sensor as possible, and the sensor should be installed very near to the AE source.

The strong peak at spindle rotation frequency in Figure 6.6 can prove that the signal processing was effective. This signal is not significant compared to the noises in Figure 6.5, but when it was demodulated from high frequency, it became the strongest signal. This signal was generated by the small imbalance of the spindle rotational components (the tool in the spindle was a single flute end mill). This signal was small both in low frequency range and in high AE frequency range, but since other high frequency signals were even smaller, it appeared very strong. A small AE signal at inner-race or outer-race defect frequency indicates a good bearing, while these peaks are invisible in Figure 6.5. In order to diagnose bearing defect, it is important to have a record of the AE signal spectrum of a good bearing in the same condition to compare with other measured signal.

The cut-off frequencies of HP and LP filters can be chosen based on the background noise frequency range and the bearing defect frequency range. The cut-

off frequency of the HP filter should be higher than the highest frequency of the significant noise, and the cut-off frequency of the LP filter should be higher than the highest bearing defect frequency. For the above case in Figure 6.5 and 6.6, the bearing speed was 10,000 rpm, the fundamental defect frequencies were below 2000 Hz, and the major background noise frequencies were between zero and 10 kHz. The cut-off frequency of the HP filter was 15 kHz and that of the LP filter was 3000 Hz.

Since acoustic emission depends on the strain-stress condition of the ball-race contact, and when bearing load and lubrication situation is different, this condition will be also different, the AE can be used to predict bearing condition.

CHAPTER 7 CONCLUSION AND FURTHER WORK

Conclusions

The FE thermal model developed in this study provides a useful tool in the analysis and design of high speed spindles. This model can yield a good estimate of the spindle temperatures, particularly for the locations not accessible for measurement, such as the contacts between the ball and races of the spindle bearings, and the spindle shaft center. The measurements, through the thermocouples and the infrared sensor, gave the actual temperatures at some accessible points in several different conditions, and were used to verify in the model.

The modeling technique is effective and efficient. The accuracy of the model depends on many factors, such as bearing heat generation, material properties, surface convection coefficients, motor heat generation, geometrical simplification, mesh size and the FEA method used. This study investigated these factors. The results are of great value for reference to the modeling of other spindles. Making a 2-D model from the 3-D structure is very important for the simplification and the generality of the model. Since high speed spindles have many structural similarities, it will be much easier to generate other models through the procedures in this study than to generate a new 3-D finite element model.

The improved formulae of the bearing heat generation were proved to be more accurate than Palmgren's original empirical model for high speed angular

contact ball bearings. The verified bearing heat generations and motor losses can provide a good reference for spindle design.

The method to include the local thermal resistances (interfaces and cavities) into material properties proved satisfactory. The conductive and convective coefficients obtained are useful for modeling of other high speed spindles in the cases when no other reliable data are available. An important observation is that, for Spindle A, the convective coefficients were dependent on the spindle speed, while for Spindle B, the coefficients did not show a significant change for the speed ranges studied. It can be understood that the influence of speed on convection increases with the speed and then remains constant at high speed. When the spindle speed is beyond a certain limit, the air flow speed at most surfaces will not increase significantly with spindle speed. Therefore, convection will no longer depend on spindle speed.

The analysis also shows that the air pressure for the air-oil lubricator affects the temperature through internal convection. Since the fast-moving air inside the spindle has a much higher ability to convey heat from hot surfaces to cold surfaces than does still or slow-moving air, the air inside the fast spindle has several times higher "conduction" capability.

Both calculation and measurement show that the spindle internal motor generates most of the spindle heat and greatly affects the temperatures of the bearings. In new spindle designs, the selection of a low loss motor should be considered.

The FE model evaluation shows that water cooling of the bearing outer rings can effectively reduce the overall bearing temperature. If the bearing temperature limits the maximum spindle speed, for the same temperature, water cooling of the bearing outer rings is possible to increase the spindle speed by about 10,000 rpm.

The bearing seizure analysis gives a transient view of a catastrophic bearing failure, and suggests another use of this spindle thermal model. By measuring the spindle temperatures, one can use this model to estimate the bearing thermal load and to predict the bearing condition.

It is also shown that the bearing temperatures, as well as the temperature change rate, can identify the bearing's condition, and that the bearing's acoustic emission can be used as a very effective tool to detect bearing defects, especially when strong background noise is present.

A computer program was developed for the calculation of the speeds and loads of the bearing components at various speeds.

Areas of Further Research

Based on the model established, further analysis should be made on the spindle's thermal deformation, the induced bearing load, and the effect on the spindle's properties and machining accuracy. The spindle housing and arbor axial expansions can be calculated by using the FEA. For spindles with bearings in fixed positions, the bearing axial load can be obtained from the housing and arbor expansions and from the bearing axial stiffness.

A product should be developed to predict the spindle bearing condition through the bearing AE signal intensity. The method to obtain the AE signal reliably

and to process it effectively should be further investigated. For example, how does the gap between the bearing outer ring and the housing affect the transmission of the AE signal, and how do the filter cut-off frequencies affect the AE signal and noise. Development of a micro-controller-based technique can realize the signal processing and on-line monitoring of the bearing.

The thermal model can be improved by establishing empirical formulae to estimate convective coefficients for various models and working conditions, such as a horizontal spindle, or a limited working space. In order to apply this thermal modeling technique to other bearing assemblies, other bearing heat generation models for different types of bearings and lubrications should be studied.

Forced bearing cooling should be studied further in order to understand the potential of this method to increase the bearing's operating speed and the effect on the bearing's service life. Other cooling methods, which include the method to reduce the effect of the motor heat generation on the bearings, should also be studied to provide alternatives for spindle design. The design rules of the cooling system for water cooling or other cooling methods should also be investigated.

Since the motor heat generation has a great influence on the temperatures of the bearings and the spindle, ways to eliminate this influence can be studied. Research can be done to improve the motor design so as to reduce the motor (particularly the rotor) heat generation, and to improve the spindle structure design so as to prevent motor heat from flowing to the bearings.

APPENDIX A BEARING CALCULATION PROGRAM

Introduction

BEARING is a bearing load and speed calculation program written in C. The calculation procedure is illustrated in Figure A.1. In the flowchart the upper case procedures are sub-programs. Calculation conditions are determined by input parameters. The equations used in this program are adopted from [5] and [41].

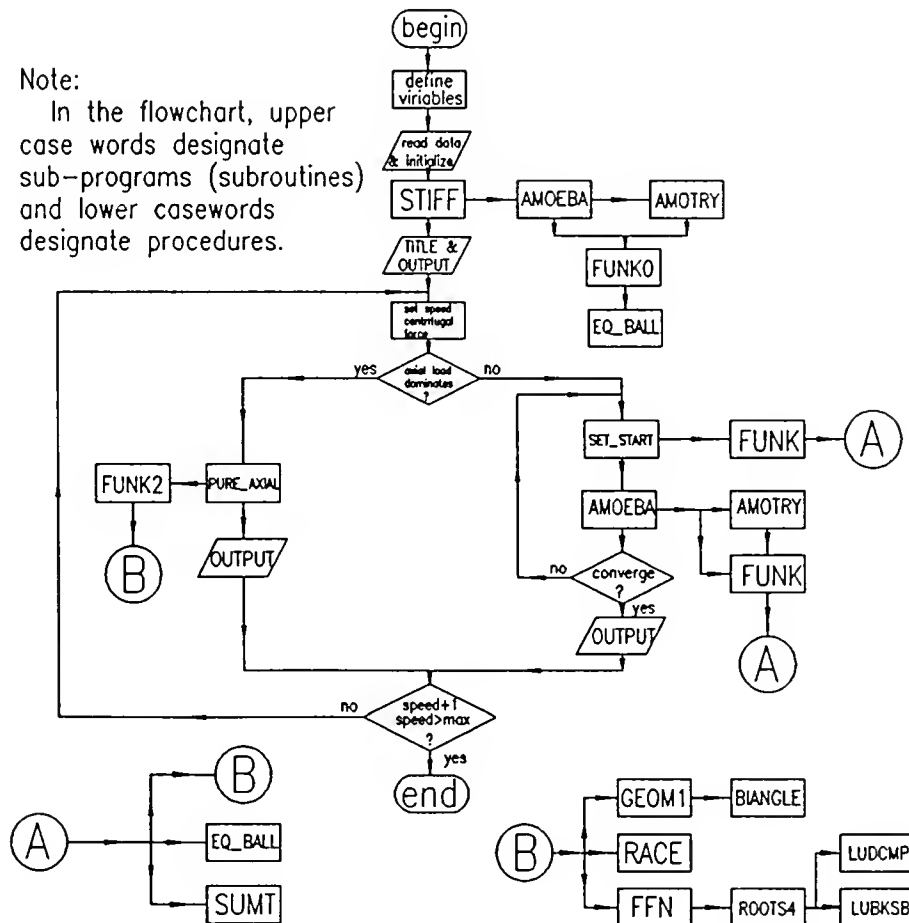


Figure A.1 Program Flowchart

Static Load Calculation (*STIFF*)

The *STIFF* sub-program calculates ball-race contact parameters and load distribution for bearing under stationary conditions through follow equations:

Elliptical-Contact Deformation and Load

$$F = K \delta^{3/2} \quad (1)$$

where F is the normal load at the contact, δ is the deflection at the contact, and K is called the load-deflection constant and can be evaluated by

$$K = \pi k E' \left(\frac{R I_{e2}}{4.5 I_{e1}^3} \right)^{1/2} \quad (2)$$

where E' is equivalent modules of elasticity, R is curvature sum, k is the ellipticity parameter and I_{e1} and I_{e2} are first and second kind elliptical integrals respectively.

Geometry and Load Relations

When a bearing is under external loads, it will have an axial and a radial deflection δ_a and δ_r . If we take balls into account individually, each ball will have the same axial deflection as the bearing axial deflection δ_a , and a radial deflection $\delta_{r,i} = \delta_r \cos \psi$ depending on the location of the ball. The geometrical relation of the deflection of a ball is illustrated in Figure A.2. In

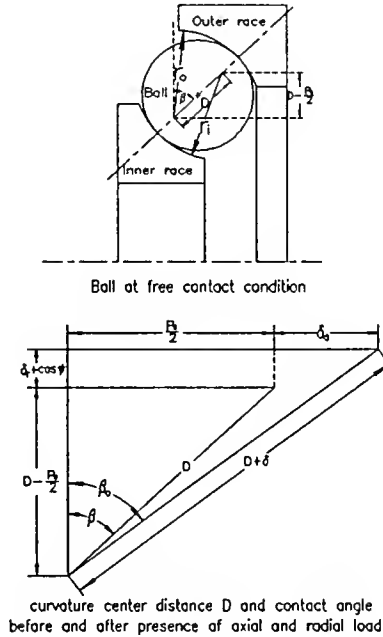


Figure A.2 Ball Contact Geometry and Deflection under Load

this figure, the top part illustrates a ball with no load and its free contact angle is β . The bottom part shows that the ball geometry varies after the axial and radial loads are applied. The normal deflection δ at the ball-race contact is equivalent to an increase in the distance between the two race curvature centers (if the deflection is small, the change of curvature radius is negligible). Then the relation of bearing deflection and ball contact deflection is

$$(D + \delta_i)^2 = (D \cos \beta + \delta_r \cos \psi)^2 + (D \sin \beta + \delta_a)^2 \quad (3)$$

Substituting δ into load-deflection relation gives

$$F_i = KD^{3/2} \left[\left(\cos \beta + \frac{\delta_r}{D} \cos \psi \right)^2 + \left(\sin \beta + \frac{\delta_a}{D} \right)^2 \right]^{1/2} - 1 \quad (4)$$

From Figure A.2 the contact angle β can be obtained in terms of the other parameters, and then the bearing load equilibrium can be expressed as

$$F_a = \sum_1^n F_i \sin \beta \quad (5)$$

$$F_r = \sum_{-\psi_i}^{\psi_i} F_i \cos \beta \cos \psi \quad (6)$$

F_a and F_r are axial and radial components of combined external loads. When F_r is sufficiently large, ψ_1 may not be π :

$$\cos \psi_i = \frac{[1 - (\sin \beta + \frac{\delta_a}{D})^2]^{1/2} - \cos \beta}{\delta_r / D} \quad (7)$$

The unknowns, δ_a , δ_r for the bearing and δ , β for each ball, are obtained by solving the above equations. Since $\sin \beta$ and $\cos \beta$ can be expressed by ball location

angle ψ , deflections δ_a and δ_r and other parameters, the bearing load equilibrium equations include only two unknowns, δ_a and δ_r . The Simplex optimization method was used to solve them. The object function was formed from the equilibrium equations. When true δ_a and δ_r are approached, the function values will approach zero. Other unknowns can be calculated through δ_a and δ_r .

Bearing Load in Rotation

When the bearing rotation speed is considered, the ball's centrifugal force will affect ball-race contact load and contact angle. Thus the geometrical relation will also be different. The displacement relationship is illustrated in Figure A.3. In Figure A.3 L_1 and L_2 can be expressed by D , β , δ_a and δ_r . Ball contact angles β_i , β_o can also be expressed by the ball diameter d , the conformities f_i and f_o , the deflections δ_i and δ_o , and L_1 , L_2 , L_3 and L_4 through the relations in Figure A.3. For each ball

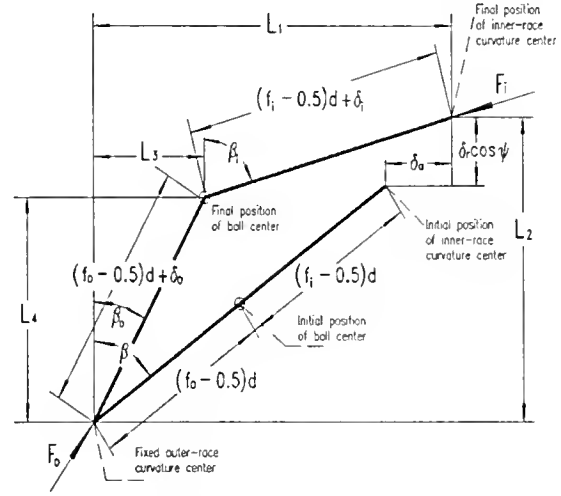


Figure A.3 Deflection of Race-curvature Centers and Ball Center

$$L_1 = D \sin \beta + \delta_a \quad (8)$$

$$L_2 = D \cos \beta + \delta_r \cos \psi \quad (9)$$

$$L_4^2 + L_3^2 - [d(f_o - 0.5) + \delta_o]^2 = 0 \quad (10)$$

$$(D \cos \beta + \delta_r \cos \psi - L_4)^2 + (D \sin \beta + \delta_a - L_3)^2 - [(f_i - 0.5)d + \delta_i]^2 = 0 \quad (11)$$

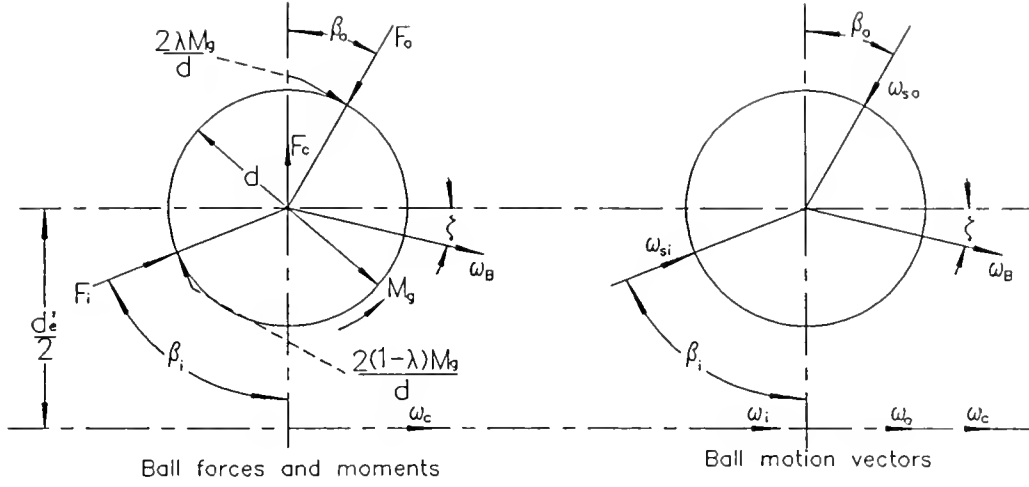


Figure A.4 Ball Forces, Moments and Motion Vectors

The forces and moments acting on a ball as well as ball's motion vectors are shown in Figure A.4. The equilibrium equations of each ball can be written as

$$F_o \sin \beta_o - F_i \sin \beta_i - \frac{2M_g}{d} [\lambda \cos \beta_o - (1 - \lambda) \cos \beta_i] = 0 \quad (12)$$

$$F_o \cos \beta_o - F_i \cos \beta_i + \frac{2M_g}{d} [\lambda \sin \beta_o - (1 - \lambda) \sin \beta_i] - F_c = 0 \quad (13)$$

where F_c is the ball's centrifugal force and M_g is the gyroscopic moment:

$$F_c = \frac{1}{2} m d_e' \omega_c^2 \quad (14)$$

$$d_e' = d_e + 2L_4 - 2d(f_o - 0.5) \cos \beta \quad (15)$$

$$M_g = J_p \omega_B \omega_c \sin \zeta \quad (16)$$

and $\lambda = 1$ for outer-race control, $\lambda = 0$ for inner-race control. If we assume trial values of δ_a and δ_r , we can solve for L_3 , L_4 , δ_i and δ_o simultaneously. The relative

error of the trial values and the true values of δ_a and δ_r can be found through checking the equilibrium of the entire bearing:

$$F_a - \sum_{j=1}^n [F_{ij} \sin \beta_{ij} - \frac{2(1 - \lambda_j) M_{gj}}{d} \cos \beta_{ij}] = 0 \quad (17)$$

$$F_r - \sum_{j=1}^n [F_{ij} \cos \beta_{ij} + \frac{2(1 - \lambda_j) M_{gj}}{d} \sin \beta_{ij}] \cos \psi_j = 0 \quad (18)$$

The speed loop in the program will solve the above equations for the speeds in a speed range of user's interest. Based on the ratio of bearing radial and axial load, two solution strategies are used in the program.

a. Axial Load Dominates (*PURE_AXIAL*)

If the radial load is insignificant, every ball in the bearing will have approximately the same contact angles, loads and speeds, then we can solve the equations for only one ball instead of every ball. So the solution procedure will be simplified. The Golden-section method is used to find δ_a . For each δ_a value, the ball speed, deflection and loads will be calculated by the Newton-Raphson method.

b. Combined Axial and Radial loads (*FUNK*)

The Simplex method is used again and more than half of the bearing balls need to be calculated in every function evaluation. In the computation, many functions used in *PURE-AXIAL* are also used here. Function *SET_START* initializes the bearing and the ball parameters and selects the starting points. Function *AMOEBA* performs the root-searching. The object function is evaluated in function *FUNK*. If the preset accuracy cannot be satisfied after a number (100 to 1000) of Simplex search, the process will be re-started differently.

Input and Output

Input file consists of five lines. The first line is the bearing identification. The second line provides the rotation index (1 for outer ring rotating and 0 for inner ring), the ball and race elasticity modules, tolerance of equilibrium error. The third line: contact angle, inner and outer race contact conformities, bearing pitch diameter. The fourth line: ball diameter, ball material density, ball and race Poisson's ratios. The last line: number of balls, maximum rotation speed, speed step, total external axial and radial loads.

There are six output files to save the calculation results:

- a. Bearing data and deflection (*BRG.OUT*): This file contains the input data, ball mass, bearing axial and radial contact stiffness, the bearing speed, the cage speed, the ball centrifugal force, the number of iterations, the equilibrium error, and the bearing axial and radial deflections.
- b. The angle file (*BALLA.OUT*) contains the ball's location angle and attitude angle, the ball-race contact, the race control, and the inner and outer-race contact angles.
- c. The ball deflection file (*BALLD.OUT*) contains the ball's location angle, the inner and outer-race deflections.
- d. The ball elasticity file (*BALLE.OUT*) contains the inner and outer-race contact constants.
- e. The load file (*BALLF.OUT*) contains the inner and outer-race contact loads.
- f. The ball spin condition file (*BALLS.OUT*) contains the ball's location angle, race-control, spin-to-roll ratio, the ball's spinning speed and the ball's rolling speed.

APPENDIX B

MOTOR LOSS MEASUREMENT

Spindle B has a integrated 2-pole 3-phase, 50 HP AC motor to provide high speed and high power. This motor contributes a significant amount of heat to the spindle. A good estimation of the motor heat generation (motor loss) is important for the spindle thermal modeling.

The motor is powered by a Volkmann inverter drive, Series 8000 variable frequency AC drive. The motor speed is controlled by the drive through the frequency of supplied AC power. The inverter rectifies the commercial 3-phase, 50/60 Hz, 460 V AC power into DC power first, and adjusts this DC voltage to maintain a constant speed/voltage ratio. Then a thyristor switching circuit is used to change the DC power to 3-phase, square-wave AC power. The switching circuit also controls the AC frequency and determines the motor speed. The AC frequency from 0 to 613 Hz corresponds to the motor speed from 0 to 35,000 rpm.

Motor loss is defined as the input power to the motor when the motor output power (shaft power) is zero. The motor loss was measured by two methods: 1) through the inverter DC circuit to get the motor loss, which includes measurement of motor load through DC control circuit and direct measurement of inverter DC power, and 2) through the voltage and current supplied to the motor to calculate motor loss.

The Motor Loss through DC Power Measurement
of the Volkmann Drive @ Idling

The voltage between TB1.30 and TB1.10 is proportional to the motor load and the voltage between TB1.36 and TB1.10 in the inverter indicates DC current (DC Amp. = volt/0.038). The measurement was made by using an oscilloscope to measure the voltage. Since the voltage waveform is not pure DC, the average voltage was measured by using a low pass filter. The DC current can be measured through a shunt resistor and the DC voltage can be measured directly between the DC buses, and the voltage was proportional to speed (600V/35,000rpm) with an error of 5%.

At idle, the DC power minus the loss in the thyristor switching circuit is the motor loss. According to manufacturer, the thyristor circuit loss is about 20% of the DC power. The voltages measured at TB1.30 (V_{30}) were obtained in peak-to-peak values and filtered values respectively. The motor load was calculated based on that $V_{30} = 10 \text{ V}$ indicates a motor torque of 150% of the rated value, which is 7.5 ft-lbs. According to the manufacturer, the motor load estimation through the above methods will has an error of above $\pm 10\%$.

The measurement result is listed in Table B.1, where V_{p-p} is the measured peak-to-peak voltage at TB1.30, V_{filtered} is the measured voltage through a low-pass filter at TB1.30, I_{DC} is the measured DC current, V_{DC} is the measured DC voltage, P_{DC} is the DC power and P_{load} is the motor loss. There are three P_{load} values for each speed, the first one is P_{DC} minus the switching circuit loss, the second is the calculated motor load through V_{p-p} measured at TB1.30, and the third is the motor load through V_{filtered} .

Table B.1 Motor Loss from DC Power Measurement

RPM	V_{Filtered}	I_{DC} (A)	V_{DC} (V)	P_{DC} (W)	P_{load} (W)
2500	0.115	3.0263	42.857	129.7	103.8, 100.0/119.5
5000	0.12	3.1579	85.714	270.7	216.6, 159.4/200.0
7500	0.13	3.4211	128.571	439.9	351.9, 227.7/269.7
10,000	0.14	3.6842	171.429	631.6	505.3, 321.1/359.2
12,500	0.155	4.0789	214.286	874.1	699.3, 438.7/499.0
15,000	0.166	4.3684	257.143	1123.3	898.6, 598.9/778.5
17,500	0.182	4.7895	300.000	1436.9	1149.5, 839.7/1047.4
20,000	0.192	5.0526	342.857	1732.3	1385.8, 1021.4/1276.7
22,500	0.21	5.5263	385.714	2131.6	1705.3, 1294.6/1526.5
25,000	0.222	5.8421	428.571	2503.8	2003.0, 1517.0/1897.3

Motor Loss from the Motor AC Current & Voltage Measurement

The measurement was made in the motor power supply lines. The motor has a Y (star) connection (3-phase, 3-line). The current and voltage signals were measured through resistance dividers and difference amplifiers. The line voltage signals have been decomposed into its component harmonics with different frequency, amplitude and phase angle. Each of the line voltage harmonics was phase shifted 30° and composed to form the phase voltage signal. Then the final power was obtained by integrating the product of the phase current signal and phase voltage signal and dividing the result (work) by the integral time. The result is listed in Table B.2. Since there are many high frequency harmonics not included in the calculation, and since there is discontinuity in the current signal due to the square

wave voltage input, the calculated power is smaller than those obtained through another method.

Table B.2 Motor Loss from
Motor Current & Voltage Measurement

Speed (rpm)	Motor Power (W)
2500	44.45
5000	76.14
7500	139.46
10,000	272.7
12,500	350.5
15,000	811.46
20,000	1011.83
25,000	1281.8

REFERENCES

- [1] Tlusty, J., Zaton, W., and Ismail, F., "Stability Lobes in Milling," *Annals of the CIRP*, Vol. 32, Jan. 1983, pp. 309-313.
- [2] Tlusty, J., "Dynamics of High-Speed Milling," *J. Engr. for Industry*, Vol. 108, May 1986, pp. 59-67.
- [3] *Fafnir High Speed Super Precision Spindle Bearings*, Catalog, Torrington Bearing Company, New Britain, 1987.
- [4] Palmgren, A., *Ball And Roller Bearing Engineering*, 3rd Edition. SKF Industries, Inc., Philadelphia, 1959.
- [5] Harris, T. A., *Rolling Bearing Analysis*, 3rd Edition. John Wiley & Sons, New York, 1991.
- [6] Jones, A. B., *Analysis Of Stress And Deflections*, Vol. 1, New Departure Division of General Motors, Detroit, 1946.
- [7] Jones, A. B., "Ball Motion and Sliding Friction in Ball Bearings," *J. of Basic Engineering, Trans. ASME*, Vol. 81, March 1959, pp. 1-12.
- [8] Lundberg, G., and Palmgren, A., "Dynamic Capacity of Rolling Bearings", *Acta Polytechnica*, Mech. Engr. Series, Vol. 1, No. 3, 1947, pp. 5-50.
- [9] Astridge, D. G., Smith, C. F., "Heat Generation in High-Speed Cylindrical Roller Bearings," *Instn Mech Engrs*, Vol. 186, C14/72, pp. 82-93.
- [10] Ragulskis, K. M., *Vibration of Bearings*, Hemisphere Publishing Corporation, London, 1987.
- [11] Tallian, T. E., "Weibul Distribution of Rolling Contact Fatigue Life and Deviation Therefrom," *ASLE Trans.* Vol. 5, No. 1, April 1962, pp. 183-196.
- [12] Tallian, T. E., "A Unified Model for Rolling Contact Life Prediction," *J. of Lubrication Technology, Trans. ASME*, Vol. 104, July 1982, pp. 336-346.

- [13] Tallian, T. E., "Rolling Bearing Life Prediction. Corrections for Material and Operating Conditions. Part I: General Model and Basic Life," *J. of Tribology, Trans. ASME*, Vol. 110, Jan. 1988, pp. 2-6.
- [14] Tallian, T. E., "Rolling Bearing Life Prediction. Corrections for Material and Operating Conditions. Part II: The Correction Factors," *J. of Tribology, Trans. ASME*, Vol. 110, Jan. 1988, pp. 7-12.
- [15] Harris, T. A., "An Analytical Method to Predict Skidding in Thrust-Loaded, Angular-Contact Ball Bearings," *J. of Lubrication Technology, Trans. ASME*, Vol. 93, Jan. 1971, pp. 17-24.
- [16] Harris, T. A., "Ball Motion in Thrust-Loaded, Angular Contact Bearings With Coulomb Friction," *J. of Lubrication Technology, Trans. ASME*, Vol. 93, Jan. 1971, pp. 32-38.
- [17] Dowson, D., and Higginson, G. R., "Numerical Solution to the Elasto-Hydrodynamic Problem," *J. of Mech. Eng. Science*, Vol. 1, June 1959, pp. 6-15.
- [18] Hamrock, B. J. and Dowson, D., "Isothermal Elastohydrodynamic Lubrication of Point Contacts, Part 1: Theoretical Formulation," *J. of Lubrication Technology, Trans. ASME*, Vol. 98, April 1976, pp. 223-229.
- [19] Gupta, P. K., "Dynamics of Rolling-Element Bearings, Part III: Ball Bearing Analysis," *J. of Lubrication Technology, Trans. ASME*, Vol. 101, July 1979, pp. 312-318.
- [20] Zaretsky, E. V., Signer, H., and Bamberger, E. N., "Operational Limitations of High-Speed Jet-Lubricated Ball Bearings," *J. of Lubrication Technology, Trans. ASME*, Vol. 98, Jan. 1976, pp. 32-39.
- [21] Ioannides, E., and Harris, T. A., "A New Fatigue Life Model for Rolling Bearings," *J. of Tribology, Trans. ASME*, Vol. 107, July 1985, pp. 367-378.
- [22] Ioannides, E., Harris, T. A., and Regen, M., "Endurance of Aircraft Gas Turbine Mainshaft Ball Bearings-- Analysis Using Improved Fatigue Life Theory: Part 1-- Application to a Long-Life Bearing," *J. of Tribology, Trans. ASME*, Vol. 112, April 1990, pp. 304-316.
- [23] Coe, H. H., and Hamrock, B. J., "Performance of 75mm Bore Arched Outer-Race Ball Bearings," *J. of Lubrication Technology, Trans. ASME*, Vol. 99, July 1977, pp. 346-353

- [24] Boness, R. J., "Minimum Load Requirements for the Prevention of Skidding in High Speed Thrust Loaded Ball Bearings," *J. of lubrication Technology, Trans. ASME*, Vol. 103, Jan. 1981, pp. 35-39.
- [25] Kingsbury, E. P., "Slip Measurement in an Angular Contact Ball Bearing," *J. of Lubrication Technology, Trans. ASME*, Vol. 105, April 1983, pp. 162-165.
- [26] Jedrzejewski, J., "Effect of the Thermal Contact Resistance on Thermal Behavior of the Spindle Radial Bearings," *Int. J. Mach. Tools Manufact.*, Vol. 29, No. 2, 1988, pp. 409-416.
- [27] Carmichael, G. D., and Davies, P. B., "Factors Which Affect the Transient Behaviour of Preloaded Ball Bearing Assemblies," *ASLE Trans.*, Vol. 15, Oct. 1971, pp. 1-7.
- [28] Tlusty, J., Hernandez, I., Smith, S., and Zamudio, C., "High Speed High Power Spindles with Roller Bearings," *Annals of the CIRP*, Vol. 36, Jan. 1987, pp. 267-272.
- [29] Shin, Y. C., "Bearing Non-Linearity and Stability Analysis in High Speed Machinery," *Fundamental Issues in Machining*, ASME-PED-Vol. 43, Nov 25-30, 1990, pp. 193-210.
- [30] Stein, J. L., and Tu, J. F., "A State-Space Model for Monitoring Thermal-Induced Preload in Anti-Friction Spindle Bearings of High-Speed Machine Tools," *Proc. of the 1991 ASME WAM Symposium on Control of Manufact. Processes*, Vol. 1, 1992, pp. 1-14.
- [31] Tlusty, J., Smith, S., Smith, D., Bales, C., Zhang, W., and Chau, W., "Machine Tool Research," *National Science Foundation Design and Manufacturing Conference*, University of North Carolina, Charlotte, NC, 1992.
- [32] Eschmann, P., Hasbargen, L., Weigand, K., *Ball and Roller Bearings, Theory, Design and Application*, John Wiley, Chichester, 1985.
- [33] Philips, G. J., "Bearing Performance Investigations through Speed Ratio Measurements," *33rd ASLE Annual Meeting*, Dearborn, Michigan, April 17-20, 1978.
- [34] Sandy, J., "Monitoring and Diagnostics for Rolling Element Bearings," *S&V*, Vol. 22, June 1988, pp. 16-20.

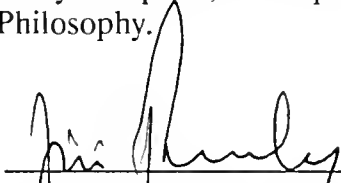
- [35] Berry, James E., "How to Track Rolling Element Bearing Health with Vibration Signature Analysis," *S&V*, Vol. 25, Nov. 1991, pp. 24-35.
- [36] Andreas, J. C., *Energy-Efficient Electric Motors--Selection and Application*, Marcel Dekker, Inc., New York, 1982.
- [37] Holman, J. P., *Heat Transfer*, 6th Edition. McGraw-Hill, New York, 1986.
- [38] Davis, G. de Vahl, Leonardi, E., and Reizes, J. A., "Convection in a Rotating Annular Cavity," *Heat and Mass Transfer in Rotating Machinery*, Edited by Darryl E. Metzger and Naim H. Afgan. Hemisphere Corp., London, 1984, pp. 131-142.
- [39] Bathe, Klaus-Jürgen, *Finite Element Procedures in Engineering Analysis*, Prentice-Hall, Inc., Englewood Cliffs, New Jersey, 1982.
- [40] Quinn, T. J., *Temperature*, Academic Press, Inc., London, 1983.
- [41] Hamrock, B. J., *Ball Bearing Lubrication*, John Wiley & Sons, Inc., New York, 1981.
- [42] Scott, Ian G., *Basic Acoustic Emission*, Gordon and Breach Science Publishers, New York, 1991.
- [43] Berggren, J. C., "Diagnosing Faults in Rolling Element Bearings, Part I. Assessing Bearing Condition," *Vibrations*, Vol. 4, No. 1, March 1988, pp. 5-15.

BIOGRAPHICAL SKETCH

The author was born on September 10, 1959, in Xi'an, Shannxi, China, where he had his early education. He graduated from China Institute of Mining and Technology (currently China University of Mining), Xuzhou, Zhejiang, China, in 1982 with a Bachelor of Science in Mechanical Engineering. The author continued his education in Beijing Graduate School, China University of Mining, Beijing, China, and received a Master of Science in May of 1985. After three years working for China University of Mining, the author enrolled in the University of Florida, to pursue his Doctor of Philosophy in engineering.

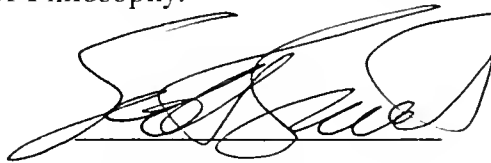
The author is happily married to Aiyu Li.

I certify that I have read this study and that in my opinion it conforms to acceptable standards of scholarly presentation and is fully adequate, in scope and quality, as a dissertation for the degree of Doctor of Philosophy.



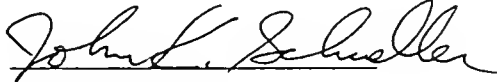
Jiri Tlustý, Chairman
Graduate Research Professor
of Mechanical Engineering

I certify that I have read this study and that in my opinion it conforms to acceptable standards of scholarly presentation and is fully adequate, in scope and quality, as a dissertation for the degree of Doctor of Philosophy.



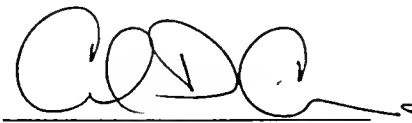
K. Scott Smith
Associate Professor of
Mechanical Engineering

I certify that I have read this study and that in my opinion it conforms to acceptable standards of scholarly presentation and is fully adequate, in scope and quality, as a dissertation for the degree of Doctor of Philosophy.



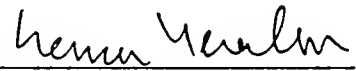
John Schueller
Associate Professor of
Mechanical Engineering

I certify that I have read this study and that in my opinion it conforms to acceptable standards of scholarly presentation and is fully adequate, in scope and quality, as a dissertation for the degree of Doctor of Philosophy.



Carl Crane
Associate Professor of
Mechanical Engineering


I certify that I have read this study and that in my opinion it conforms to acceptable standards of scholarly presentation and is fully adequate, in scope and quality, as a dissertation for the degree of Doctor of Philosophy.



Senser Yeralan
Associate Professor of
Industrial and
Systems Engineering

This dissertation was submitted to the Graduate Faculty of the College of Engineering and to the Graduate School and was accepted as partial fulfillment of the requirements for the degree of Doctor of Philosophy.

May 1993


for Winfred M. Phillips
Dean, College of Engineering

Madelyn M. Lockhart
Dean, Graduate School

UNIVERSITY OF FLORIDA



3 1262 08557 1171